VILNIUS UNIVERSITY

Andrius Melninkaitis

# OPTICAL RESISTANCE OF DIELECTRIC COATINGS TO MULTI-PULSE FEMTOSECOND LASER RADIATION

Doctoral dissertation

Physical sciences, Physics (02 P), Optics (P200)

Vilnius, 2009

The research was performed in 2004-2008 at Vilnius University

**Scientific supervisor:**

*Prof. Habil. Dr.* Valdas Sirutkaitis
(*Vilnius University,* Physical sciences, Physics – 02P, Optics – P200)

**Consultant:**

*Dr.* Marco Jupé
(*Laser Zentrum Hannover e.V.,* Physical sciences, Physics – 02P, Optics – P200)

VILNIAUS UNIVERSITETAS

Andrius Melninkaitis

# DIELEKTRINIŲ DANGŲ OPTINIS ATSPARUMAS PASIKARTOJANTIEMS FEMTOSEKUNDINIAMS LAZERIO IMPULSAMS

Daktaro disertacija

Fiziniai mokslai, fizika (02P), optika (P200)

Vilnius, 2009

Disertacija rengta 2004 – 2008 metais Vilniaus universitete

**Mokslinis vadovas:**

*Prof. habil. dr.* Valdas Sirutkaitis
(*Vilniaus universitetas,* fiziniai mokslai, fizika 02P, optika P200)

**Konsultantas:**

*Dr.* Marco Jupé
(*Hanoverio lazerių centras,* fiziniai mokslai, fizika 02P, optika P200)

# Contents

# Acknowledgements

There is a very long list of good willing people who trusted in me and helped me in many ways when doing this work. There is no space to thank everyone, so if I did not mentioned you, please do not think I forgot you.

However, first of all I need to thank my parents *Danutė* and *Algis* as well as other members of our big family for their support during the period of my long studies.

I am also deeply indebted to my scientific supervisor Professor *Valdas Sirutkaitis* whose trust, stimulating suggestions and endless support helped me all the time.

Special thanks to also the main coauthors of common scientific publications: *Giedrius Abromavičius, Rytis Buzelis, Marco Jupé, Detlev Ristau, Alfridas Skrebutėnas, Remigijus Juškėnas, Algirdas Selskis, Ramutis Drazdys, Rimantas Grigonis, Martynas Barkauskas, Tomas Rakickas, Ona Balachninaitė, Gintaras Tamošauskas, Mindaugas Maciulevičius, Aldona Beganskienė, Aivaras Kareiva* and *Dainius Tumosa.*

Many thanks also to all those altruists for proofreading the manuscript or its separate parts and giving me valuable criticism: to *Julius Janušonis*, *Agnietė Lukoševičiūtė*, *Viačeslav Kudriašov*, *Mikas Vengris*, *Marco Jupé*, *John W. Arenberg, Zita Manstavičienė* and *Vilma Vaskelaitė.*

I also want to thank our dream team which is called *Department of Quantum Electronics of Vilnius University* for a friendly atmosphere conducive to the completion of this thesis. A very big *thank you* goes to the head of the department Professor Algis Petras Piskarskas for his believing in me and giving me possibility to do the necessary research work as well as to use departmental equipment.

Special thanks to my former colleagues from Laser Zentrum Hannover e.V. in Germany, especially *Marco Jupé, Detlev Ristau*, *Kai Starke* and *Holger Blaschke* for

their hospitality, always fruitful discussions, the possibility to join their team during my studies in Hannover according to *Erasmus* program and providing us with experimental IBS coatings.

I also want to thank our optician *Šarūnas Jablonskas*, technician *Juozas Krupauskas* and goddess of cleanness *Rita Gudaitienė*.

I am grateful to all the students who made all the invisible work and some routine measurements when developing separate parts of our equipment, especially: *Darius Mikšys, Tadas Balčiūnas, Julius Mirauskas, Gintarė Batavičiūtė, Andrius Vanagas, Rita Vaižmužytė, Ričardas Buividas, Kęstutis Juškevičius, Alfredas Gradzevičius, Modestas Šinkevičius, Valdemaras Juzumas, Simonas Kičas, Ruslanas Tarchovas, Loreta Meslinaitė* and *Andrius Žukauskas*.

Special thanks to young and dynamic teams of Lithuanian laser companies: *Optida*, *Ekspla* and *Altechna* for the financial support and donation of samples.

Thanks to the Lithuanian Government, Lithuanian study and science foundation, the Faculty of Physics and European structural funds for the financial support of my studies and research.

And last but definitely not least. I thank all my Friends who are not mentioned here for all the sweet little things and being together during either happy or sad moments of my life. Especially I am thankful for all those inspirational everyday questions which sound like this: "*Tai kada ginsies*?" or "*Ar jau parašei*?". From now I promise to be dutiful to remind my younger (or even some older) colleagues of those questions. ;)

*Ačiū Jums Visiems*!

*Andrius Melninkaitis*

*February 2009,Vilnius*

*To my Family*

# List of the Abbreviations

1-*on*-1 – test mode when only one pulse is exposed per single site

AFM – atomic force microscopy

AR – anti-reflection

CCD – charge coupled device

CHDC – characteristic damage curve

DC – direct current

EFI – electric field intensity

e-beam – electron beam evaporation

fs – femtosecond ($10^{-15}$ s)

HR – high reflectivity

IAD – ion assisted deposition

IBS – ion beam sputtering

LIDT – laser-induced damage threshold also used as "damage threshold"

MS – magnetron sputtering

ns – nanosecond ($10^{-9}$ s)

OPA – optical parametric amplifier

PVD – physical vapor deposition

ps – picosecond ($10^{-12}$ s)

*S*-*on*-1 – test mode when S laser pulses are exposed per single site

SHG – second harmonic generation

STE – self trapped exciton

SZM – structure zone model

RMS – root mean square

RF – radio frequency

THG – second harmonic generation

XRD – x-ray diffraction

# Introduction

The history of lasers started on the 16th of May 1960 [1] when Theodore Maiman made the first laser operating by shining a high-power flash lamp on a ruby rod with silver-coated surfaces. A few years later in 1963 Paul D. Maker et al. [2] reported on the first laser induced damage to transparent dielectrics and the production of plasma spark in the air by focusing a pulsed ruby laser beam. These two revolutionary discoveries: *laser* and *laser-induced damage* opened up the vast new fields of science and technology. And up to now the research in all aspects of laser-induced damage is an active and vital area of material science. Especially important subjects of research and debates are the fundamental mechanisms of LIDT.

Interest in laser-matter interaction remains growing due to very broad area of its applications which further stimulate the development of high power lasers. Since the late sixties every ten years the number of scientific publications in the field of *laser damage* almost doubles (Fig. 1). It is obvious that every laser technology is related to the operating laser and the performance of the laser is limited by its parts. The most important part of the laser is an optical system consisting of many coated elements. Some of them are critical with respect to light intensity. Since the system is limited by its weakest component further development of laser technology is closely related to the optical coating technology. It is impossible to increase the power and brightness of laser radiation without improvement of critical components and their optical coatings. Therefore, there is demand for high quality optical coatings with highest available optical resistance. Low absorption and scattering, high

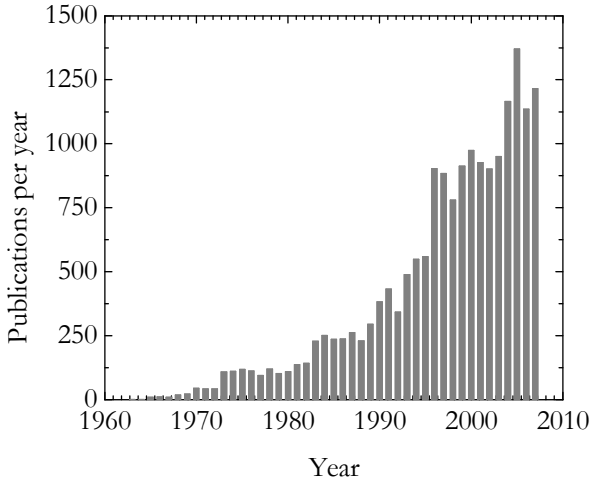


Fig. 1 Number of found scientific publications related to keywords *laser damage* according to SCOPUS database (up to 2008-01-01).

laser-induced damage threshold, good stability and uniformity of the spectral parameters are the requirements for optical components in high power laser applications. In many cases the optical coatings are the most limiting among almost all above mentioned parameters.

Optical coatings are thin-film dielectric layers with thickness comparable to the wavelength of the light. Thin-films can significantly enhance the performance of the optical systems. By controlling the refractive indices, thickness, and order sequence of thin films one can transform substrates such as glass and silicon into optical components such as mirrors, filters, and beam splitters. Nowadays optical coatings are used in nearly every optical device and create a very important part of laser cavities as well as other parts of laser systems.

The fastest development in recent years was observed in the field of femtosecond laser technology. It was shown that mechanisms of optical resistance for ultrashort pulses are different in comparison with nanosecond pulses [3]. However, there are some open questions in understanding of laser damage phenomena. Firstly, the influence of unstable laser radiation on the results of standard damage threshold test procedure is not clear. Secondly, the role of multiphoton ionization in the process of damage initiation is not evident. There is no experimental evidence of multiphoton absorption based damage mechanism in dielectric coatings for femtosecond pulses. Moreover, there are some doubts whether the manipulation of standing wave of electric field intensity being able to increase the optical resistance of thin films is valid for ultrashort pulses. And finally the roles of the specimen surface roughness before deposition and the effect of coating densification are not observed for IR femtosecond pulses. Therefore, all the experimental and theoretical investigations of present study are directed towards deeper understanding of these questions.

**Statements to defend:**

1. The testing of optical resistance in optical surfaces containing absorbing damage precursors by spatially and energetically fluctuating laser radiation leads to the apparently accumulative damage statistics. The *S-on*-1 damage probability increases due to the instabilities and, therefore, the damage threshold will be underestimated.

2. The multiphoton absorption is responsible for stepwise transition in damage threshold of dielectric wide band-gap optical coatings when changing the wavelength of near infrared and visible femtosecond pulses.

3. The roughness of typical substrates before the deposition process does not influence the optical resistance of the deposited $ZrO_2/SiO_2$ HR coatings evaporated by the e-beam and IAD techniques until the characteristic roughness of the coatings exceeds the roughness of substrate.

4. The densification of the growing coating layers by the additional bombardment with accelerated up to ~150 eV Ar+ ions does not influence the optical resistance of HR $ZrO_2/SiO_2$ coatings evaporated by the e-beam technology to femtosecond laser pulses.

5. The suppression of standing wave electric field intensity maxima towards the higher damage threshold layers inside the high reflectivity dielectric mirror layers leads to the increase of optical resistance in the femtosecond range of laser radiation.

**Practical value and novelty**

The impact of spatial and energetic laser fluctuations is related to the *S-on*-1 damage probability. The new concept of statistical accumulation is proposed and explained. This knowledge improves the understanding in the nature of accumulation phenomena and helps to avoid measurement errors. Secondly, the quantized behavior of multiphoton absorption is observed experimentally and theoretically for dielectric optical coatings. This for the first time experimentally confirms previous theoretical assumptions made in a number of studies. This elucidated damage mechanism will also be useful for optical engineers designing high power optical systems operating in a wide range of wavelengths. Furthermore, the results are useful in the selection of the materials for highly resistant optics. The absence of roughness and coating densification influence to the damage threshold in femtosecond domain suggests that even cheaper polishing and evaporation technologies may be selected for manufacturing process. Finally, the interference effects may be used to improve the optical resistance of high reflection coatings in femtosecond range.

**Thesis is structured as follows:**

The chapters that comprise part 1 are a short introduction to the pertinent literature describing coating techniques, materials deposition methods as well as description of the *in house* built LIDT test set-up. A general definition of laser-induced damage threshold (LIDT) and the basic measurement techniques are also described. In part 2 the analysis of currently existing *S-on*-1 LIDT test standard procedure is made by considering unstable multi-pulse laser radiation and its influence to the test results. The approach of investigation is the numerical modeling of the test procedure which leads to *pseudo-accumulation* phenomena in wide ban-gap materials containing absorbing defects. The results of numerical simulations are compared to the experimental data. Part 3 is dedicated to the studies of multiphoton absorption influence to the optical resistance of dielectric

coated optics. The measurements of optical resistance using tunable wavelength source (optical parametric oscillator) were performed. In part 4 the influence of substrate properties and deposition process parameters such as substrate roughness on the laser-induced damage threshold are investigated experimentally. The samples were characterized by atomic force microscopy and X-ray diffraction before and after the coating deposition process. Later the coated samples were LIDT tested by fs pulses and compared. Finally, the effect of standing wave electric field intensity inside the coating layers is investigated in part 5. The design of dielectric coatings was modified in order to shift the peak intensity position of the standing wave towards lower refractive index material having higher damage threshold. The experimental coatings were LIDT tested by fs pulses.

**Contributions**

The author of the thesis designed and conducted the practical part of the study. His contributions and responsibilities consist of:

- preparation of methodology related to performed experiments;
- prediction and numerical modeling of the pseudo-accumulation effect;
- main part of development and automation of LIDT test bench;
- conduction of optical resistance measurements;
- visualization, interpretation, and publication of the experimental results.

Most other ideas and details, and the implementation and the experiments were developed jointly as a team, and it is not possible to give a full account of all of the differences in the contributions of the team members. The main coauthors of the work described in this thesis were Prof. *V. Sirutkaitis*, Dr. *Marco Jupé*, *G. Abromavičius*, Dr. *R. Buzelis*, *D. Mikšys* and *J. Mirauskas*.

Professor *Valdas Sirutkaitis* established the laboratory of optical characterization at *Vilnius University Laser Research Center* (VULRC), thus creating good and friendly conditions for ongoing research. He also participated in formulation of general tasks as well as in interpretation and presentation of obtained results.

Dr. *Marco Jupé* helped in understanding of basic principles of laser induced damage threshold testing. He generated idea about the stepwise transition in multiphoton absorption for single layer dielectric coatings. He also made computer simulations and participated in experiments which are described in chapter 3.

*Giedrius Abromavičius* and Dr. *Rytis Buzelis* were primarily responsible for the evaporation, AFM and spectral characterization and of experimental coatings, which are described in chapters 4 and 5. They also participated in interpretation of those results.

*Darius Mikšys* participated in the initial phase of the experimental set-up development.

*Julius Mirauskas* made contributions in programming of the pseudo-accumulation effect model code.

Professor *Algis Petras Piskarskas* and Doctor *Detlev Ristau* should also be credited for valuable discussions related to concepts of optical resistance testing.

# The List of Author's Publications

*Author has published 28 scientific papers in total. Twenty two of them are closely related to the topic of this thesis* [A1-A22]. *He also made 41 reports* [C1-C41] *at the conferences.*

**Scientific papers related to the topic of this thesis:**


**[A1]** Valdas Sirutkaitis, Robert C. Eckardt, Ona Balachninaite, Rimantas Grigonis, **A. Melninkaitis** and T. Rakickas. *Optical characterization in wide spectral range by a coherent spectrophotometer*, Proc. of SPIE **5188**, p.19 - 34, (2003)

**[A2]** Andrius Zukauskas, **Andrius Melninkaitis**, Valdas Sirutkaitis, Kai Starke and Detlev Ristau. *Nonlinear absorption of ultrashort pulses in HR dielectric mirrors*, Proc. of SPIE **5991**, p.599111 - 10, (2005)

**[A3] Andrius Melninkaitis**, Tomas Rakickas, Darius Miksys, Rimantas Grigonis, Valdas Sirutkaitis, Alfridas Skrebutenas, Rytis Buzelis, Ramutis Drazdys, Giedrius Abromavicius, Remigijus Juskenas and Algirdas Selskis. *Effect of deposition method and substrate surface quality on laser-induced damage threshold for repetitive 13-ns and 130-fs pulses*, Proc. of SPIE **5647**, p.43 - 52, (2005)

**[A4]** Marco Jupé, L. Jensen, Kai Starke, Detlev Ristau, **Andrius Melninkaitis**, Rimantas Grigonis and Valdas Sirutkaitis. *Quantized behavior of fs-LIDT in dielectric layers*, Proc. of SPIE **5647**, p.53 - 60, (2005)

**[A5]** G. Abromavicius, R. Buzelis, R. Drazdys, R. Grigonis, **A. Melninkaitis**, D. Miksys, T. Rakickas, V. Sirutkaitis, A. Skrebutenas, R. Juskenas and A. Selskis. *Influence of ion-assisted deposition on laser-induced damage threshold and microstructure of optical coatings*, Proc. of SPIE **5991**, p.59911F - 7, (2005)

**[A6] A. Melninkaitis**, D. Miksys, R. Grigonis, V. Sirutkaitis, D. Tumosa, G. Skokov and D. Kuzma. *Laser-induced damage thresholds of ion beam sputtered and magnetron sputtered AR-coatings on lithium borate*, Proc. of SPIE **5991**, p.59911C - 11, (2005)

**[A7] A. Melninkaitis**, D. Miksys, T. Balciunas, V. Sirutkaitis, A. Skrebutenas, R. Buzelis, R. Drazdys and G. Abromavicius. *Effect of substrate temperature and ion assistance on nanosecond laser-induced damage threshold in high reflection dielectric coatings*, Proc. of SPIE **5991**, p.59911B - 9, (2005)

**[A8] A. Melninkaitis**, D. Miksys, R. Grigonis, V. Sirutkaitis, D. Tumosa, G. Skokov and D. Kuzma, *Multiple pulse laser-induced damage of antireflection coated lithium triborate*, Proc. of SPIE **5963**, p.59631I - 8, (2005)

**[A9] A. Melninkaitis**, M. Maciulevicius, T. Rakickas, D. Miksys, R. Grigonis, V. Sirutkaitis, A. Skrebutenas, R. Buzelis, R. Drazdys and G. Abromavicius. *Comparison of optical resistance of ion assisted deposition and standard electron beam deposition methods for high reflectance dielectric coatings*, Proc. of SPIE **5963**, p.59631H - 9, (2005)

**[A10] Andrius Melninkaitis**, Darius Miksys, Valdas Sirutkaitis, Giedrius Abromavičius, Rytis Buzelis and Ramutis Drazdys. *Laser-induced damage threshold measurements of high reflecting dielectric layers*, Proc. of SPIE **6596**, p.65961I - 6, (2006)

**[A11]** Giedrius Abromavičius, Rytis Buzelis, Ramutis Drazdys, **Andrius Melninkaitis**, Darius Miksys, Valdas Sirutkaitis and Alfridas Skrebutenas. *Improvement of optical properties and radiation resistance of optical coatings based on Nb[sub 2]O[sub 5] and Ta[sub 2]O[sub 5]*, Proc. of SPIE **6596**, p.65961O - 6, (2006)
**[A12] A. Melninkaitis**, D. Miksys, M. Maciulevičius, V. Sirutkaitis, G. Slekys and A. V. Samoylov. *Laser-induced damage thresholds of starched PMMA waveplates*, Proc. of SPIE **6403**, p.640325 - 640328, (2006)
**[A13] A. Melninkaitis**, K. Juškevičius, M. Maciulevičius, V. Sirutkaitis, A. Beganskienė, I. Kazadojev, A. Kareiva and D. Perednis. *Optical characterization of antireflective sol-gel coatings fabricated using dip coating method*, Proc. of SPIE **6403**, p.64031C - 8, (2006)
**[A14]** A. Beganskiene, S. Sakirzanovas, A. Melninkaitis, V. Sirutkaitis, and A. Kareiva. *Sol-gel derived optical coating with controlled parameters*, Materials Science (Medžiagotyra) **12,** 283-286, (2006)
**[A15]** G. Abromavicius, R. Buzelis, R. Drazdys, **A. Melninkaitis**, D. Miksys, V. Sirutkaitis, A. Skrebutenas, R. Juskenas and A. Selskis, *The microstructure and LIDT of Nb[sub 2]O[sub 5] and Ta[sub 2]O[sub 5] optical coatings*, Proc. of SPIE **6403**, p.640315 - 640317, (2006)
**[A16] A. Melninkaitis**, D. Miksys, T. Balciunas, O. Balachninaite, T. Rakickas, R. Grigonis and V. Sirutkaitis, *Automated test station for laser-induced damage threshold measurements according to ISO 11254-2 standard*, Proc. of SPIE **6101**, p.61011J - 10, (2006)
**[A17]** A. Beganskiene, S. Sakirzanovas, I. Kazadojev, **A. Melninkaitis**, V. Sirutkaitis and A. Kareiva. *Sol-gel derived antireflective coating with controlled thickness and reflective index*, Materials Science *(Poland)* **25**, p.817 - 824, (2007)
**[A18] Andrius Melninkaitis**, Darius Miksys, Rimantas Grigonis, Valdas Sirutkaitis, Marco Jupé and Detlev Ristau. *Comparative studies of laser-induced damage threshold measurements in highly reflecting mirrors*, Proc. of SPIE **6720**, p.672012 - 672018, (2007)
**[A19]** G. Abromavicius, R. Buzelis, R. Drazdys, **A. Melninkaitis** and V. Sirutkaitis. *Influence of electric field distribution on laser induced damage threshold and morphology of high reflectance optical coatings*, Proc. of SPIE **6720**, p.67200Y - 8, (2007)
**[A20]** M. Jupé, M. Lappschies, L. Jensen, K. Starke, D. Ristau, **A. Melninkaitis**, V. Sirutkaitis, I. Cravetchi and W. Rudolph. *Mixed oxide coatings for advanced fs-laser applications*, Proc. of SPIE **6720**, p.67200U - 672013, (2007)
**[A21] A. Melninkaitis**, J. Mirauskas, M. Jupé, D. Ristau, J. W. Arenberg and V. Sirutkaitis. *The effect of pseudo-accumulation in the measurement of fatigue laser-induced damage threshold*, Proc. of SPIE **7132**, p. 713203, (2008)
**[A22]** J.Pilipavičius, I. Kazadojev, A. Beganskienė, A. Melninkaitis, V.Sirutkaitis, A. Kareiva. *Hydrophobic Antireflective Silica Coatings via Sol-gel Process*, Material science (Medžiagotyra), **14** (4), 283-287, (2008)

**Other scientific papers:**

**[A23]** Ona Balachninaite, M. Barkauskas, Robert C. Eckardt, Rimantas Grigonis, M. Maciulevicius, **A. Melninkaitis** and Valdas Sirutkaitis. *Absorptance measurement of nonlinear crystals by calorimetric method at 1064 and 532 nm*, Proc. of SPIE **4751**, p.291 - 296, (2002)
**[A24]** Martynas Barkauskas, **Andrius Melninkaitis**, Modestas Sinkevicius, Arunas Ciburys, Roaldas Gadonas, Valdas Sirutkaitis, Herve Bercegol and Laurent Lamaignere. *Linear and nonlinear absorption and defects formation in KDP crystals used for large aperture doublers and triplers*, Proc. of SPIE **5949**, p.59491T - 9, (2005)
**[A25] Andrius Melninkaitis**, Modestas Sinkevicius, Tadas Lipinskas, Nerijus Slavinskis, Valdas Sirutkaitis, Herve Bercegol and Laurent Lamaignere *Characterization of the KDP crystals used in large-aperture doublers and triplers*, Proc. of SPIE **5647**, p.298 - 305, (2005)
**[A26]** Martynas Barkauskas, **Andrius Melninkaitis**, Darius Miksys, Loreta Meslinaite, Rimantas Grigonis, Valdas Sirutkaitis, Herve Bercegol and Laurent Lamaignere. *Characterization of KDP crystals used in large aperture doublers and triplers*, Proc. of SPIE **6403**, p.64031V - 10, (2006)
**[A27]** T. Balciunas, **A. Melninkaitis**, G. Tamosauskas and V. Sirutkaitis. *Time-resolved off-axis digital holography for characterization of ultrafast phenomena in water*, Optics Letters **33**, p.58 - 60, (2008)
**[A28] Andrius Melninkaitis**, Valdemaras Juzumas, Tadas Balciunas, Valdas Sirutkaitis, Julius Janušonis, Gintas Šlekys. *Formation of grooves in $SiO_2$ coated silicon using femtosecond Ytterbium DPSS laser*, Proc. of SPIE **7005**, p. 70050L, (2008)

**Conference presentations, directly related to the topic of this thesis:**

*The vast majority of presentations listed below were made at: "Boulder damage symposium" (the main international conference of its topic) organizer in Colorado, USA (2003-2008).*

**[C1] A. Melninkaitis,** "Real-Time Detection of Laser-Induced Damage in Dielectric Optics". ICPS 2003, Conference Handbook, – Odense, Denmark. 44 p. 2003
**[C2]** Valdas Sirutkaitis, Robert C. Eckardt, Ona Balachninaite, Rimantas Grigonis, **A. Melninkaitis**, and T. Rakickas, "Optical characterization in wide spectral range by a coherent spectrophotometer", "Advanced characterization techniques for optics, semiconductors and nanotechnologies", 3 – 5 August, San Diego, California USA, 2003
**[C3]** O. Balachninaitė, M. Maciulevičius, **A. Melninkaitis**, R. Grigonis, V. Sirutkaitis, R. Eckardt. "A coherent spectrophotometer based on a periodically poled lithium niobate optical parametric oscillator for optical characterization", "Optical parametric processes and periodical structures: international workshop", p. 71-73., Vilnius, Lithuania, September 26-29, 2004
**[C4] A. Melninkaitis,** D. Mikšys, M. Šinkevičius, M. Maciulevičius, R. Grigonis, V. Sirutkaitis "Optinių lazerinių elementų parametrų standartizuoti matavimai",

Conference "Techninių sistemų diagnozavimas, neardomieji fizikiniai kokybės kontrolės ir skaitiniai metodai - 2004" Vilnius, Lithuania, 2004

**[C5]** Mikšys D., **Melninkaitis A**., Grigonis R., "Lazerio indukuoto pažeidimo slenksčio matavimo sistema", Conference "Techninių sistemų diagnozavimas, neardomieji fizikiniai kokybės kontrolės ir skaitiniai metodai - 2004", Vilnius, Lithuania, 2004

**[C6]** D. Mikšys, **A**. **Melninkaitis**, "Lazeriu indukuotieji pažeidimai optinėse dangose", Konferencijos "Laisvieji skaitymai 2004" pranešimų tezės. 77 p. Vilnius, Lithuania, 2004

**[C7] Andrius Melninkaitis**, Tomas Rakickas, Darius Miksys, Rimantas Grigonis, Valdas Sirutkaitis, Alfridas Skrebutenas, Rytis Buzelis, Ramutis Drazdys, Giedrius Abromavicius, Remigijus Juskenas, Algirdas Selskis, "Effect of deposition method and substrate surface quality on laser-induced damage threshold for repetitive 13-ns and 130-fs pulses", Boulder Damage Symposium XXXVI, National Institute of Standards and Technology, Boulder, Colorado, USA, 20–22 September, 2005

**[C8]** Marco Jupé, L. Jensen, Kai Starke, Detlev Ristau, **Andrius Melninkaitis**, Rimantas Grigonis, Valdas Sirutkaitis, "Quantized behavior of fs-LIDT in dielectric layers", Boulder Damage Symposium XXXVI, National Institute of Standards and Technology, Boulder, Colorado, USA, 20–22 September, 2005

**[C9] A. Melninkaitis**, M. Maciulevicius, T. Rakickas, D. Miksys, R. Grigonis, V. Sirutkaitis, A. Skrebutenas, R. Buzelis, R. Drazdys, G. Abromavicius, R. Juskenas, A. Selskis, "Comparison optical resistance of ion-assisted deposition and standard electron- beam deposition methods for high-reflectance dielectric coatings", "Optical Systems Design 2005", Friedrich-Schiller-Universitaet, Jena, Germany, 12-16 September, 2005

**[C10] A. Melninkaitis**, D. Miksys, R. Grigonis, V. Sirutkaitis, D. Tumosa, G. Skokov, D. Kuzma, "Multiple pulse laser-induced damage of AR-coated lithium borate", "Optical Systems Design 2005", Friedrich-Schiller-Universitaet, Jena, Germany, 12-16 September, 2005

**[C11]** M. Jupé, L. S. Jensen, K. Starke, D. Ristau, **A. Melninkaitis**, V. Sirutkaitis, "High-resolution video-based inspection method for LIDT investigations of thin-disc laser crystals", "Optical Systems Design 2005", Friedrich-Schiller-Universitaet, Jena, Germany, 12-16 September, 2005

**[C12]** A. Zukauskas, **A. Melninkaitis**, V. Sirutkaitis, K. Starke, D. Ristau, "Nonlinear absorption of ultrashort pulses in HR dielectric mirrors", Boulder Damage Symposium XXXVII, National Institute of Standards and Technology, Boulder, Colorado, USA, 19–21 September, 2005

**[C13] A. Melninkaitis**, D. Mikšys, T. Balciunas, V. Sirutkaitis, A. Skrebutenas, R. Buzelis, G. Abromavicius, R. Drazdys, "Effect of substrate temperature and ion assistance on nanosecond laser induced damage threshold in high reflection dielectric coatings", Boulder Damage Symposium XXXVII, National Institute of Standards and Technology, Boulder, Colorado, USA, 19–21 September, 2005

**[C14] A. Melninkaitis**, D. Mikšys, R. Grigonis, V. Sirutkaitis, D. Tumosa, G. Skokov, D. Kuzma, "Laser-induced damage thresholds of ion beam sputtered and magnetron sputtered AR-coatings on lithium borate", Boulder Damage Symposium XXXVII, National Institute of Standards and Technology, Boulder, Colorado, USA, 19–21 September, 2005

**[C15]** R. Buzelis, G. Abromavicius, R. Drazdys, R. Grigonis, **A. Melninkaitis**, D. Mikšys, V. Sirutkaitis, A. Skrebutenas, R. Juskenas, A. Selskis, "Influence of ion-assisted deposition on laser-induced damage threshold and microstructure of optical coatings", Boulder Damage Symposium XXXVII, National Institute of Standards and Technology, Boulder, Colorado, USA, 19–21 September, 2005

**[C16]** D. Mikšys, **A. Melninkaitis**, "Lazeriu indukuotų pažeidimo slenksčių tyrimai termiškai padengtose ir papildomai sutankintose jonų srautu dielektrinėse dangose", "Laisvieji skaitymai 2005", Vilnius, Lithuania, April 22 d., 2005

**[C17]** D. Mikšys, **A. Melninkaitis**, "Effect of deposition method on optical Resistance for Repetitive Laser Pulses", Conference "Advanced materials and technologies", Palanga, Lithuania, 27 – 31 August, 2005

**[C18]** T. Balčiūnas**, A. Melninkaitis**, M. Jupé, "Laser-induced damage detection method of Digital video microscopy", Conference "Advanced materials and technologies", Palanga, Lithuania, 27 – 31 August, 2005

**[C19]** **A. Melninkaitis**, D. Miksys, T. Balciunas, O. Balachninaite, T. Rakickas, R. Grigonis, and V. Sirutkaitis, "Automated test station for laser-induced damage threshold measurements according ISO 11254-2 standard", 8th International Workshop on Laser Beam and Optics Characterization, 6101B-34 at the San Jose Convention Center, in San Jose, California, USA, 21–26 January, 2006

**[C20] Andrius Melninkaitis**, Darius Mikšys, Tadas Balčiūnas, Valdas Sirutkaitis "Automated test station for laser-induced damage threshold measurements of novel laser optics", XII Conference on Laser Optics 2006, III International Conference for Young Scientists on Laser Optics (LOYS), St. Petersburg, Russia, June 26-30, ThS7-04, 2006

**[C21] A. Melninkaitis**, D. Mikšys, V. Sirutkaitis, G. Abromavičius, R. Buzelis, R. Drazdys, "Laser induced damage threshold measurements of high reflecting dielectric layers", P2-10, 5th International Conference "ADVANCED OPTICAL MATERIALS AND DEVICES - AOMD5" Vilnius, Lithuania, 27-30 August, 2006

**[C22]** G. Abromavičius, R. Buzelis, R. Drazdys, D. Perednis, **A. Melninkaitis**, V. Sirutkaitis, A. Skrebutėnas, "Improvement of optical properties and radiation resistance of optical coatings based on $Nb_2O_5$ and $Ta_2O_5$", P2-22, 5th International Conference "ADVANCED OPTICAL MATERIALS AND DEVICES - AOMD5" Vilnius, Lithuania, 27-30 August, 2006

**[C23]** M. Jupé, L. Jensen, K. Starke, D. Ristau, **A. Melninkaitis**, V. Sirutkaitis, "Mixed oxide coatings for advanced fs-laser applications", Boulder Damage Symposium XXXIX, National Institute of Standards and Technology, Boulder, Colorado, USA, 6720-32, 24–27 September, 2007

**[C24]** R. Buzelis, G. Abromavicius, R. Drazdys, **A. Melninkaitis**, V. Sirutkaitis, "Influence of electric-field distribution on laser-induced damage threshold and morphology of high-reflectance optical coatings", 6720-36, Boulder Damage Symposium XXXIX, National Institute of Standards and Technology, Boulder, Colorado, USA, 24–27 September, 2007

**[C25] A. Melninkaitis**, D. Mikšys, R. Grigonis, M. Jupé, D. Ristau, V. Sirutkaitis, "Comparative studies of laser-induced damage threshold measurements in highly reflecting mirrors", 6720-45, Boulder Damage Symposium XXXIX, National

Institute of Standards and Technology, Boulder, Colorado, USA, 24–27 September, 2007

**[C26]** J. Mirauskas, G. Batavičiūtė, **A. Melninkaitis,** "Lazeriu-indukuotojo pažeidimo slenksčio pseudo-akumuliacinis efektas optinėse dangose su nanodefektais", S-24, Laisvieji Skaitymai 2008, Vilnius, Lithuania, 4 April, 2008 (*Best poster presentation*)

**[C27]** **A. Melninkaitis**, J. Mirauskas, M. Jupé, D. Ristau, J. W. Arenberg, V. Sirutkaitis "The effect of pseudo-accumulation in the measurement of fatigue laser-induced damage threshold",7132-2, Boulder Damage Symposium XL, National Institute of Standards and Technology, Boulder, Colorado, USA, 22-24 September, 2008

**Other presentations:**

**[C28]** O. Balachninaitė, M. Barkauskas, M. Maciulevičius, **A. Melninkaitis**, G. Šlekys, R. Grigonis, V. Sirutkaitis, "Didelio tikslumo sugerties matavimai netiesiniuose optiniuose kristaluose", Lietuvos nacionalinė fizikos konferencija 34, Vilnius, Lithuania, 14-16 June, 2001

**[C29]** O. Balachninaitė, M. Barkauskas, R. Grigonis, M. Maciulevičius, **A**. **Melninkaitis**, V. Sirutkaitis, R.C. Eckardt "Calorimetric absorptance measurements of nonlinear crystals" *In* Abstracts 6th International Workshop on Laser Beam and Optics Characterization (WLT/IFSW-Conference "LBOC6", Sub conference of "Lasers in Manufacturing", edited by WLT-German Scientific Laser Society, p. 62-64, Munich, Germany 18-22 June, 2001

**[C30]** O. Balachninaite, M. Barkauskas, R. Grigonis, M. Maciulevičius, **A. Melninkaitis**, V. Sirutkaitis, "Absorptance measurements of nonlinear crystals by calorimetric method" P. 247 (FP13), *In* Technical Digest of XVII International Conference on Coherent and Nonlinear Optics (ICONO 2001, Minsk, Belarus, June 26-July 1, 2001), Published by B.I. Stepanov Institute of Physics, NASB, Minsk, 2001.

**[C31]** M. Barkauskas, **A. Melninkaitis**, M. Maciulevičius "Didelio Tikslumo Sugerties Matavimai Lazeriniuose Optiniuose Elementuose", Conference "Laisvieji skaitymai", Vilnius, Lithuania, 2001

**[C32]** **A**. **Melninkaitis**, M. Barkauskas, V. Sirutkaitis, "Netiesinių kristalų sugerties matavimai 532 nm ir 1064 nm bangos ilgių ruožuose", Conference "Metrologija ir matavimai", Kaunas, 22-23 April, 2002 .

**[C33]** V. Kudriašov, E. Gaižauskas, M. Staponkus, V. Sirutkaitis, **A. Melninkaitis**, "Investigation of self-trapped propagation of femtosecond pulses in fused silica", Solid-state and fiber coherent light sources: EPS-QEOD Europhoton conference, Lausanne, Switzerland, 29 August - 3 September, 2004

**[C34]** M. Jupé, L. Jensen, D. Ristau, **A. Melninkaitis**, M. Šinkevičius, V. Sirutkaitis. "Wavelength dependent high resolution calorimetric measurement - using an OPO system", p. 99-100, Optical parametric processes and periodical structures: international workshop, Vilnius, Lithuania, 26-29 September, 2004

**[C35]** L. Jensen, M. Jupé, D. Ristau, **A. Melninkaitis**, M. Šinkevičius, V. Sirutkaitis, "Wavelength dependent high resolution calorimetric measurement - using an OPO system", XVI Lithuanian – Belarusian seminar "Lasers and optical nonlinearity" 27 – 29 October, Vilnius, 2004

**[C36]** M. Šinkevičius, **A**. **Melninkaitis**, "Optinių komponentų sugerties matavimai", Conference "Laisvieji skaitymai 2004", 80 p. Vilnius, Lithuania, 2004

**[C37] Andrius Melninkaitis**, Modestas Sinkevicius, Tadas Lipinskas, Nerijus Slavinskis, Valdas Sirutkaitis, Herve Bercegol, Laurent Lamaignere, "Characterization of the KDP crystals used in large-aperture doublers and triplers", Boulder Damage Symposium XXXVI, National Institute of Standards and Technology, Boulder, Colorado, USA, 20–22 September, 2005

**[C38]** T. Balčiūnas, **A. Melninkaitis**, "Skaitmeninė video mikroskopija: lazeriu indukuotų pažeidimų detekcija", "Laisvieji skaitymai 2005", Vilnius, Lithuania, 22 April, 2005

**[C39]** M. Šinkevičius, **A. Melninkaitis**, "Greitojo auginimo KDP kristalų sugerties matavimai", "Laisvieji skaitymai 2005", Vilnius, Lithuania, 22 April, 2005

**[C40] Melninkaitis A**., Balčiūnas T., "Digital holographic microscope application for quantitative phase-contrast imaging", WeS7-P03, XII Conference on Laser Optics 2006 and III International Conference for Young Scientists on Laser Optics (LOYS), St. Petersburg, 26-30 June, 2006

**[C41] Andrius Melninkaitis**, Valdemaras Juzumas, Tadas Balciunas, Valdas Sirutkaitis, Julius Janušonis, Gintas Šlekys, "Formation of grooves in $SiO_2$ coated silicon using femtosecond Ytterbium DPSS laser", 7005-21, High-Power Laser Ablation 2008, Taos, New Mexico USA, 20–24 April, 2008

# 1. Literature review and experimental set-up
## 1.1. Dielectric coating technology
### 1.1.1. Electromagnetic waves and Gaussian beams

All electromagnetic phenomena, including the strength of electric field $\boldsymbol{E}$ and magnetic field $\boldsymbol{B}$ and light polarization, can be described in terms of Maxwell's equations [4]:

$$\nabla \boldsymbol{E} = \frac{\rho}{\varepsilon_0}, \tag{1.1.1.1}$$

$$\nabla \boldsymbol{B} = 0, \tag{1.1.1.2}$$

$$\nabla \times \boldsymbol{E} = -\frac{\partial \boldsymbol{B}}{\partial t}, \tag{1.1.1.3}$$

$$\nabla \times \boldsymbol{B} = \mu_0 \left( \boldsymbol{J} - \varepsilon_0 \frac{\partial \boldsymbol{E}}{\partial t} \right). \tag{1.1.1.4}$$

where $\mu_0$ and $^{-}$ $\varepsilon_0$ are the permeability and permittivity of vacuum; $\rho$ and $\boldsymbol{J}$ – the charge and current densities, respectively. The electric and magnetic fields appear coupled in Maxwell's equations. It is possible to de-couple them. The decoupling process brings out some of the most exciting aspects of electromagnetism. For a homogeneous medium, except at its boundaries, (1.1.1.1) reduces to:

$$\nabla \boldsymbol{E} = 0. \tag{1.1.1.5}$$

This result suggests that a linear homogeneous medium, having no free charge inside, cannot sustain any bound charge except (may be) at its boundaries. With (1.1.1.5), the $\nabla \times \nabla \times \boldsymbol{E}$ simplifies to:

$$\nabla \times \nabla \times \boldsymbol{E} = \nabla(\nabla \boldsymbol{E}) - \nabla^2 \boldsymbol{E} = -\nabla^2 \boldsymbol{E}. \tag{1.1.1.6}$$

Taking curl of (1.1.1.3), interchanging $\nabla$ and $\partial / \partial t$ operations on the right-hand side and combining it with (1.1.1.4) leads to the well-known wave equation:

$$\nabla^2 \boldsymbol{E} - \mu\varepsilon \frac{\partial^2 \boldsymbol{E}}{\partial t^2} = 0. \tag{1.1.1.7}$$

In a similar manner, we can obtain:

$$\nabla^2 \boldsymbol{B} - \mu\varepsilon \frac{\partial^2 \boldsymbol{B}}{\partial t^2} = 0 . \qquad (1.1.1.8)$$

Despite of this apparent separation, the electric field $\boldsymbol{E}$ and magnetic field $\boldsymbol{B}$ of an electromagnetic wave remain dependent on each other through Maxwell's equations. Wave equations (1.1.1.7) and (1.1.1.8) describe wave motion in a variety of situations. We can interpret (1.1.1.7) and (1.1.1.8) describe the propagation of the electric and magnetic fields or more appropriately, the propagation of the electromagnetic waves. Electromagnetic waves including the light waves can propagate in absolutely empty space. They do not require matter to facilitate propagation. The periodically varying electric and magnetic fields associated with an electromagnetic wave sustain each other. A comparison of the wave equation with its counterpart for mechanical waves suggests that the product $\varepsilon\mu$ must represent the inverse of the electromagnetic wave propagation speed square. The general plane wave solution of equation (1.1.1.7) is written in the form:

$$\boldsymbol{E}(\boldsymbol{r},t) = E_0(\boldsymbol{r},t)e^{j\phi(\boldsymbol{r},t)} \qquad (1.1.1.9)$$

or in particularly useful form of the harmonic plane wave:

$$\boldsymbol{E}(\boldsymbol{r},t) = E_0(\boldsymbol{r},t)\cos(\boldsymbol{k}\boldsymbol{r} - \omega t + \varphi_0) \qquad (1.1.1.10)$$

where $\boldsymbol{E}_0(\boldsymbol{r}, t)$ and $\varphi(\boldsymbol{r}, t) = \boldsymbol{k}\boldsymbol{r} - \omega t + \varphi_0$ are the amplitude and the phase of the wave, respectively. The plane wave is characterized by the phase $\varphi(\boldsymbol{r}, t)$ which remains constant at any given time in a plane perpendicular to its direction of propagation. The phase $\varphi(\boldsymbol{r}, t) = \boldsymbol{k}\boldsymbol{r} - \omega t + \varphi_0$ satisfies this condition since the dot product $\boldsymbol{k}\cdot\boldsymbol{r}$ remains constant $(=k\cdot r_0)$ as the tip of the position vector $\boldsymbol{r}$ moves over a given plane perpendicular to the direction of propagation $\boldsymbol{k}$; $r_0$ is component of $\boldsymbol{r}$ in the direction of $k$.

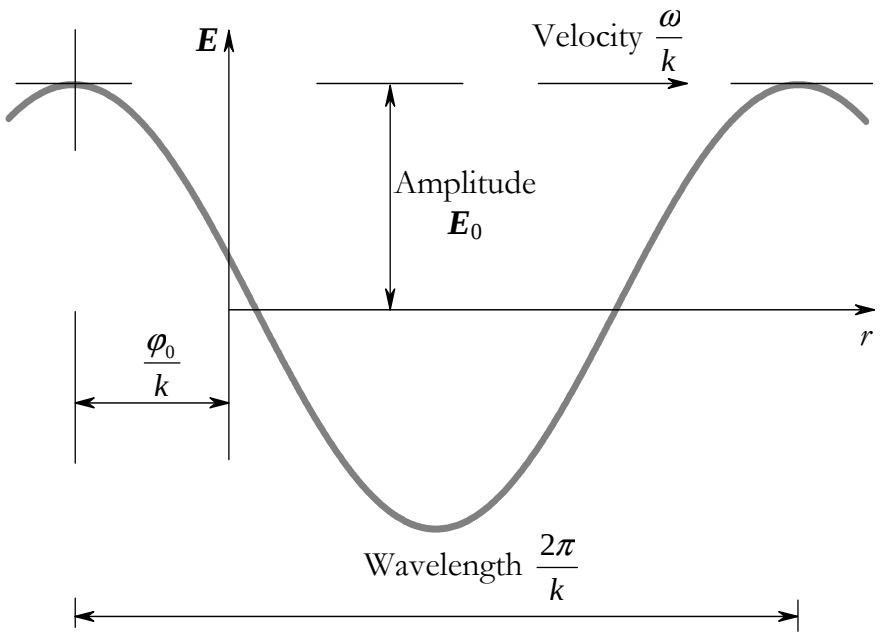


Fig. 1.1.1.1 Progressive cosine wave $\boldsymbol{E}(\boldsymbol{r},t)=E_0(\boldsymbol{r},t)\cos(\boldsymbol{kr}-\omega t+\varphi_0)$ at $t$ = 0.

The amplitude $E_0$ of the plane wave does not depend on the position vector $r$ and time $t$. Intensity of the electromagnetic wave is a time average of the amount of energy that flows per unit time through unit area perpendicular to the energy flow [5]. The intensity is thus related to time average of Pointing vector, $\boldsymbol{S}=(\boldsymbol{E}\times\boldsymbol{B})/\mu$. For the plane wave $\boldsymbol{E}$ and $\boldsymbol{B}$ are perpendicular to each other and $\boldsymbol{B}=\boldsymbol{E}/c_n$, where $c_n=\frac{1}{\sqrt{\varepsilon\mu}}$ is velocity of light in the medium. Thus for the intensity we obtain:

$$I=\langle|\boldsymbol{S}|\rangle=\frac{\langle E^2\rangle}{c_n\mu}=\varepsilon c_n\langle E^2\rangle\approx\frac{1}{2}\varepsilon_0 cnE_0^2 \qquad (1.1.1.11)$$

where c is the velocity of light in vacuum, $n$ is the refractive index of a medium and $\varepsilon_0$ is vacuum permittivity. (1.1.1.11) can be written as follows:

$$I=\frac{E^2}{Z}=\frac{n}{Z_0}\langle E^2\rangle \qquad (1.1.1.12)$$

where $Z$ is medium impedance, and $Z_0$ impedance is the vacuum: $Z = \sqrt{\frac{\mu}{\varepsilon}} = 377\Omega$.

In the case of plane monochromatic electromagnetic wave

$$I = \frac{nE_0^2}{Z} = \frac{n}{Z_0}\left\langle \cos^2(\omega t - \boldsymbol{kr})\right\rangle = \frac{nE_0^2}{2Z_0} \tag{1.1.1.13}$$

If $I$ = 100 W/m², from (1.1.1.13) we obtain ($n$ = 1):

$$E_0 = \sqrt{2Z0I} = 274{,}6 \text{ V/m} \tag{1.1.1.14}$$

Time averaged energy density $\langle\rho\rangle$ of harmonic electromagnetic wave is:

$$\langle\rho\rangle = \frac{1}{2}\varepsilon\left\langle E^2\right\rangle + \frac{1}{2}\mu\left\langle H^2\right\rangle \tag{1.1.1.15}$$

For the plane electromagnetic wave (1.1.1.15) becomes:

$$\langle\rho\rangle = \varepsilon\left\langle E^2\right\rangle \tag{1.1.1.16}$$

For $I$ = 100 W/m² from we obtain:

$$\langle\rho\rangle = \frac{nI}{c} = 3{,}3 \text{ J/m}^3 \tag{1.1.1.17}$$

However, it is very common to refer to the fluency as to the *energy density* (expressed in J/cm²) in the scientific and industrial community dealing with pulsed lasers. The definition of laser fluency in real application will be introduced below. Plane wave approximation is useful for the modeling of many linear reflectance properties. Although plane waves exist only in theory, the beams generated in real lasers have a lot of properties similar to those obtained for plane waves. Beam of light is similar to the plane electromagnetic wave, but its energy is localized in time and space. The most common beams are Gaussian beams. Optical engineers and researchers working on optics deal with laser beams and optical systems as usual tools in their specific areas. In general, propagation of laser beam is a 3D problem (two transversal dimensions $x$, $y$, and one axial dimension $z$), however the Gaussian beam or $TEM_{00}$ mode has axial symmetry and 2D analysis is sufficient. The amplitude distribution of a Gaussian laser beam can be written as [6]:

$$E(x,z) = E_0 \cdot \sqrt{\frac{2}{\pi}} \cdot \frac{\omega_0 \exp(-i[\varphi_0 - \varphi(z)])}{\omega(z)} \cdot \exp\left(-i\frac{kx^2}{2R(z)} - \frac{x^2}{\omega^2(z)}\right) \tag{1.1.1.18}$$

This expression describes the behavior of the laser beam amplitude as a function of the transversal coordinate $x$ and the axial coordinate $z$. $k = 2\pi/\lambda$ is the wave number, where $\lambda$ is the wavelength of the propagating beam in a material. Function $\omega(z)$ describes beam radius evolution along the propagation direction which is defined at the $1/e$ in electric field amplitude, or $1/e^2$ in irradiance level with respect to the amplitude on the propagation axis [7-10]:

$$\omega(z) = \omega_0 \sqrt{1 + \left( \frac{z\lambda}{\pi\omega_0^2} \right)^2} . \tag{1.1.1.19}$$

Function

$$R(z) = z\left[ 1 + \left( \frac{\pi\omega_0^2}{z\lambda} \right)^2 \right] \tag{1.1.1.20}$$

is known as the radius of curvature of a wave-front of the Gaussian beam, and

$$\varphi(z) = \tan^{-1}\left( \frac{z\lambda}{\pi\omega_0^2} \right) \tag{1.1.1.21}$$

is known as the Guoy phase shift. In the case of pulsed Gaussian beams the electric field intensity (1.1.1.18) is multiplied by term $\exp\left( -4\ln 2 \frac{t^2}{\tau^2} \right)$ [11], where $\tau$ is pulse duration (FWHM). As defined in [12, 13] the maximum energy density $H_{\max}$ of the pulsed Gaussian beam is given:

$$H_{\max} = \frac{Q}{A_{eff}} \tag{1.1.1.22}$$

The maximum power density $P_{\max}$ is defined as:

$$P_{\max} = \frac{H_{\max}}{\tau} \tag{1.1.1.23}$$

where $Q$ is the total energy of the Gaussian pulse, and $A_{eff}$ is:

$$A_{eff} = \frac{\pi\omega^2(z)}{2} \tag{1.1.1.24}$$

## 1.1.2. Reflection at boundary of dielectrics and Fresnel formulas

In order to understand the reflection and transmission properties of multilayer coatings, single optical interface properties should be discussed. It is well known that the reflection angle $\beta$ is equal to the angle of incidence $\alpha$ (Fig. 1.1.2.1) and the relationship between the angles of incidence $\alpha$ and refraction $\gamma$ is described by Snell's law:

$$n_1 \sin(\alpha) = n_2 \sin(\gamma) \qquad (1.1.2.1)$$

However, this relation does not speak about amplitudes of the reflected and transmitted waves. Consider two homogenous and isotropic media which both are of zero conductivity and consequently perfectly transparent; their magnetic permeabilities in fact will not differ from unity $\mu_1 = \mu_2 = 1$ [14]. Let us consider complex electric vector with amplitude $\boldsymbol{E} = \boldsymbol{a}_\perp + \boldsymbol{a}_\parallel$ that can be resolved into components parallel $a_\parallel$ (denoted by subscript $\parallel$) and perpendicular $a_\perp$ (denoted by subscript $\perp$) to the plane of incidence (Fig. 1.1.2.1 A and B).

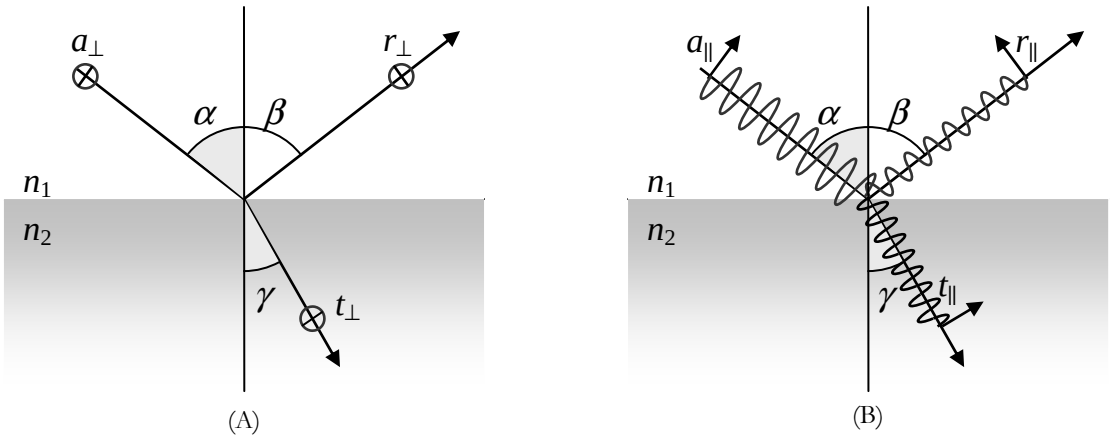


Fig. 1.1.2.1. Reflected and transmitted of electromagnetic waves at a boundary of different refractive indices. A – electric field vector is perpendicular to the plane of incidence and reflection (*S*-polarization); B – electric field vector is parallel to the same plane (*P*-polarization).

Boundary conditions [14, 15] require the tangential component of $\boldsymbol{E}$ and $\boldsymbol{H}$ vectors to be continuous across the boundary. Similar conditions are

automatically fulfilled for normal components. Using boundary conditions and Maxwell's relation $n=\sqrt{\varepsilon\mu}$ we can obtain the components ⊥ and ∥ of the reflected $r$ and transmitted $t$ waves in terms of those of the incident wave $a$:

$$t_{\parallel}=\frac{2n_1\cos(\alpha)}{n_2\cos(\alpha)+n_1\cos(\gamma)}a_{\parallel} \quad (1.1.2.2) \qquad t_{\perp}=\frac{2n_1\cos(\alpha)}{n_1\cos(\alpha)+n_2\cos(\gamma)}a_{\perp} \quad (1.1.2.3)$$

$$r_{\parallel}=\frac{n_1\cos(\alpha)-n_2\cos(\gamma)}{n_1\cos(\alpha)+n_2\cos(\gamma)}a_{\parallel} \quad (1.1.2.4) \qquad r_{\perp}=\frac{n_1\cos(\gamma)-n_2\cos(\alpha)}{n_1\cos(\gamma)+n_2\cos(\alpha)}a_{\perp} \quad (1.1.2.5)$$

Equations (1.1.2.2 – 1.1.2.5) constitute the Fresnel relations. An important fact is that whenever light reflects of a surface of higher index of refraction $n_1<n_2$, a 180° phase shift in the wave is introduced. For example, light in air reflecting of just about anything (glass, water, oil, etc.) will undergo a 180° phase shift. On the other hand, when the first medium $n_1$ is oil, which has a higher $n$ than the second medium (i.e. water) $n_1>n_2$, the reflected wave will have no phase shift. Note that a shift by 180° is equivalent to the wave traveling a distance of half a wavelength.

The formulas (1.1.2.2 – 1.1.2.5) are derived for components of the reflected and transmitted waves in terms of electric field. In practice, the reflectance $R$ and transmittance $T$, which refer to the division of the incident irradiance into the reflected and transmitted irradiances [4], are of fundamental significance. In the absence of absorption and scattering losses at the interface between two media, the relation

$$R + T = 1 \quad (1.1.2.6)$$

must be held for reasons of energy conservation. Transmitted and reflected part of the incident energy which crosses the unit interface area per unit time is proportional to the square of electric field:

$$T_{\parallel}=\left[\frac{t_{\parallel}}{a_{\parallel}}\right]^2=\left[\frac{2n_1\cos(\alpha)}{n_2\cos(\alpha)+n_1\cos(\gamma)}\right]^2, \quad (1.1.2.7)$$

$$T_{\perp}=\left[\frac{t_{\perp}}{a_{\perp}}\right]^2=\left[\frac{2n_1\cos(\alpha)}{n_1\cos(\alpha)+n_2\cos(\gamma)}\right]^2, \quad (1.1.2.8)$$

$$R_{\parallel} = \left[\frac{r_{\parallel}}{a_{\parallel}}\right]^2 = \left[\frac{n_1\cos(\alpha) - n_2\cos(\gamma)}{n_1\cos(\alpha) + n_2\cos(\gamma)}\right]^2, \quad (1.1.2.9)$$

$$R_{\perp} = \left[\frac{r_{\perp}}{a_{\perp}}\right]^2 = \left[\frac{n_1\cos(\gamma) - n_2\cos(\alpha)}{n_1\cos(\gamma) + n_2\cos(\alpha)}\right]^2. \quad (1.1.2.10)$$

## 1.1.3. Interference in thin-film coatings

The optical properties of thin dielectric films arise from interference and reflection. There are many examples in nature of the surfaces which reflect due to step-like modulation of their refractive index. Probably the simplest one is thin oil layer floating on the water. Because of superposition and interference of reflected waves thin film coated surfaces appear to have various colors when illuminated by white light. Consider two reflected parallel traveling plane electromagnetic waves in (Fig. 1.1.3.1): light from the air reflecting of the top surface $r_1$ and light traveling from the air, through oil, reflecting off the bottom surface, traveling back through oil and out into the air again $t_1 t_1' r_2$.

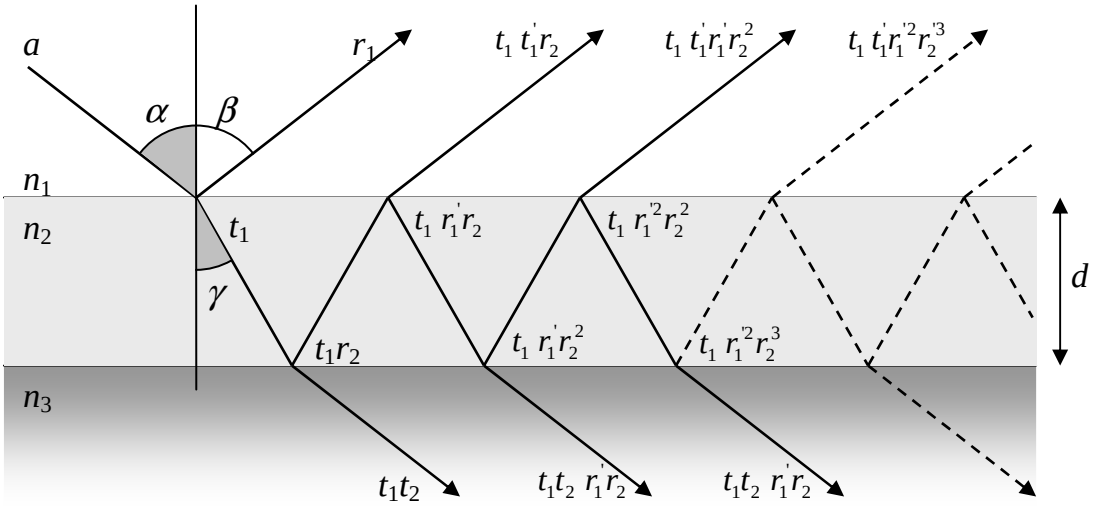


Fig. 1.1.3.1. Multiple reflections in thin oil layer on the water [16].

The resultant reflected wave $r$ is a superposition of two interfering light waves $r_1$ and $t_1 t_1' r_2$ reflected from the top surface (oil/air) and from the bottom surface (water/oil) respectively:

$$r = r_0\cos(\omega t + \delta_3) = r_{10}\cos(\omega t + \delta_1) + t_{10}t_{10}' r_{10}\cos(\omega t + \delta_2), \quad (1.1.3.1)$$

where

$$r_0 = \sqrt{(r_{10})^2 + 2 \cdot r_{10} \cdot t_{10} t_{10}^{'} r_{10} \cos(\delta_1 - \delta_2) + (t_{10} t_{10}^{'} r_{10})^2}\,, \qquad (1.1.3.2)$$

and

$$\delta_3 = \arctan\left( \frac{r_{10} \sin(\delta_1) + t_{10} t_{10}^{'} r_{10} \sin(\delta_2)}{r_{10} \cos(\delta_1) + t_{10} t_{10}^{'} r_{10} \cos(\delta_2)} \right). \qquad (1.1.3.3)$$

are the amplitude and phase of the resulting wave $r$ respectively. Note that the frequency in the reflected wave is the same as in the incident wave but the wavelength in a medium depends on the index of refraction. Wavelength in a medium with refractive index $n$ is related to the wavelength in vacuum (which differs negligibly from the wavelength in air) by:

$$\lambda_{medium} = \frac{\lambda_{vacuum}}{n} \qquad (1.1.3.4)$$

These are the main reasons why thin films, such as thin oil layer, can change the reflection properties of the surface, i.e., water surface. The same principle can be applied in order to manufacture optics well suited for laser applications, artificially reproducing nature's discovery. As described below various physical vapor deposition (PVD) processes can be applied to release a material from a source and transfer to substrate, forming a thin film or coating. Evaporated dielectric films are an essential part of the resonator optics. Typical lasers require highly reflective and partially reflective mirrors as well as many antireflection coatings on the gain media, Q-switch crystals, windows, lenses and etc. [17].

### 1.1.3.1. Single layer AR coating

High or low reflection coefficient can be obtained from a stack of quarter-wave dielectric layers of alternate high (H) and low (L) refractive index. The simplest dielectric coating is single layer antireflection (AR) coating [15, 17] which consist of a single quarter-wave optical thickness (QWOT) film. The reflectivity of a

single dielectric layer of index $n_1$, which has an optical thickness of $\lambda/4$, is, at normal incidence,

$$R = \left( \frac{n_2 - n_1^2}{n_2 + n_1^2} \right)^2 \qquad (1.1.3.1.1)$$

where $n_2$ is the refractive index of the substrate. Zero reflection is achieved when

$$n_1 = \sqrt{n_2} \qquad (1.1.3.1.2)$$

Table 1.1.3.1.1. Some of the dielectric compounds used for evaporation of dielectric layers [18]

| Chemical formula | Material | Melting point, °C | Approximate refractive index |
|---|---|---|---|
| $TiO_2$ | Titanium dioxide (titania) | 1640 - 1850 | 2.45 |
| $Ta_2O_5$ | Tantalum pentoxide (tantala) | 1870 | 2.10 |
| $Nb_2O_5$ | Niobium pentoxide | 1520 | 2.20 |
| $ZrO_2$ | Zirconium dioxide (zirconia) | 2677 | 2.10 |
| $HfO_2$ | Hafnium dioxide (hafnia) | 2812 | 1.98 |
| $Al_2O_3$ | Sapphire | 2030 | 1.60 |
| $SiO_2$ | Quartz (silica) | 1830 | 1.48 |
| MgO | Magnesium oxide | 2800 | 1.72 |
| $MgF_2$ | Magnesium fluoride | 1261 | 1.38 |

Many different materials are used for the construction of optical multilayer coatings. However, when using conventional deposition techniques there are not too many possibilities to tune the refractive index of the material except the case when evaporating materials are mixed during the process. The choice of refractive indices was limited by the set of existing dielectric materials [19]. The list of mostly used dielectric coating materials used for the deposition of non-absorbing layers in ultraviolet, visible, and infrared spectral range is given [18] in Table 1.1.3.1.1. Given approximate refractive indices are estimated at the

midpoints of the material transparency range. The lowest refractive index available as stable film is $MgF_2$ with $n_1 = 1.38$, a value which results in a perfect antireflection coating for a substrate with $n_2 = 1.90$. For $n_2 = 1.80$, 1.70, and 1.5 the residual reflectance from a $\lambda/4$ $MgF_2$ coating is ≈ 0.1, 0.3, and 1.4%, respectively. $MgF_2$ is an excellent match for very popular Nd:YAG crystals. In cases of reflection from a single-layer antireflection coating being too high, two or more dielectric layers must be applied.

### 1.1.3.2. Two layer AR coating

A substrate of two layers [17] with index values of $n_1$ and $n_2$ having optical thickness of $\lambda/4$ will have a total reflectance of

$$R = \left( \frac{n_2^2 - n_1^2 n_3}{n_2^2 + n_1^2 n_3} \right)^2 \qquad (1.1.3.2.1)$$

where $n_3$ is the refractive index of the substrate. Zero reflection can be obtained if $(n_2/n_1)^2 = n_3$. If coating materials with the proper ratio $n_2/n_1$ are not available for a particular substrate, thicknesses which deviate from $\lambda/4$ must be used to achieve zero reflection from glass. Region of low reflectance for this type of coating is rather small, so this kind coating is sometimes also called *V*-coating. A very hard and durable two-layer coating frequently employed on glass substrates is the system $ZrO_2$ and $MgF_2$.

### 1.1.3.3. HR coating

High reflectivity, multilayer dielectric films (Fig. 1.1.3.3.1) can be tailored for specific reflectance versus wavelength characteristics by the appropriate choice of the number of layers, layer thickness, and the index of refraction of materials. The simplest design of a multilayer coating is a stack of alternating films of equal optical thickness, corresponding to $\lambda/4$, but of two different refractive indices. It

is the most efficient way to start and end with a high-index layer so that the structure will have an odd number of layers. We obtain

$$R_{\max} = \left( \frac{n_H^{l+1} - n_L^{l-1} n_3}{n_H^{l+1} - n_L^{l-1} n_3} \right)^2 \qquad (1.1.3.3.1)$$

where $n_1$ is for the high-index material, $n_2$ is for the low-index material, and $l$ is the odd number of $\lambda/4$ films.

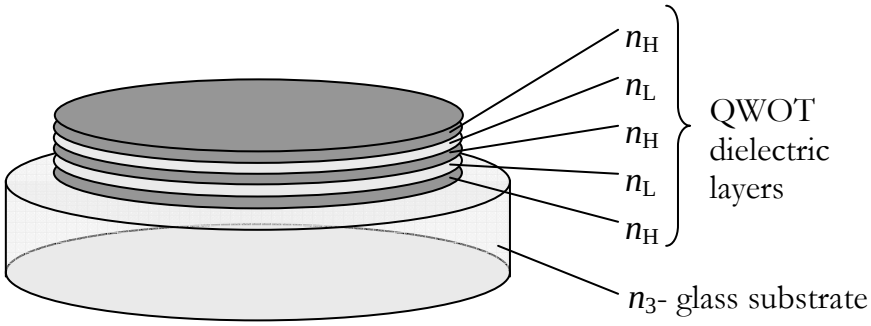


Fig. 1.1.3.3.1. High reflectivity, multilayer dielectric mirror - a stack of alternating low ($n_L$) and high ($n_H$) refractive index films of equal optical thickness, corresponding to $\lambda/4$ [16].

## 1.1.4. Matrix formalism and standing wave inside the layer

The analytical modeling of HR, AR and more advanced coatings for laser applications is based on the matrix formalism which is derived from classical Fresnel reflection and transmission (1.1.2.2 – 1.1.2.5) formulas at the boundary. Electromagnetic field is described in terms of transfer function. In the case of single layer the matrix can be constructed [16, 20] which transfers field components at the entrance of coating to distance $d_i$ just before the second boundary of thin layer. Consider the plane wave described in equation (1.1.1.9) incident upon the thin film of physical thickness $d_i$. At the first interface (Fig. 1.1.3.1.), a part of this plane wave is directly reflected with an amplitude of $A_0=E_0r_1$, which can be calculated using the reflection coefficient $r_1$ given by the Fresnel formulas depending on polarization in equation (1.1.2.4) or (1.1.2.5).

Then the additional phase shift produced by optical path of the traveling wave (from the front to rear interface and back) must be taken into account:

$$\delta_i = \frac{2\pi n_i d_i \cos(\gamma_i)}{\lambda}; \tag{1.1.4.1}$$

which is dependant on the thickness $d_i$ of the layer, the refractive index $n_i$ and angle of incidence $\alpha_i$ which is related to $\gamma_i$ by Snellius law in equation (1.1.2.1). Following the wave reflected the first time inside the layer, a further phase shift for the path from the rear side to the front side has to be taken into account. This partial wave is then transmitted by the front surface resulting in amplitude $A_1$ of the first order wave ($k = 1$) leaving the layer:

$$A_1 = t_1 t_1' r_2 E_0 \exp(-j2\delta); \tag{1.1.4.2}$$

where $t_1'$ is the Fresnel transmission coefficient defined by equations (1.1.2.2) or (1.1.1.3) for the amplitude of the wave passing the first boundary of the layer. By following the wave further through the layer, amplitudes of each partial wave of the order $k$ can be determined as:

$$A_1 = t_1 t_1' r_2 E_0 \exp(-j2\delta) \cdot \left(r_1' r_2 \exp(-j2\delta)\right)^{k-1}. \tag{1.1.4.3}$$

It is obvious that the contributions of the partial waves follow the rule of the geometric expansion, and therefore, the total amplitude of the wave reflected by the layer, which is the sum of the amplitudes of partial waves, can be expressed in closed form:

$$A_\infty = \left[ r_1 + \frac{t_1 t_1' r_2 E_0 \exp(-j2\delta)}{1 - r_1' r_2 \exp(-j2\delta)} \right] \cdot E_0. \tag{1.1.4.4}$$

The reflection coefficient $r_s$ of a single layer is given by the ratio between the total amplitude of the reflected wave and the amplitude of the incoming wave:

$$r_s = \frac{r_1 + r_2 \exp(-j2\delta)}{1 + r_1 r_2 \exp(-j2\delta)}. \qquad (1.1.4.5)$$

In this equation, the coefficients $r_1'$ and $t_1'$ have been replaced by using the relations:

$$t_1 t_1' = (1 - r_1')(1 - r_1) = (1 - r_1)(1 + r_1) = 1 - r_1^2. \qquad (1.1.4.6)$$

However, considering an enormously increasing number of partial beams, the resulting equations become extremely complicated for multilayer structures. Therefore, a matrix formalism, which can be deduced from the boundary conditions of the electric and magnetic field at the interfaces, is usually employed for calculation of thin film systems. The major advantage of this approach is the representation of each layer by a single matrix $M_i$ containing all specific parameters of the film. The matrix $M_i$ of a thin film at the position $i$ within layer system relates the electric ($E_{i-1}$) and magnetic ($H_{i-1}$) field strength at the front face to the field strength values ($E_i$ and $H_i$) at the rear face of the layer:

$$\begin{pmatrix} E_{i-1} \\ H_{i-1} \end{pmatrix} = M_i \begin{pmatrix} E_i \\ H_i \end{pmatrix} = \begin{pmatrix} \cos(\delta_i) & \frac{j}{n_i}\sin(\delta_i) \\ j n_i \sin(\delta_i) & \cos(\delta_i) \end{pmatrix} \begin{pmatrix} E_i \\ H_i \end{pmatrix}. \qquad (1.1.4.7)$$

By considering boundary conditions for the field strengths at the interfaces the matrix components of (1.1.4.7) can be determined. On the basis of the matrix formalism, the transfer function of a layer system can be simply calculated by a multiplication of matrices $M_i$ representing the constituent single layers. Thus the transfer matrix $M_{stack}$ of a stack, which is formed by a number of $K$ single layers with layer 1 located at the first interface in respect to the incoming wave, is given by:

$$M_i = M_1 \cdot M_2 \cdot M_3 \cdot \ldots \cdot M_i \cdot M_{i+1} \cdot \ldots \cdot M_K. \qquad (1.1.4.8)$$

For calculations of reflection coefficient $r_{SK}$ of entire arrangement including the substrate (index of refraction $n_T$) and the ambient medium (index of refraction $n_0$), again the ratios of the amplitudes have to be considered:

$$r_{SK} = \frac{n_0 M_{11} + j n_0 n_T M_{12} - j M_{21} - n_T M_{22}}{n_0 M_{11} + j n_0 n_T M_{12} + j M_{21} + n_T M_{22}} \tag{1.1.4.9}$$

By artificially introducing negligibly thin layer of the same refractive index into the selected depth of the interest it is possible to obtain electric fields at any arbitrary depth $z$ from the surface of stratified films. The electric field distributions of standing waves [21] in a single layer AR and standard HR stack coatings are shown in (Fig. 1.1.4.1). The intensity inside the multilayer coating can reach up to four times higher values than that of incident traveling wave because of the standing waves. This effect can drastically decrease the LIDT of the coating compared with bare substrate and is known as the standing wave effect. Computation of the electric field intensity (EFI) can yield valuable information about the performance of thin film coatings. In general, coating designers want to minimize laser damage by reducing EFI inside the more absorbing or less optically resistant layers.

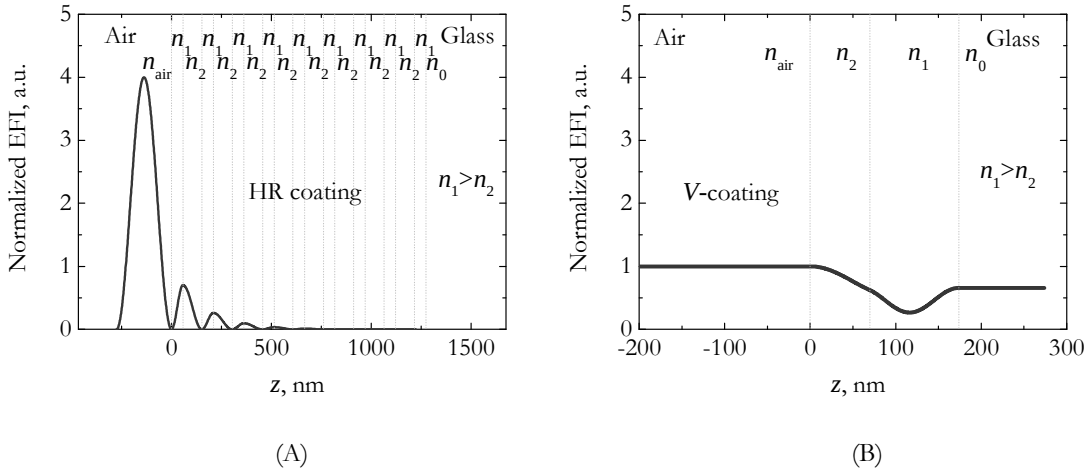


Fig. 1.1.4.1 The computation of the electric field intensity (EFI): A – QWOT stack HR coating and B – two layer AR coating.

### 1.1.5. Coating deposition techniques

Thin-film technologies are essential for laser manufacturers because of the fact that optical coatings may significantly enhance the performance of optical systems. Production of optical coatings started in the 1940s by using boat evaporation [20, 22]. By controlling the type, number, thickness, and sequence of thin films, one can transform substrates such as glass or silicon into optical components such as mirrors, filters, and beam splitters. However, the optical resistance and other properties of multilayer coatings strongly depend on the materials used in the deposition process as well as on the surface quality of the substrate. Many deposition processes known as Physical Vapor Deposition (PVD) releasing a material from a source and transferring it to a substrate are used. The following chapters shortly introduce five commonly used optical interference dielectric coating production techniques which are of the major importance for laser technology: electron-beam deposition (e-beam), ion-assisted deposition (IAD), ion-beam sputtering (IBS) and magnetron sputtering (MS), sol-gel method (Sol-gel). However, all these sections are, of necessity, just summaries of the subject.

#### 1.1.5.1. E-beam coating process

In conventional electron beam evaporation method also know as the e-beam evaporation, a block of the material (source) to be deposited is heated by the electron beam to the point where it starts boiling and evaporating. Then it is possible to condense it on the substrate. This process takes place inside a vacuum chamber, enabling the molecules to evaporate freely and condense on all surfaces. e-beam method is typically [18] a

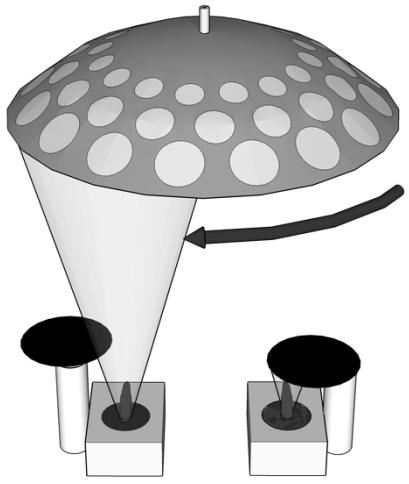

Fig. 1.1.5.1.1. E-beam coating plant.

low-energy process (particle energy is ~0.1 eV) and the resulting films frequently have a porous structure. The porosity may vary with the material, substrate temperature, residual pressure in the deposition chamber, deposition rate, and angle of incidence of vapor on the substrate. Typically the porosity values are in range from 0 to 40 percent. On exposure to the atmosphere, some of the voids in the film may absorb water vapor. This increases the effective refractive index of the films and results in shift of spectral features of the multilayer towards longer wavelengths. Multi-layer coatings can be deposited in one duty cycle.

### 1.1.5.2. IAD coating process

The microstructure of films can be significantly affected by bombarding the substrate during deposition with energetic ions from an auxiliary ion beam source [23-32]. The additional energy (from 50 to 300 eV) results in denser films. Hence, the coatings produced by ion - assisted deposition have higher refractive indices and exhibit less ageing on exposure to the atmosphere. The ion plating process can result in even denser coatings. In this high deposition rate process the starting material must be a good conductor and is usually a metal. Argon and a reactive gas species are introduced into the chamber and are ionized together with the evaporant. Ions are then accelerated to the substrate with energies of order 10 to 300 eV. Transparent films with near bulk-like densities and low temperature variation of refractive index can be obtained by this process. For most materials, layers are glasslike and interfaces remain smooth. This results in lower scattering values of growing films. Conventionally evaporated thin films can be under compressive or tensile stresses. Without being controlled, these stresses can distort the substrate or cause the multilayer to break up. The magnitude of stress depends on the material and on the deposition conditions. It is possible to select

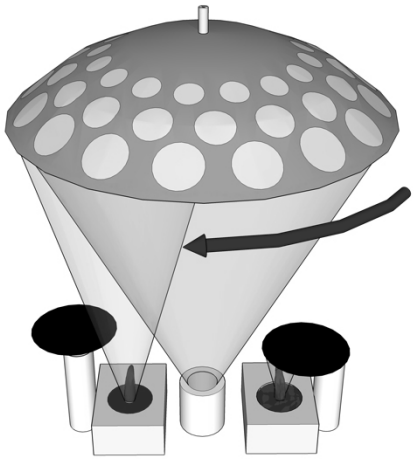

Fig 1.1.5.2.1 IAD coating plant.

material and process parameters so that the stresses of various layers counteract each other. In contrast, almost all ion plated layers are under compressive stress. Therefore, it is more difficult to produce stress-compensated multilayer coatings by this process.

### 1.1.5.3. IBS coating process

Fig 1.1.5.3.1. IBS coating plant.

Sputtering in general is removal of atomized material from a solid due to energetic bombardment of its surface layers by ions or neutral particles. In ion - beam sputtering (IBS), an energetic beam of inert ions is aimed at a target made of the material that is to be deposited [33]. Atoms or clusters of atoms of the material are dislodged from the target and land on substrate with a high energy. This is the slowest physical vapor thin-film deposition method described here and it cannot be readily scaled for the coating of large components. However, it yields the highest quality coatings. Films prepared by IBS method have excellent properties of thermal, chemical stability and high dielectric constant, so they could widely benefit many applied science and technological branches. Many of the high-reflectance coatings for laser gyros, with no significant losses tolerated, are produced in this way.

### 1.1.5.4. Magnetron sputtering coating process

Reactive or nonreactive DC or RF magnetron sputtering (MS) is also used to deposit optical multilayer coatings [34]. Reactive sputtering means sputtering of an elemental target in the presence of a gas that will react with target material to form a compound. In one sense all sputtering is reactive because of residual gases in chamber that would react with sputtered species. However, in reality reactive

sputtering occurs when purposely added gas reacts with the sputtered material. For example, when oxygen is injected into the chamber with the sputtering of aluminum to form aluminum oxide or when nitrogen is added with the sputtering of titanium to form titanium nitride [35]. Many modifications of magnetron sputtering exist. Most are significantly slower than evaporation and targets can be quite expensive. By using magnets behind the cathode to trap free electrons in a magnetic field directly above the target surface, these electrons are not free to bombard the substrate to the same extent as with diode sputtering. At the same time extensive, circuitous path carved by these same electrons trapped in the magnetic field, enhances their probability of ionizing a neutral gas molecule by several orders of magnitude. This increase in available ions significantly increases the rate at which target material is eroded and subsequently deposited onto the substrate. However, the process is stable, provides excellent control over the thicknesses of the layers, and can be readily scaled to provide uniform coatings over large areas. Both metal and metal oxide layers can be produced. Sputtering is an energetic process and results in dense, bulk-like layers which exhibit virtually no ageing.

Fig. 1.1.5.4.1. MS coating plant.

### 1.1.5.5. Sol-gel coating process

A simple process for preparation of broadband anti-reflective single-layer silica films is sol-gel method. This technique is based on a transparent liquid containing nanometer sized particles deposition by using spin-coating or dip-coating techniques. Drying is used afterwards in order to stabilize produced layer. Typically preparation of PVP-containing $SiO_2$ sol is made by using [36] an ammonium hydroxide catalyzed hydrolysis and condensation of tetraethoxysilane (TEOS) in the ethanol solution of PVP at 20 °C. TEOS (99%), PVP, anhydrous

ethanol and pure water are used in such preparation. At first, PVP should be dissolved in ethanol for a concentration of 0.1 wt.%. Then TEOS, water and aqueous solution of ammonium hydroxide (15 mol/l) should be added to the ethanol solution of PVP. The final concentration of $SiO_2$ typically should be of 3 wt.% and the pH of sol must be adjusted to 7.5. After one and a half month aging in a hermetically sealed chamber at 20°C, the as-synthesized PVP containing $SiO_2$ sol can be used to deposit glass or other samples using *spin-* (Fig. 1.1.5.5.1) or *dip-coating* methods. *Spin-coating* is a cheap and fast method to produce homogeneous layers. An excess amount of the solvent is placed on the substrate, which is then rotated at high speed in order to spread the fluid by centrifugal force. The film thickness can be adjusted by varying the rotation speed, rotation time, and the concentration of used solution. The disadvantage of this method is that it is limited by the solvent and that no lateral resolution is possible. *Dip-coating* technique is a process where the substrate to be coated is immersed in a liquid and then withdrawn with a well-defined withdrawal speed under controlled temperature and atmospheric conditions. The coating thickness is mainly defined by the withdrawal speed, by the solid content and the viscosity of the liquid. Coatings prepared by sol gel method are typically porous and have very good optical resistance compared to other methods.

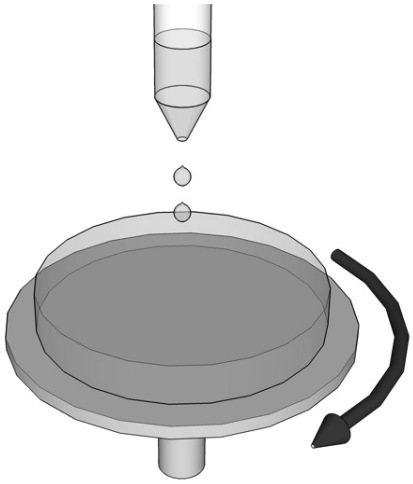

Fig 1.1.5.5.1 Spin-coating process.

## 1.1.6. Coating defects and layer growth microstructure

Both the substrate and the coating influence optical characteristics of a coated component. The LIDT's of even identical coating materials and designs on nominally identical substrates, which have been prepared and cleaned under similar procedures, are affected by differences in coating deposition processes.

The resistance to optical radiation of dielectric coatings by means of material content and nanostructure can be assigned to two major groups:

1. pure materials – maximal *intrinsic* damage threshold limited: attributed to fundamental limits of pure, mainly crystalline, materials.
2. polluted or inhomogeneous, randomly structured materials – *extrinsic* damage threshold limited: attributed to materials having impurities or structural lattice defects. Such coatings have lower damage threshold than those of pure materials and contains an additional transient levels within the band-gap.

However, up to now in most of the coatings produced by conventional deposition techniques laser-induced damage has been observed to be the result of absorbing inclusions [37-42] inside the damaged material. Different characteristics of the defects determine the damage mechanism under laser radiation. This chapter shortly presents known extrinsic enhanced absorption reasons which may lead to laser-induced damage in dielectric coatings at lower than intrinsic damage limited energy fluencies.

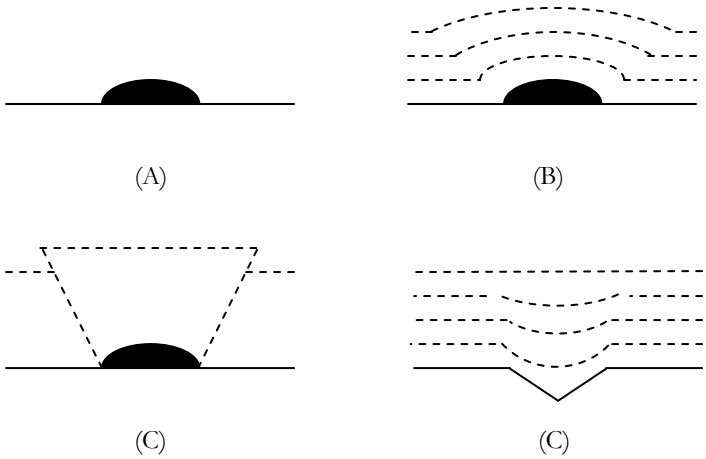


Fig. 1.1.6.1 Coated surface defects.

Most of abovementioned deposition techniques replicate surface shape, including scratches and material lumps [37, 41]. Irregularities of plane surfaces are only gradually smoothed out at the expense of either increasing the number of voids or

modified local refractive index. Some of common problems associated with the coating run are illustrated in (Fig. 1.1.6.1). In the case of a lump (A) bigger than normal droplet of the material is deposited, then (B) thin layers of atomic layers are deposited. As it is shown in (Fig. 1.1.6.1, B), layer by layer stack only gradually evens the surface. The resulting structure either replicates itself into (C) a lens-like structure or, if the coating has crystal structure, forms a cone shaped inclusion (nodular defect) of different refractive index. Both of these structures can result in extra focusing of transmitted light which in extreme cases results in laser induced damage [37-39]. By investigations of such defect ageing it was shown that the size of nodular defects increases with the time in particular due to exposure to the atmosphere. This results in reduction of LIDT whilst having little or no effect on the absorption and reflectance. In the case of scratches and digs the deposited coatings fill gaps with a lower density of material than the average coating. It means that over the dig typically there are more voids than in surrounding coating. The local reflection characteristics are modified in this region.

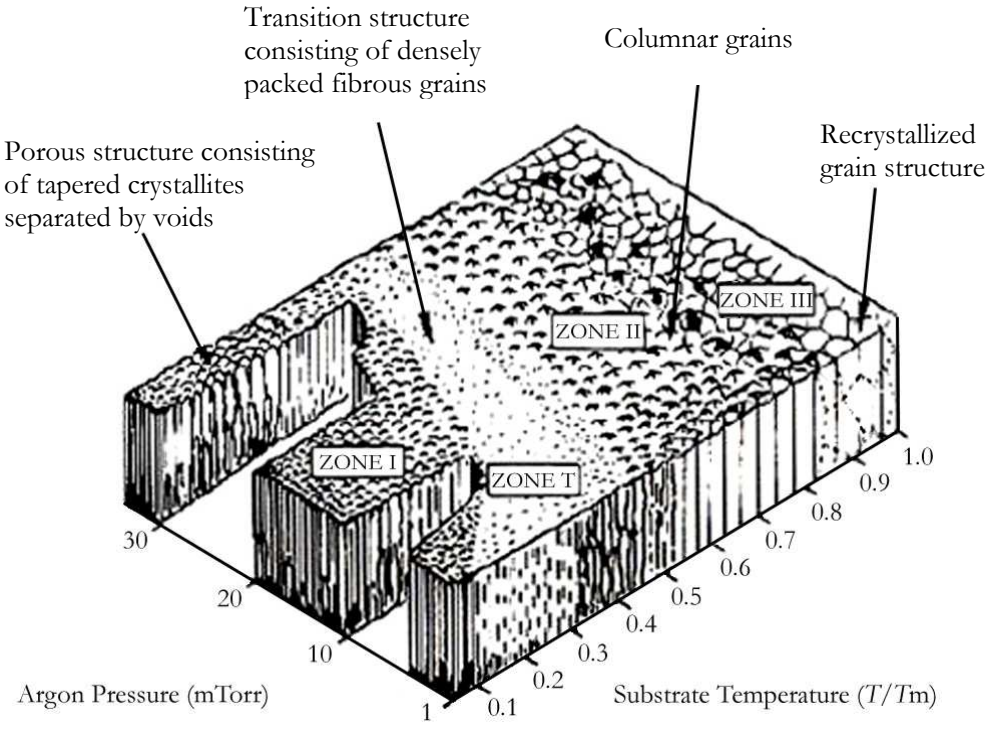


Fig. 1.1.6.2 The Thornton Structure Zone Model [43-45].

Another interesting feature of thin film preparation by PVD technique is a wide range of crystalline properties of deposited layers. Structure zone model (SZM) based on experimental investigations (Fig 1.1.6.2) was developed in order to relate the microstructure of a thin film to the temperature of substrate $T$ and melting point $T_m$ of coating material [43-45]. According to this model micro-structural development is in turn controlled by shadowing effects (zone 1), surface diffusion (zone $T$ and zone 2) and bulk diffusion (zone 3) as $T/T_m$ increases. This model explains why the microstructure is independent of the particular method of vapor deposition used to prepare film. At $T/T_m$, <0.l there is little adatom surface mobility, and initial nuclei tend to grow in the direction of available coating flux. The growth morphology is affected significantly by inter-grain shading. Tapered crystallites develop. Inter-grain boundaries are voids rather than true grain boundaries, so that coatings have poor lateral strength and are under-dense, although individual crystallites have near bulk density. At higher $T/T_m$ (0.1-0.3) self-diffusion becomes appreciable, and coatings consist of a dense array of fibrous grains separated by more nearly conventional grain boundaries, probably due to the occurrence of sintering type coalescence during growth. Such coatings yield high lateral strengths. Above $T/T_m$ (~0.3-0.5) surface mobility is even greater and grain boundary migration and recrystallization is possible. Columnar grains extending through the entire coating thickness and separated by true grain boundaries develop, possibly by surface recrystallization during the growth. Surfaces tend to be faceted in $T/T_m$ range (0.5–0.75). Greater tendency for developing faceted surfaces in hollow cathode at moderate $T/T_m$ is believed to be due to relatively low energy (30-50 eV) ion bombardment etching and oblique flux of coating atoms. At very high $T/T_m$ (~0.75) equilibrium surface structure apparently consists of relatively flat grain tops with grooved grain boundaries in both apparatuses. The adsorption of a solid substrate (adsorbent) is a capability to attract molecules of gas or vapor (adsorbate) when they are in contact with the surface. It depends on Van Der Waals forces of attraction between molecules. The non-ideal crystal structure causes the so-called defect sates of self trapped excitons and forms additional absorption bands corresponding to the transition

levels inside the forbidden band-gap [46]. For example, in crystal quartz the defects are produced by displacement of atoms in the lattice. The primary defect is oxygen vacancy: its positive state is called *E'* center and contains one electron which localizes onto one of the Si atom ($\equiv Si \bullet$). Another type of defects in $SiO_2$ are so called non bridging hole centers ($\equiv Si - O \bullet$). The properties of those defects have been studied in [46-48].

## 1.2. The method of optical resistance testing and experimental set-up

### 1.2.1. Definition of LIDT and test procedure

Metrology and characterization of laser-induced damage threshold is of major importance for high intensity laser development. Metrology (from Greek *metro*- measure, *logos* -study) is the science of measurements, methods and means for providing their unanimity and adequate accuracy. The optical resistance of laser component is characterized in terms of critical amount of electromagnetic radiation which can cause the optical damage. Long time after invention of the first lasers there were no adequate standards by which scientists or laser manufacturers could specify the power levels at which they expected components perform without damage. Only at the end of the last century the International Organization for Standardization has published an International Standards entitled *Test Method for Laser Radiation Induced Damage Threshold of Optical Surfaces* (ISO11254-1 and ISO-11254-2) [12, 13]. Those standard procedures are based on the damage frequency method [49-51] and allow the classification of optics according to the laser power resistance. Damage threshold is determined by linear extrapolation of the measured energy-density dependent damage probability as function of incident laser pulses. In this chapter a short description of a testing procedure and its theoretical background will be given. In both standards the definition for laser-induced surface damage is the same:

*..any permanent laser radiation induced change of the surface characteristics of the specimen which can be observed by an inspection technique described within this International Standard. <…> A microscope technique shall be used to inspect the surface before and after the test. The investigations shall be made with an incident light microscope having Nomarski-type differential interference contrast. A magnification in the range from 100x to 150x shall be used* [12, 13].

The definition above is used in this work. It seems obvious that the damage observed can be characterized as a sudden irreversible material modification due to laser irradiation. However, this definition is not absolute in terms of resolution and sensitivity of damage detection and inspection technique. For example, the resolution of conventional optical microscopy is limited approximately by a wavelength of electromagnetic wave, therefore, the observable damage is not smaller than ~100 nm [52, 53]. Essential feature of the reflected light differential interference contrast *Nomarski* microscopy is that both sheared orthogonal wavefront components reflect from the specimen, separated only by fractions of a micrometer (the shear distance), which is much less than the resolution of objective. It is not apparent to an observer that resulting image visualized in the eyepieces is composed of these two superimposed components, because their separation is too minute to be resolved by the microscope. However, each point in the image is derived from two closely spaced and overlapping Airy disks originating from adjacent points on the specimen. Each disk has the intensity that corresponds to its respective optical path difference induced by specimen. Image contrast is described as being differential because it is a function of optical path gradient across the specimen surface, having steeper gradients and producing greater contrast. High resolution depending on shear distance afforded by the *Nomarski* technique has been employed to ascertain specimen details limited by just a few tens of nanometers in height and approximately ~100 nm wide [53]. In the most general case laser-induced material changes can appear even in atomic scale. The techniques capable to detect extremely small structural material changes such as scanning electron microscopy (SEM) or atomic force microscopy (AFM) differs strongly in their sensitivity and detection speed. However, the ISO

standard must be implemented at reasonable cost [51] for manufacturing environment, therefore, the choice of *Nomarski* microscopy in the definition of damage is rather technical trade-off between testing speed, accuracy and price.

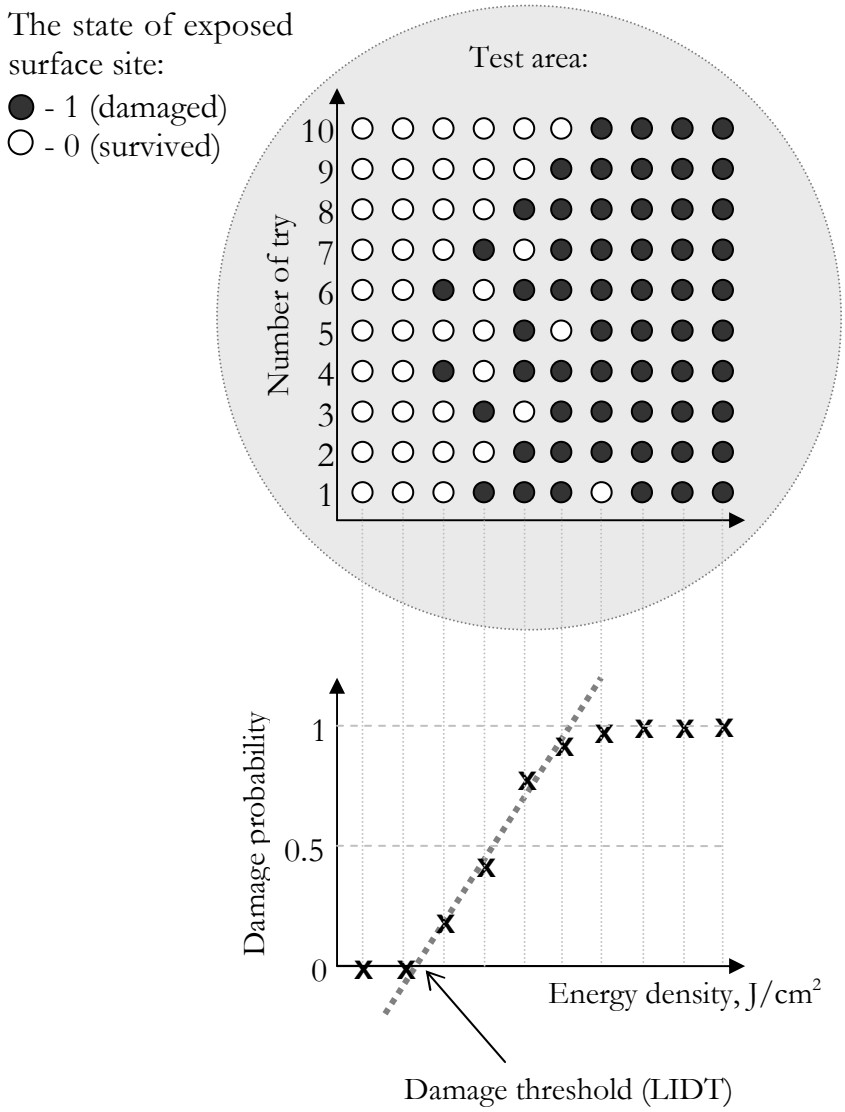


Fig. 1.2.1.1 Damage frequency method.

Testing of optical resistance is a destructive procedure based on damage frequency method (DFM). In most cases the occurrence of optical damage is rather probabilistic [54] in nature and can be characterized in terms of damage frequency (probability) [12, 13, 49, 50]. If the component is exposed under the laser radiation it may or may not be damaged. Consider ten different sites of a sample exposed under identical laser pulses. Some sites are damaged after the

irradiation and some of them not. The damage probability (frequency of occurrence) at given energy density of pulse is then given by a ratio of damaged sites to the total amount of tested sites. In DFM the damage probability is measured as a function of laser pulse energy density (Fig. 1.2.1.1). For the whole LIDT test procedure a minimum of 10 sites should be tested for each energy density or power density increment and the range of pulse energies (or beam power) must be sufficiently broad to include points of zero damage frequency, as well as points of 100 % damage probability. After being exposed, test sites are inspected microscopically to confirm damage and characterize laser-induced changes. From damage statistics the damage frequencies (probabilities) are estimated for each energy density and a damage threshold can be determined. This method provides the most accurate measurement of a damage threshold, but requires a relatively large sample [55], since many sites must be exposed. However the procedure is applicable to the testing with all laser systems irrespective of pulse length and wavelength.

According to this method the definition of *laser-induced damage threshold* (LIDT) is:

*the highest quantity of laser radiation incident upon the optical surface for which the extrapolated probability of damage is zero. The quantity of laser radiation may be expressed in energy density* $H_{max}$ *or power density* $E_{max}$

Standards ISO 11254-1 and ISO 11254-2 distinguish between 1-*on*-1 and *S*-*on*-1 test procedures. For the *S*-*on*-1 procedure, a train of equal pulses impinges on one test site. In the case of the 1-on-1 test, every site of the sample is irradiated by only one laser pulse of a certain pulse energy density. Therefore, 1-*on*-1 test delivers only rough estimations for the LIDT and *S*-*on*-1 method can be employed to assess the long-term optical resistance.

## 1.2.2. Experimental set-up

*Material related to this chapter was published in* [A1-A22] *and* [C1-C27].

As a part of this work a metrological facility meeting the requirements of ISO standards [12, 13] has been built at Laser Research Center of Vilnius University (Fig. 1.2.2.1). The approach to laser damage testing is shown in (Fig. 1.2.2.2). LIDT of optical components is strongly dependant on special operation conditions of the laser system.

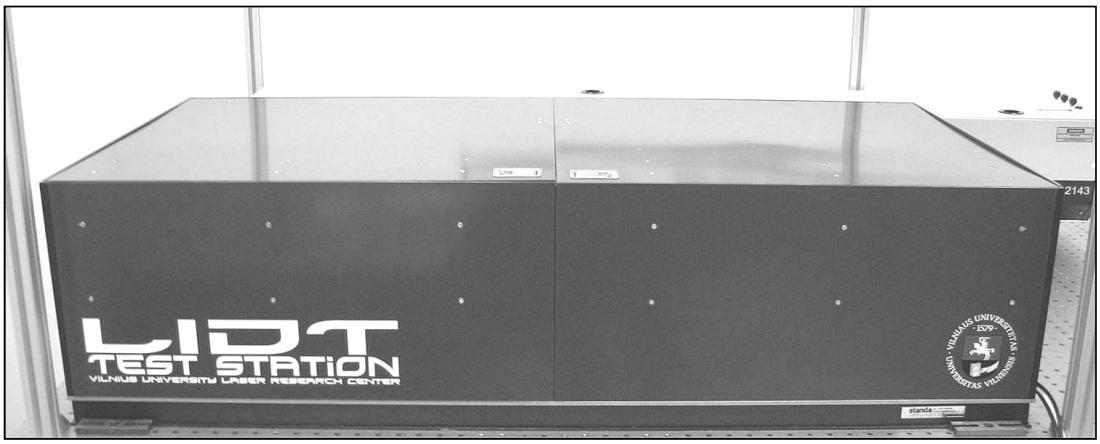


Fig. 1.2.2.1. LIDT test station at VULRC.

Therefore, to get the most meaningful results, test parameters should be as close as possible to the intended laser operation conditions such as wavelength, pulse duration and repetition rate. Lasers of nanosecond and femtosecond pulse durations are very often applied in laser technology nowadays. In order to cover pulse durations of interest the LIDT test station is equipped with two laser systems (use of the other laser systems is also available). The first one is a flash lamp pumped, Q-Switched Nd:YAG laser (*NL301G*, *Ekspla*) with a second, third and fourth harmonic units and a possibility of selecting the repetition rate from 0.5 Hz up to 10 Hz. Pulse duration (FWHM) value, measured for the first harmonic (1064 nm) is about 3.4 ns. Temporal beam profile is shown in (Fig 1.2.2.3, A). Spatial beam profile measured in target plane is close to Gaussian (Fig. 1.2.2.3, B). Maximal energy of pulses is ~240 mJ. The second laser source is a femtosecond Ti:Sapphire laser system (*Super Spitfire, Spectra-Physics*) based on

chirped-pulse-amplification (CPA) technique. The master laser is a Ti:Sapphire based Kerr lens mode-locked oscillator pumped by a continuous-wave visible laser. Further the chirped pulse amplifier is pumped by two diode-pumped Nd:YLF lasers.

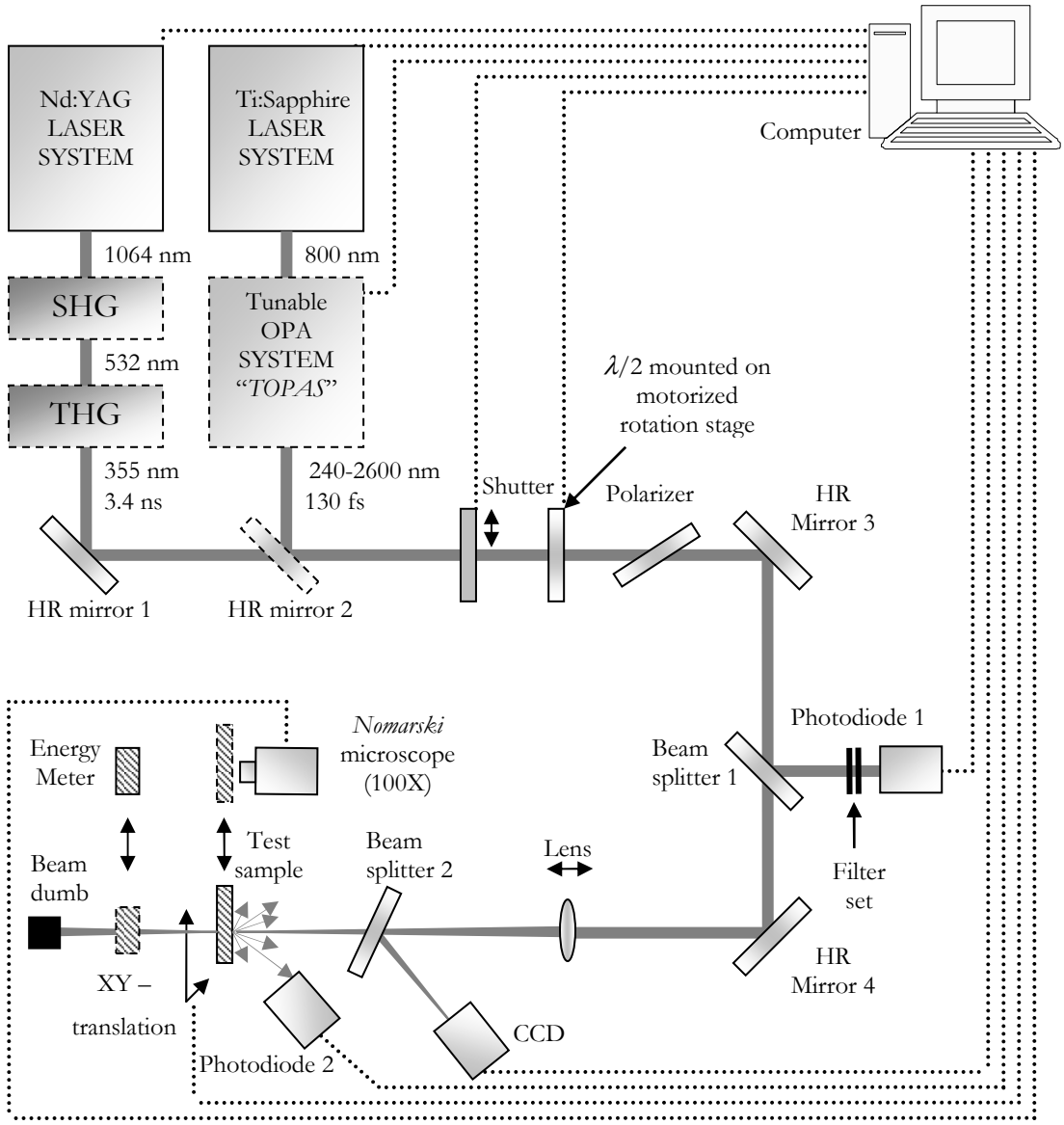


Fig. 1.2.2.2. Schematic illustration of the *S-on*-1 LIDT test station.

The output energy of the laser is gained up to 2.3 mJ at 1 kHz repetition rate and central wavelength 800 nm. The estimated duration (FWHM) of output pulses is approximately 130 fs (Fig. 1.2.2.3, C). Repetition rate of the amplified pulses can be tuned from 1 Hz up to 1 kHz. A typical spatial beam profile measured in target plane of the amplified pulses is shown in (Fig. 1.2.2.3, D). A collinear traveling-

wave optical parametric amplifier (*Topas, Light Conversion*) is attached to the system in order to extend the tuning range of wavelengths: from 240 nm to 2600 nm.

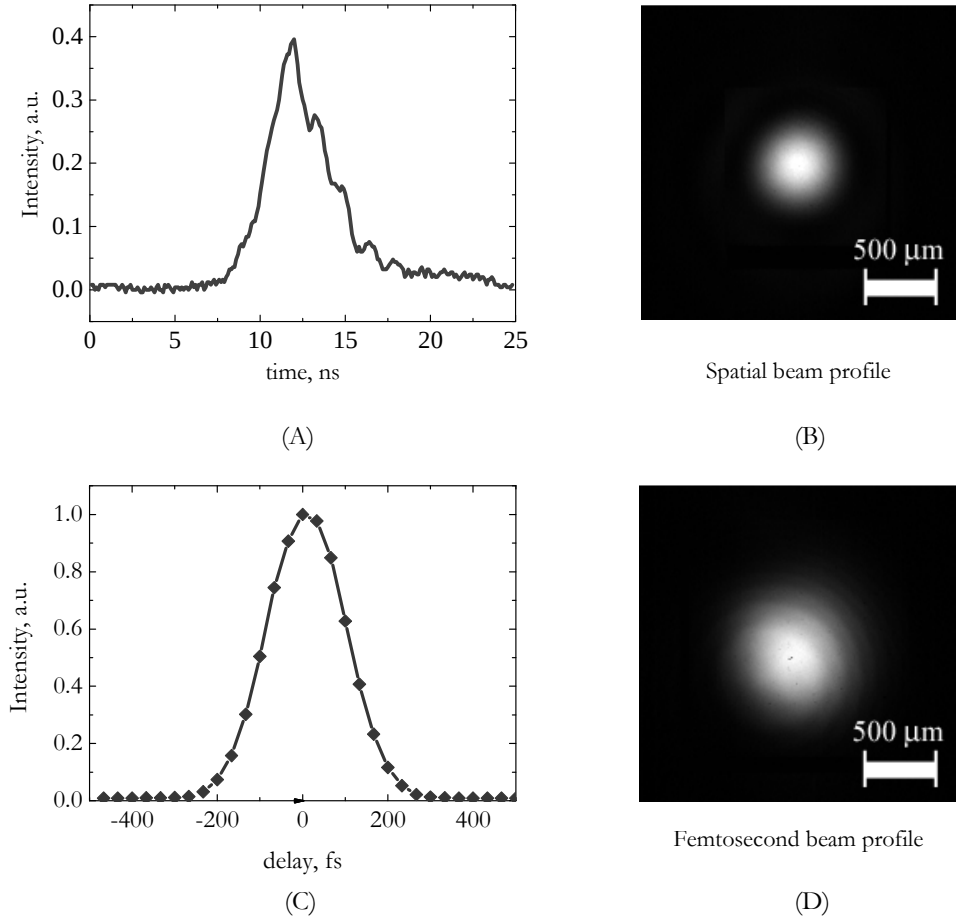


Fig. 1.2.2.3. A and B – temporal and spatial profiles of the pulses generated by the Nd:YAG laser; C and D – multi-shot autocorrelation curve and spatial beam profile of the Ti:Sapphire laser.

The maximal pulse energy is wavelength-dependant; however, in most cases it is sufficient to induce optical damage. Computer-controlled mechanical shutter and the attenuator are placed behind the laser systems and high reflectivity mirror (Mirror 1 or Mirror 2). Shutter controls the amount of incident laser pulses. The output of a well-characterized stable laser source is set by software to the desired energy or power with a motorized attenuator consisting of a half-wave plate and a Brewster type polarizer. Contrast exhibits a 1000:1 extinction ratio and the transmission loss of the energy of about 4%. Photodiode 1 (*S1337-1010 BQ, Hamamatsu*) and attenuator position is calibrated with commercial energy meter (*LaserStar, Ophir*). Focusing system permits concentration of laser radiation to the

destructive energy or power density at the test specimen. The specimen is mounted in a 2-axis (XY) manipulator which is used to position separate test sites under the laser beam and set the angle of incidence. The spot size of the laser beam is controlled by the choice of lens which focus the beam on the sample. Another beam splitter (beam splitter 2) is used to direct a small portion of beam to a CCD matrix for purpose of monitoring the intensity distribution at focus. Polarization state if necessary is set with an appropriate phase retardation plate placed in front of the specimen. To determine the damage threshold, a number of sample sites are irradiated at different fluencies. The occurrence of damage is automatically recognized by the optical scattering technique. The detector registering increase of the scattered light (photodiode 2) is connected to the shutter controller in order to block radiation immediately after damage (scattering) occurs. The typical signal of back-scattered light from test surface is shown in (Fig. 1.2.2.4).

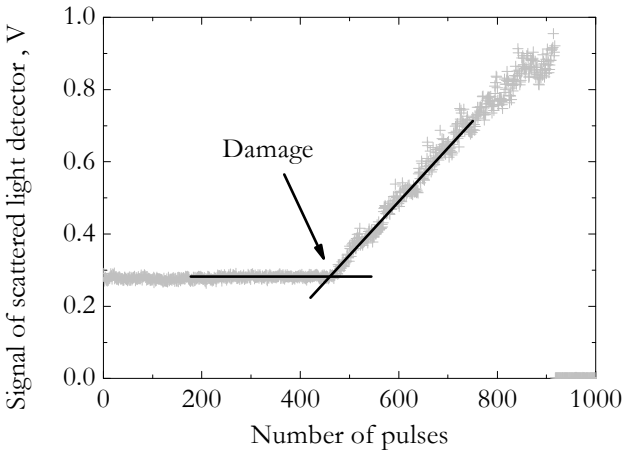


Fig. 1.2.2.4. The typical signal registered by scattered light detector.

Each site is observed before and immediately after irradiation with the *Nomarski* microscope (*100x*). During the measurement any visible change, plasma formation, or change in scatter of the laser beam is noted. The entire experimental set-up was placed in a special chamber with enhanced clean air pressure in order to prevent contamination of the sample by air dust. All data is stored and analyzed by computer.

## 1.2.3. Software for controlling the LIDT measurements

In order to automate and control the LIDT measurements the interface program based on the graphical programming language (*LabView, NI*) was created. The aim of the computer program was to speed up the *S-on*-1 or 1-*on*-1 measurement procedure and minimize human resources. Before starting the measurement the sample must be placed into a sample holder and laser must be switched on.

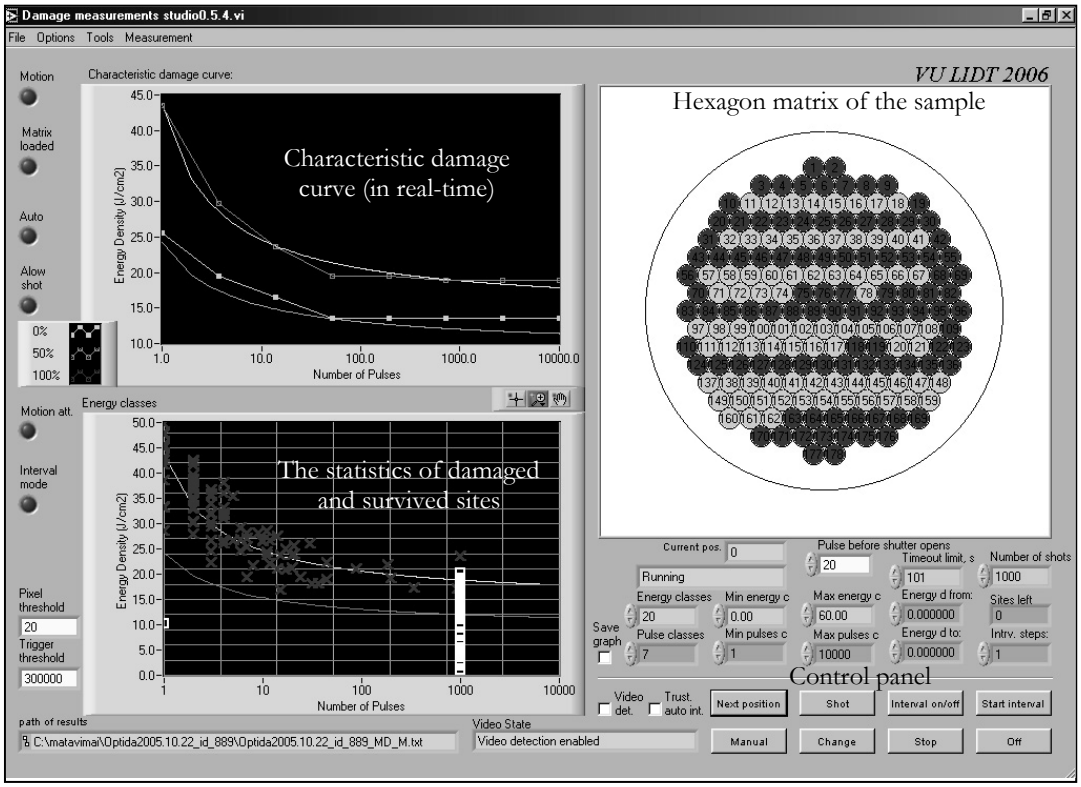


Fig. 1.2.3.1. Front panel of developed LIDT measurement software.

Thereafter a calibration of attenuator and the measurement of laser beam diameter are performed. Then the *S-on*-1 measurement procedure is initialized and the surface area of a specimen is automatically divided into cells of a hexagonal matrix (Fig. 1.2.3.1): minimal distance between test sites is considered to be at least three times higher than beam diameter ($1/e^2$). The software controls the whole procedure of the *S-on*-1 measurement. The positioning of experimental sample in *X* and *Y* directions, adjusting of laser energy, shutter control, monitoring and recording of incident energy density of pulses are performed automatically. Special algorithm recognizes damage when it occurs by change in

scattered light signal monitored by a photodiode. The program is also capable of saving measurement data (state of the surface, number of pulses before damage, energy of each pulse and position coordinates of the point). Finally, when damage inspection is done, characteristic damage curve is calculated.

### 1.2.4. The accuracy of measurements

The uncertainty and error of damage threshold is influenced by accuracy of all the detection and measuring systems. These errors [56, 57] are clearly defined and can easily be described. Below the calculation of damage probability and energy domain errors for 1-*on*-1 measurement $\sigma_P^2$ and $\sigma_I^2$ are shortly introduced respectively. The reported value of damage frequency $P$ for fixed energy density $I$ is calculated from the formula [56]:

$$P = \frac{d}{n+d} \tag{1.2.4.1}$$

where $d$ is the number of damage sites observed at a specific fluence and $n$ is the number of sites that are irradiated with no observed damage. Using a propagation of error argument, the variance of $P$ is given by:

$$\sigma_P^2 = \left(\frac{\partial P}{\partial n}\right)^2 \sigma_n^2 + \left(\frac{\partial P}{\partial d}\right)^2 \sigma_d^2 \tag{1.2.4.2}$$

If in damage frequency method (ISO), sites are continually exposed until $d$ damages are observed, thus $d$ is fixed reducing (1.2.4.2) to:

$$\sigma_P^2 = \left(\frac{\partial P}{\partial n}\right)^2 \sigma_n^2 \tag{1.2.4.3}$$

The variance in $n$ is given by the variance in number of trials in the negative binomial distribution to get $d$ successes:

$$\sigma_n^2 = \frac{d\left(1-\frac{d}{N}\right)}{\left(\frac{d}{N}\right)^2} \tag{1.2.4.4}$$

where sum of $n$ and $d$ is $N$ the total number of sites exposed at a given fluence $I_i$.

The partial derivative in (1.2.4.3) is

$$\frac{\partial P}{\partial n} = \frac{-n}{N}. \tag{1.2.4.5}$$

Substituting (1.2.4.5) and (1.2.4.4) into (1.2.4.3) gives

$$\sigma_P^2 = \frac{nd}{N^3}. \tag{1.2.4.6}$$

Equation (1.2.4.6) can be rewritten in terms of the probability of damage $P$ using the definition (1.2.4.3), namely

$$\sigma_P = \sqrt{\frac{P(1-P)}{N}}. \tag{1.2.4.7}$$

Fractional uncertainty in observed damage probability is $\varepsilon_P$:

$$\varepsilon_P^2 = \frac{\sigma_P^2}{P^2} = \frac{n}{dN} \tag{1.2.4.8}$$

The variance in the fluence, $\sigma_I^2$ is [57]:

$$\sigma_I^2 = \left(\frac{\partial I}{\partial A}\right)^2 \sigma_A^2 + \left(\frac{\partial I}{\partial E}\right)^2 \sigma_E^2 \tag{1.2.4.9}$$

Where $A$ is the effective area and $E$ is the energy of the laser pulse

$$\sigma_I^2 = I^2\left(\varepsilon_E^2 + \varepsilon_A^2\right) \tag{1.2.4.10}$$

The uncertainties for both lasers which are used in our experiments are given in the Table 1.2.4.1.

Table 1.2.4.1. The budget of measurement errors.

| Error source | NL301G | Super Spitfire |
|---|---|---|
| Pulse-to-pulse random variations | | |
| Energy stability | ± 1-3.5 %* | 1.5 % |
| Spatial profile diameter stability | ± 3 %* | 2 % |
| Systematic variations: | | |
| Calorimeter calibration | ±3 % | ±3 % |
| Calorimeter-energy monitor correlation | ±2 % | ±2 % |

* depends on the wavelength

Errors which are intrinsic to the procedure [51] cause much more problems. For example, it is hardly possible to quantify the influence of errors in determination of the damage probability at a given energy-density on result of the extrapolation. This is a problem because the basic assumption is that all testing sites show an identical behavior. However, there are examples [58] which show the presence of different types of defects and therefore complicated damage probability functions. Moreover, depending on the arrangement of testing sites on the sample largely diverging damage frequencies can be measured if the sample is inhomogeneous. Since the homogeneity cannot be tested by an independent method, possibility of a certain inhomogeneity has to be taken into account. The consequences can hardly be quantified. Finally, selection of measured values on which the extrapolation should be based is a subject to a certain arbitrariness [12, 13, 59]. A lot of experience and sense of responsibility is necessary to manage the procedure of damage threshold evaluation.

## 1.2.5. Conclusion

An automated metrological facility for *S-on*-1 laser-induced damage threshold measurements was developed. It minimizes the influence of human factors and speeds up the LIDT measurements. The sensitivity of assembled metrological facility using femtosecond pulses is sufficient for the determination of various factors (deposition technique parameters and materials) on LIDT of optical coatings.

# 2. The effect of pseudo-accumulation: theory and experiment

*Material related to this chapter was published in* [A21] *and* [C26, C27].

The determination and interpretation of damage threshold as a function of the number of pulses on a specific optic element is a classical problem in laser damage studies. It has been known that material surfaces, irradiated with multiple high-power laser pulses, become damaged at pulse energies far below the single-shot damage threshold. There are a few models of fundamental mechanisms explaining the accumulation-like behavior of LIDT: defect incubation - changes in electronic or chemical material structure during laser-matter interaction and temperature increase due to pulse-to-pulse heat accumulation. In this chapter a new additional statistical phenomenon is introduced and discussed: the *pseudo-accumulation* effect on the laser-induced damage probability. It manifests itself at specific optical jitter cases and defect densities. Computer simulation of *S-on-1* (*S* shots on the single test site) [13] tests show a behavior similar to that of a true accumulation or incubation effect. We do not insist that our proposed model of pseudo-accumulation is the main and the only one responsible for accumulation like behavior. Our goal is to show the role of angular propagation and fluency fluctuations (jitter) of repetitive laser radiation and its relation with the accumulative damage probability. In our simulations, defect induced damage is assumed and a degenerate defect model is applied. The influence of this effect exists in addition to any true physical accumulation in the sample. After neglecting both effects: pulse to pulse heat accumulation and incubation of new defects by absorbed laser light our model based on statistical accumulation still leads to results similar to that of heat accumulation. The statistical nature of the effect, in fact a false accumulation, leads to the name pseudo-accumulation effect. It is demonstrated that the pseudo-accumulation is the result of temporally and spatially unstable laser radiation in transparent dielectrics containing some absorbing inclusions of negligible size compared to the beam width in $1/e^2$ level

of peak irradiance. Experimental results are introduced to illustrate the theoretical results. In order to show the clear role of the statistical accumulation only, we model the *worst case* cumulative damage probability corresponding to the beam scanned area by spatially and energetically unstable multiple laser pulses. Then we simulate the *S-on-1* measurements and compare the results with experimentally obtained data. The fundamental elements of this model are:

- Absorbing defects are randomly distributed on the surface and they are of negligible size compared to the test laser beam width ($1/e^2$);
- Laser-induced damage occurs when the defect is irradiated by the laser beam having local fluence of $T_{defect}$ (*defect damage threshold*) critical to the defects or higher.
- The surface returns to room temperature before the next pulse (no pulse-to-pulse heat accumulation)
- No new defects are created because of repetitive irradiation of the same site (no defect incubation).

## 2.1. The degenerate ensemble of damage precursors

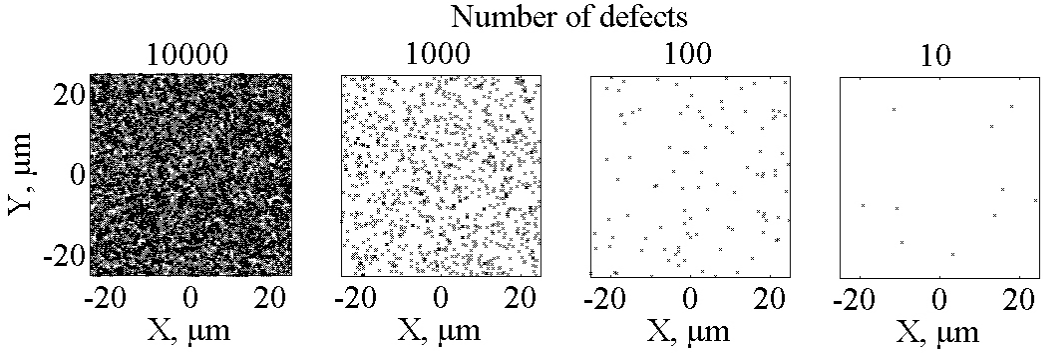


Fig. 2.1.1 Simulated spatial distributions of random surface defects at various defect densities.

The presence of submicron sized defects in high quality optical coatings[1] can be determined by the means of experimental methods such as fluorescence

[1] For simplicity reasons attention only to the surface defects is paid and bulk defects are neglected. However the bulk defects will lead to very similar computer simulation results.

spectroscopy [60], optical coherence tomography [61], analysis of the laser-induced damage morphology and damage statistics [62] as well as the raster scanning absorption-deflection methods [63-66]. It is important to understand that laser irradiation of these defects (damage precursors) initializes damage process by the absorption of laser energy [67] at lower than intrinsic damage fluency of hosting matrix. The absorption causes free electron generation, ionization and thermal expansion, shock wave generation and other effects leading to damage. Moreover, repetitive laser pulses can also introduce new defects [47, 68, 69] thus changing the probability of damage and causing the so-called incubation effect. Defect types and densities are strongly dependant on coating manufacturing conditions and the manufacturing technologies themselves [70, 71]. However, direct characterization of absorbing defect density and their positions are still technologically difficult and time consuming tasks. The spatial resolution of such measurements is typically not higher than the wavelength of tightly focused scanning beam. In general, defects may have individual damage threshold values. The population of defects is then specified by the ensemble function $f(I)$, which multiplied by $\mathrm{d}I$ gives the number of defects per unit area that damage at fluence between $I$ and $I + \mathrm{d}I$. The simplest possible ensemble $f(I)$ is when all defects fail at the same fluence. This is the so-called degenerate defect distribution. This kind of distribution is represented by a delta function (2.1.1) at $I = T_{defect}$ when all defects are distributed uniformly on the surface:

$$f_{degenerate}(I) = M\delta(I - T_{defect}) \tag{2.1.1}$$

where $M$ is the normalizing constant which represents the surface defect density. This model is applicable to the wide range of samples and will be used in further simulations. A more complex (nondegenerate) defect ensemble model descriptions involving power-law [72] and Gaussian [62] are also known and they have practical meaning but will not change the essence of pseudo-accumulation phenomena which is described below. For the purpose of illustration the

computer simulated randomly distributed spatial defects with different surface densities are shown in (Fig. 2.1.1).

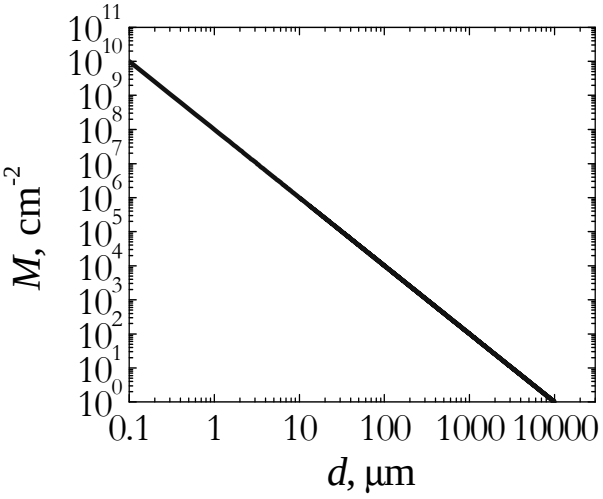


Fig. 2.1.2. Surface defect density $M$ versus average distance $d$ between neighbor defects.

Another very important parameter characterizing defects is the average distance between neighbor defects $d(M)$. In order to estimate the order of magnitude of this parameter the rough assumption of the square surface defect lattice is made:

$$d(M) = \sqrt{\frac{1}{M}} \tag{2.1.2}$$

The graphical result of the formula (2.1.2) is shown in (Fig. 2.1.2).

## 2.2. Porteus and Seitel model: 1-*on*-1 damage probability

In order to estimate the influence of the random beam hopping (spatial laser jitter) on the LIDT measurement for materials containing nanometer sized defects the mathematical approach of 1-*on*-1 damage probability should be considered. The simplest physical model that relates 1-*on*-1 damage probability and defect density was firstly proposed in early 1980s by J.O. Porteus and S.C. Seitel. The main idea of their study [72] was the definition of defect ensembles and their relation with Poisson statistics to derive a universal regression function for

damage testing. Consider surface defects of degenerate ensemble (2.1.1) are under the focused laser beam (Fig. 2.2.1). The fluence of the incident beam is assumed to be Gaussian:

$$I(r) = I_0 \exp\left(-\frac{2r^2}{w^2}\right) \tag{2.2.1}$$

where $I_0$ is the peak fluence (or energy density), $r$ radial coordinate and $w$ - is Gaussian beam radius at $1/e^2$ level of $I_0$.

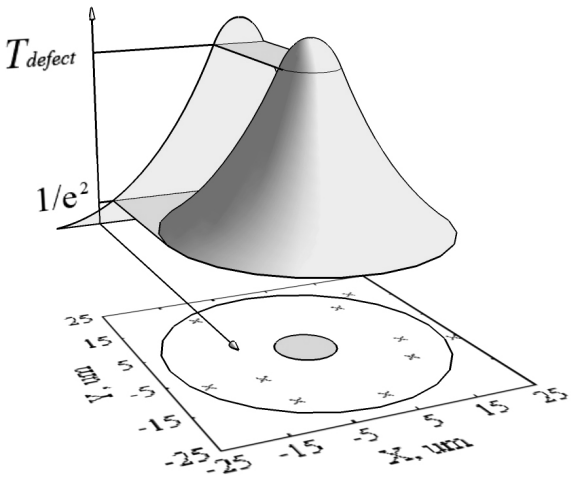


Fig 2.2.1. The coverage of randomly distributed defects by a Gaussian beam ($TEM_{00}$ mode). Outer solid line surrounded circle of radius $w$ denotes the area above $1/e^2$ level of Gaussian beam; Filled circle in the middle is the area where the energy density is higher than $T_{defects}$.

Note that the area where the fluence is above threshold $T_{\text{defect}}$ varies with peak energy density $I_0$ [58]:

$$a(I_0, w, T_{defect}) = 0.5 \cdot \pi w^2 \ln\left(\frac{I_0}{T_{defect}}\right) \tag{2.2.2}$$

As $a(I_0, w, T_{defect})$ increases the average number of defects $n$ within this area also increases thus increasing the probability of damage. The radius or area a is given by

$$r_a = w\sqrt{\frac{1}{2}\ln\left(\frac{I_0}{T_{defect}}\right)}. \tag{2.2.3}$$

The probability of damage in a single shot, $P(I_0)$, is given then by Poisson statistics:

$$P = \begin{cases} 0, & I_0 < T_{defect} \\ 1 - \exp(-n), & I_0 \geq T_{defect} \end{cases} \quad (2.2.4)$$

where

$$n = a(I_0, w, T_{defect}) \cdot M \quad (2.2.5)$$

is the average number of degenerate ensemble defects within the laser spot that are damaged at fluencies above $T_{\text{defect}}$. This probability represents the *best case* – the highest damage threshold of the sample. In the case of real accumulation the probability curve for multi-pulse mode can only be *shifted* towards the lower energy density. It will not change if there is no accumulation.

## 2.3. Derivation of cumulative damage probability

The 1-*on*-1 damage probability model of Poreteus and Seitel will be extended in order to show the effects of laser angular and pulse energy fluctuations in *S*-*on*-1 mode. Four scenarios for *S*-*on*-1 measurement are discussed.

### 2.3.1. Reproducible repetitive laser radiation

In the case of absolutely stable repetitive laser radiation the area $a$ where fluence exceeds $T_{defect}$ (2.2.2) does not increase with consecutive laser pulses (Fig. 2.3.1.1, A). All repetitive pulses are at exactly the same physical position of the sample. Both initial 1-*on*-1 *best case* and the cumulative *S*-*on*-1 *worst case* damage probabilities are identical to the probability predicted by *Porteus* and *Seitel*.

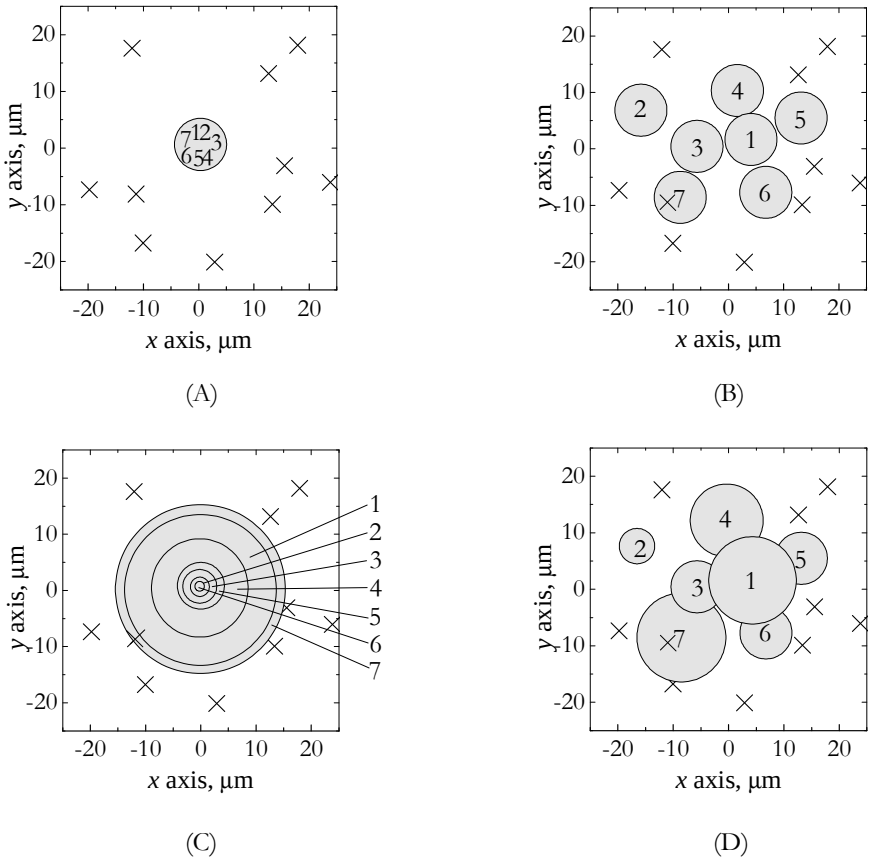


Fig. 2.3.1.1. Illustration of tested area: region where energy density is higher that $T_{defect}$ is depicted by filled circles. A – absolutely stable and reproducible stable beam, B - spatially fluctuating Gaussian beam: in this case, the seventh laser shot hits the defect and damages the test site, C – pulse-to-pulse energy fluctuations, D – spatially and energetically unstable laser pulses.

## 2.3.2. Spatial random beam hopping with no energy fluctuations

The term *jitter* will be used in order to describe either spatial random beam hopping on the target or pulse-to-pulse energy fluctuations of laser pulses. In this chapter the spatial jitter is modeled as a two-axis random process, whereby two axes of motion ($x$ and $y$ perpendicular to optical axis $z$) are uncorrelated and follow Gaussian normal statistics with the mean - zero and constant standard deviation $\sigma_s$. For pulses as short as 1 ns and shorter the single shot intensity is Gaussian in spatial domain but it shifts between pulses because of the jitter. Two-dimensional spatial jitter of peak energy density locations may be expressed as a normal distribution [73]:

$$R(x,y)=\frac{1}{2\pi\sigma_s^2}\exp\left\{-\frac{\left(x^2+y^2\right)}{2\sigma_s^2}\right\} \tag{2.3.2.1}$$

where $x$ and $y$ are the random coordinates of peak intensity position and

$$\sigma_s=\sqrt{\frac{\sum_{i=1}^{n}\left(x_i-\bar{x}\right)^2}{n-1}}=\sqrt{\frac{\sum_{i=1}^{n}\left(y_i-\bar{y}\right)^2}{n-1}} \tag{2.3.2.2}$$

one-axis standard deviation of the spatial jitter. According to empirical rule in the case of normal distribution, virtually all (approximately 99.73%) the data values can be expected to lie within a three standard deviation interval around the mean: $[\bar{x}-3\sigma_s;\bar{x}+3\sigma_s]$. Consider the radius vector which originates from the most probable peak intensity position of the beam in target plane. This vector every time is directed towards the peak intensity position of new exposition by laser shot. Following the empirical rule we suggest that maximal radius vector of spatial fluctuation has raw boundary of $r_{fl}=\sqrt{x^2+y^2}=3\sigma_s$. Accordingly, the $3\sigma_s$ can be a good parameter characterizing the approximate boundaries of spatial random beam hopping (spatial jitter). Note that parameter $r_{fl}$ may also have the meaning of either mechanical vibrations of the target or effects of air turbulence. Now consider the overlap of randomly walking beam and randomly distributed surface defects in (Fig. 2.3.1.1, B). According to the single shot model (2.2.4) damage probability is proportional to scanned area and defect density. The same principle can be applied here: random beam walking increases scanned area for which the local fluence is $T_{defect}$ or higher. Then cumulative (*S-on*-1) damage probability as a function of incident number of pulses $N$ can be derived from (2.2.4) simply replacing area $a$ in (2.2.5) by sum of newly added areas $\sum_{i=1}^{N_i}a_i$ . Here $a_i$ is only the fraction of newly interrogated are $a$ defined in (2.2.2) which does not overlap with previously scanned area. Index $i$ means the actual number of the pulse in burst and changes from 1 to $N_{\max}$:

$$P\left(N_i, M, I_0, \omega, T_{defect}\right) = \begin{cases} 0, & I_0 < T_{defect} \\ 1 - \exp\left( - \sum_{i=1}^{N_i} a_i\left(I_0, \omega, T_{defect}\right) \cdot M \right), & I_0 \geq T_{defect} \end{cases} \quad (2.3.2.3)$$

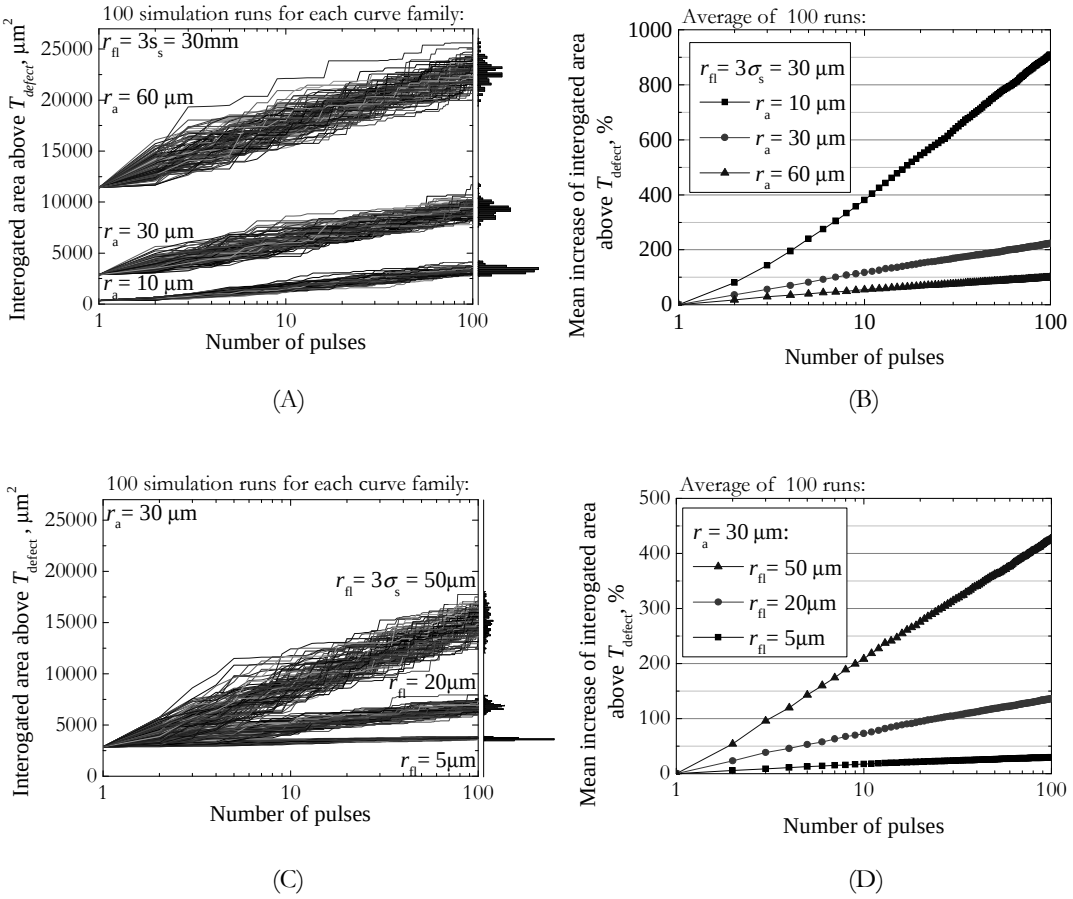


Fig. 2.3.2.1. Monte Carlo simulation of the increasing scanned area $A$ as a function of incident pulses. A – area in absolute units (spatial jitter is fixed); B – mean increase of interrogated area normalized to area of first shot (spatial jitter is fixed); C – area in absolute units (beam diameter is fixed); D – mean increase of interrogated area normalized to area of first shot (beam diameter is fixed)

A *Monte Carlo* simulation of randomly increasing area $A = \sum_{i=1}^{N_i} a_i$ due to spatial random beam hopping of the normal distribution is given in (Fig. 2.3.2.1). ISO 11254-2 [13] calls for increasing fluence levels. As fluence increases, the relative size of the jitter to laser spot diameter decreases. Therefore, the interrogated area normalized to initial area $a$ in (Fig. 2.3.2.1, B) increases much faster while coming closer, but remaining above the defect threshold. When the initial area is fixed and jitter is changed the total interrogated area increases faster for a larger jitter (Fig. 2.3.2.1, C and D). According to empirical rule the spatial

jitter has asymptotic radial amplitude of $r_{fl} = 3\sigma_s$. Accordingly, the total interrogated area $A$ for a sufficiently large number of shots can roughly be expressed as

$$A\left(r_{fl}, I_0, w, T_{defect}\right) = \pi\left[r_{fl} + r_a\left(I_0, w, T_{defect}\right)\right]^2. \qquad (2.3.2.4)$$

Graphical illustration of area $A$ is given in the (Fig. 2.3.2.2).

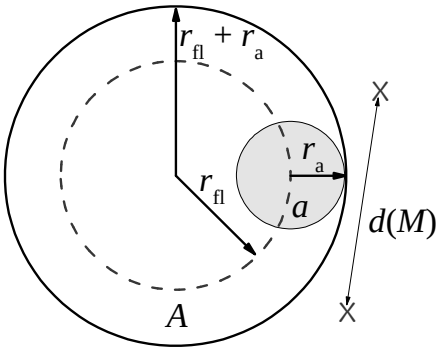


Fig. 2.3.2.2. Explanation of important radii areas and distance. See text below for details.

Therefore, the *worst case S-on-*1 damage probability for multiple pulses only because of the influence of spatial jitter can be expressed as:

$$P = \begin{cases} 0, & I_0 < T_{defect} \\ 1 - \exp\left(-\pi \cdot M\left[r_{fl} + r_a\left(I_0, w, T_{defect}\right)\right]^2\right), & I_0 \geq T_{defect} \end{cases} \qquad (2.3.2.5)$$

This curve will be discussed later together with the results of *Monte Carlo* simulation. Spatial pseudo-accumulation can be a significant factor when $r_a\left(I_0, w, T_{defect}\right)$ is small or similar compared to inter-defect spacing $d$ and the translation caused by maximal beam jitter $r_{fl}$. On the first shot, the area above the threshold will likely miss the defect. On the second shot (or subsequent shots), since the jitter is relatively large, uninterrogated region is likely to be exposed, which may contain a defect. In this case, if there is a defect in the second area and part damages, it appears as accumulation in *S-on-*1 measurement although it clearly is not.

## 2.3.3. No spatial random hopping, energy fluctuations

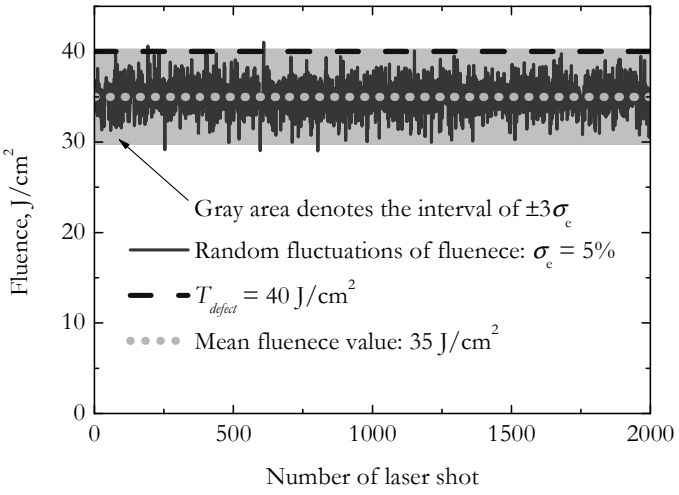


Fig. 2.3.3.1. Illustration of critical fluence and laser pulse-to-pulse energy fluctuations.

Considering there is no spatial jitter, but the pulse-to-pulse fluence is fluctuating (Fig. 2.3.1.1, C). Similarly like in the spatial domain pulse-to-pulse energy jitter can also be characterized in terms of normal (Gaussian) distribution:

$$E(I_0) = \frac{1}{\sqrt{2\pi}\sigma_e} \exp\left\{ -\frac{(I_0 - \bar{I}_0)^2}{2\sigma_e^2} \right\} \tag{2.3.3.1}$$

where $\sigma_e$ is standard deviation of peak fluence. The computer simulated noise of normal distribution is shown in (Fig. 2.3.3.1). As it can be seen, the fluence of individual shots can reach damage threshold of defects even at lower mean $\bar{I}_0$ fluence values. Following empirical rule the fluence of individual pulses can be roughly up to ~$3\sigma_e$ higher than average fluence $\bar{I}_0$. Then in *S-on-1* case the asymptotic *worst case* damage probability is approximately by $3\sigma_e$ lower than 1-*on*-1 damage probability:

$$P = \begin{cases} 0, & I_0 + 3\sigma_e < T_{defect} \\ 1 - \exp\left(-\pi \cdot M \cdot r_a\left(I_0 + 3\sigma_e, w, T_{defect}\right)^2\right), & I_0 + 3\sigma_e \geq T_{defect} \end{cases} \tag{2.3.3.2}$$

### 2.3.4. Spatial and energy fluctuations

Following the logical sequence of the cases described above the asymptotic *S-on-1* damage probability can be derived for more general case (Fig. 2.3.1.1, D). When random spatial beam hopping and energy fluctuations are present the *S-on-1* damage probability can be expressed as:

$$P = \begin{cases} 0, & I_0 + 3\sigma_e < T_{defect} \\ 1 - \exp\left(-\pi \cdot M\left[r_{fl} + r_a\left(I_0 + 3\sigma_e, w, T_{defect}\right)\right]^2\right), & I_0 + 3\sigma_e \geq T_{defect} \end{cases} \quad (2.3.4.1)$$

All four asymptotic cases are verified below by means of by *Monte Carlo* simulations of *S-on-1* measurement.

## 2.4. Computer simulations of *S-on-1* measurement

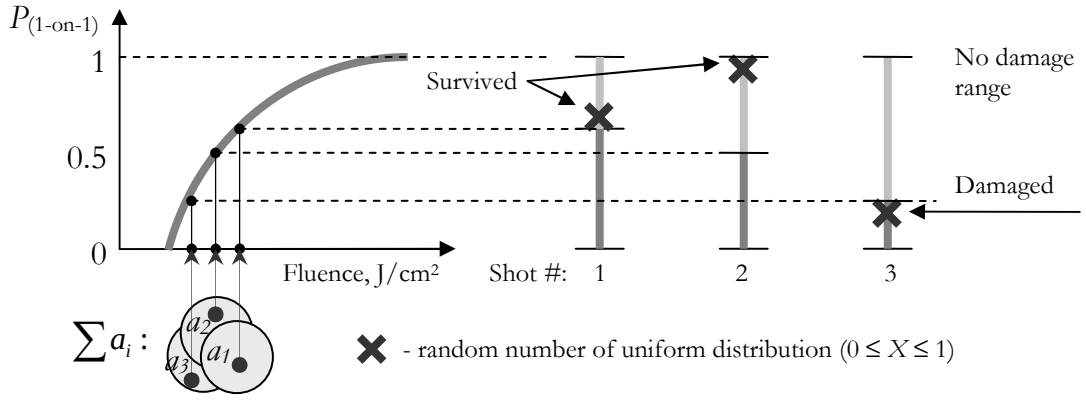


Fig. 2.4.1. The model of *S-on-1* measurement.

In order to perform a comparison between theoretical assumptions and experimentally obtained data, *Monte Carlo* simulation program of *S-on-1* measurement was developed. Simulations are based on the random damage/no-damage event generation using known single shot damage probability. Maximal number of laser pulses and their energy density are simulated according to real ISO measurement. The spatial random pulse-to-pulse hopping and fluence instabilities are considered as described by normal distributions. Damage probability for the first laser shot is given by the *Porteus* and *Seitel* formula (2.2.6).

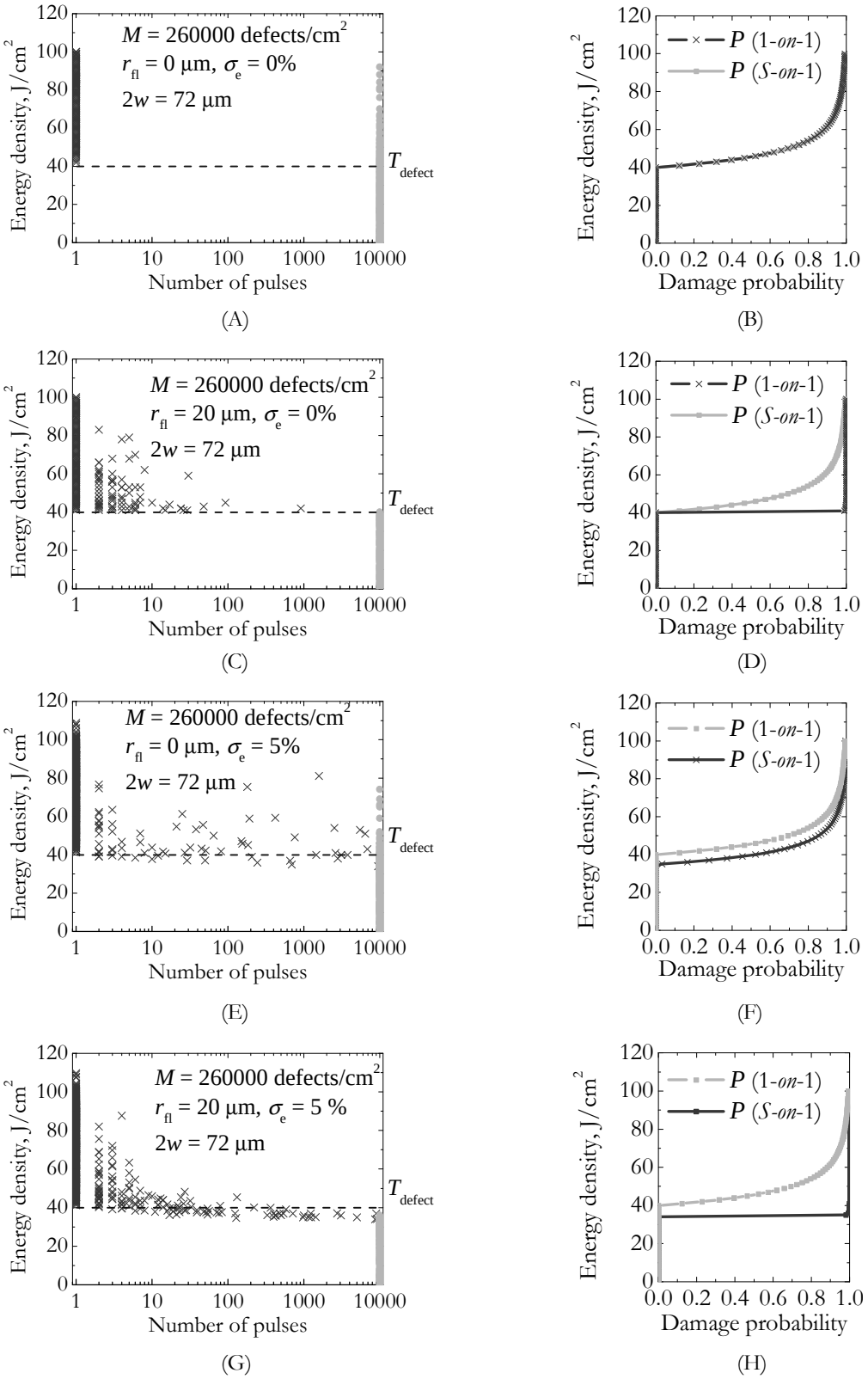


Fig. 2.4.2. On the left: Monte Carlo simulations of *S-on*-1 LIDT measurement with Gaussian beam diameter of $2w = 72$ μm and surface defect density 260000 defects/cm². On the right: single shot damage probability versus asymptotic *worst case* damage probability of *S-on*-1 measurement.

In order to simulate *damage/no-damage* event for each laser shot consider generation of a random numbers $X$ following the uniform distribution. This number must lie in the interval of $0 \le X \le 1$. After random number $X$ is generated it is checked whether this number is greater than probability obtained from *Porteus* and *Seitel* formula. If $X$ lies within interval $0 \le X \le P$, damage occurs after the first pulse. If the random number is outside this interval, the sample is not damaged (Fig. 2.4.1). Then new (shifted by jitter) physical position of laser shot is simulated and the increase of interrogated area is estimated. The probability of damage is then defined by the same formula (2.2.4) but area $a$ (2.2.2) is then replaced by the fraction of newly scanned area above $T_{defect}$ which appears due to the jitter. In the case of jitter new random number $X$ is generated for the second laser shot. For the further pulses of the burst the procedure is then repeated until first damage or maximal number $N_{\max}$ of pulses is reached. In general, the result of pseudo accumulation behavior varies with respect to the parameters of radiation and defect density of the sample. However, *S-on-1* simulations are performed only for specific set of parameters which are close to experimentally realized conditions. The aforementioned four jitter cases are simulated. *S-on-1* procedure [13] is simulated according to ISO 11254-2 standard. 10 virtual sites (different positions) on the sample are tested with $N_{\max}$ = 10000 pulses per selected energy density level. Then energy density is changed and another 10 virtual sites on the sample are tested with maximal amount of pulses. (Fig. 2.4.2) shows results of four model runs. Left side panels show the simulation of damage probability for all four jitter combinations. The right side panels correspond to the *best* and the *worst case* damage probabilities due to statistical accumulation. Crosses correspond to damage events in (Fig. 2.4.2). Filled circles are *non-damaged* sites after $N_{\max}$ is reached.

Numerical run of *S-on-1* measurement in the case of absolutely stable beam ($r_{\text{fl}} = 0$, $\sigma_{\text{e}} = 0\%$) corresponds to (Fig. 2.4.2, A and B). The damage occurs on shot #1 if there is a defect in the laser foot print. If there is no defect - the illuminated part survives the first shot and every subsequent shot, since there is

no heat accumulation or new defects. For the next pulses no new area is interrogated and, therefore, the probability of additional damage is equal to zero. In fact, test site is damaged after the first pulse or not damaged at all in the case of stable laser radiation.

There is a new area being interrogated after each pulse if there is finite spatial jitter $r_{fl} > 0$, $\sigma_e = 0\%$. If there is a defect in the laser foot print of newly interrogated area, the damage occurs. This situation corresponds to (Fig. 2.4.2, C and D). As it can be seen from asymptotic damage probability in (Fig. 2.4.2, D), the damage threshold does not change, but the cumulative damage probability increases close to the threshold. Spatial pseudo-accumulation effect can be expected to be a considerable factor when distance $r_{fl}$ is higher or similar to $d(M)$ and both of them are higher than $r_a$. The range where $r_a < d(M)$ and $r_a < r_{fl}$ depends on peak intensity $I_0$, beam diameter $w$, spatial jitter $\sigma_s$ and defect density $M$. As a rule, the spatial pseudo accumulation is always significant slightly above the damage threshold (Fig. 2.4.2, D). Depending on laser pointing stability and focusing optics the parameter $r_{fl} = 3\sigma_s$ in the vast majority of commercial laser systems is expected to be in the range of about 1 to 100 microns. In presence of spatial jitter the probability of damage grows until saturation point of interrogated area is reached. If the scanned area is fully saturated, the damage probability for next pulses is zero. Consider the situation when $I_0$ is near but above defect threshold and $r_a << r_{fl}$. Then in multi-shot irradiation mode area $A$ converges to $\pi r_{fl}^2$ and can be many times higher than the area $a$ above $T_{defects}$. When spatial jitter is large enough and newly interrogated areas do not overlap ($r_a << r_{fl}$) the experiment corresponds to a sequence of independent Bernoulli trials. Therefore, statistics of damage in that special case would follow $P(1\text{-}P)^{N-1}$ law [54, 74] until the areas $a$ don't overlap. Furthermore, if new defects and heat accumulation exists, there is no general expression for all cases of statistical damage distribution. However, a modified formula is derived in (2.3.4.1). It can be applied to evaluate the role of energy or spatial pulse-to-pulse instabilities as well as the mechanical vibrations.

The next case is when no spatial fluctuations of the beam exist but there is an energy fluence jitter $r_{fl} = 0$, $\sigma_e > 0\%$ (Fig. 2.4.2, E and F). In contrast to the previous case the damage threshold decreases approximately by $3\sigma_e$ for large number of pulses. This appears due to the fact that average fluence is used to characterize the typical pulse of the burst. The average value is lower than maximal deviation by approximately $3\sigma_e$. This is a rough estimate as for a very large number of pulses the individual values of pulse peak fluence can exceed the limit of $3\sigma_e$. However, the whole process is statistical in nature and even if damage probability is not equal to zero the damage may not occur especially when the damage probability is very close to zero (low defect density or small beam diameter). The situation is different only when defect density $M$ is very high and average distance between two defects is $d(M) < r_a$.

When both spatial ant fluency fluctuations are present $r_{fl} > 0$, $\sigma_e > 0\%$ the probability of damage for large number of pulses increases close to the threshold (Fig. 2.4.2, G and H). Moreover, virtually measured damage threshold is lower than $\sim 3\sigma_e$. This is a very important message for interpretation of experimental data.

## 2.5. Experimental evidence of pseudo-accumulation

In order to qualitatively verify our assumptions based on statistical accumulation model *S-on-1* LIDT measurement using instable laser radiation for antireflective coated LBO crystal was performed. The LIDT test system is described in the chapter 1.2.2 and the *S-on-1* procedure is defined in the reference [13]. The frequency tripled radiation of diode pumped and Q-switched Nd:YAG laser was used for the LIDT measurements. The main laser parameters are 0.5 kHz pulse repetition frequency, $\lambda$ = 355 nm wavelength, $\tau$ = 25 ns pulse duration (FWHM) and beam diameter of $2w = 72$ μm. The spatial jitter and beam diameter ($1/e^2$) of the Gaussian beam were characterized using 14 bit CCD detector (*WinCamD, Dataray*) in the focal plane of the focusing lens of the LIDT test system. The focal length of lens was of 0.6 m. The distance of free propagation between laser and

lens was of about 3 m. The measured single axis standard deviation of peak fluence position was about $\sigma_s \approx 4{,}2\ \mu m$ (Fig. 2.5.1). Vendor defined maximal angular pointing stability was of $\pm 50\ \mu rad$. The standard deviation of pulse-to-pulse energy stability was measured using (*Nova II, Ophir*) energy meter: $\sigma_e = 5\ \%$.

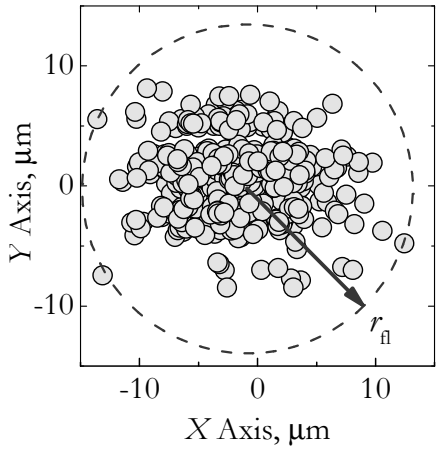


Fig. 2.5.1. Spatial Gaussian beam peak intensity pulse-to-pulse fluctuations of frequency tripled (Q-Switched, diode pumped) Nd:YAG laser recorded in focal plane of 0.6 m lens using CCD array.

The detection of damage during measurement was based on optical scatting technique. In the case of damage, surface starts to scatter the light and radiation is blocked. After the measurement all exposed sites were inspected using *Nomarski* microscope. The experimental data points of LIDT measurement are shown in (Fig. 2.5.2). It is evident that measurement data are rather chaotic and qualitatively similar to those obtained by simulations in (Fig. 2.4.2, C, E and G). In the situation of the true heat accumulation or defect incubation data are rather deterministic [75]: experimental points are distributed close to each other on a clear and narrow exponent-like curve. Such behavior is typical in femtosecond range of pulse durations. However, in our case, due to the jitter and high scattering of measured values it can be assumed that some of the accumulation is caused by pseudo-accumulation. At lower pulse repetition rates (at least below 1 kHz) the surface must return to the room temperature before the next laser pulse [76]. Furthermore, the observed damage morphologies near the

damage threshold in (Fig. 2.5.3) suggest that optical resistance of the sample is limited by the absorbing inclusions. Separated damage sites clearly show their spatial distribution. If each damage could be associated with a separate defect, $M$ could be roughly estimated to be about 260000 defects/cm$^2$ with average distance $d$ = 19.6 μm. This distance was used in our numerical simulations. The similarity of experimentally and numerically obtained data suggests that spatial and energy fluctuations (jitter) of separate laser pulses may play a role in the LIDT measurement.

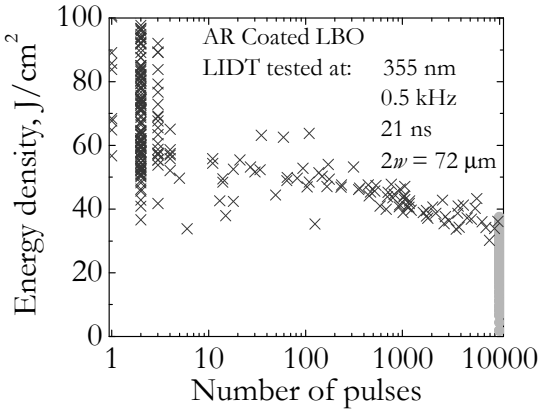


Fig. 2.5.2. The set of *S-on*-1 LIDT measurement data for dielectric coating: experimental data points are presumably modulated by pseudo-accumulation.

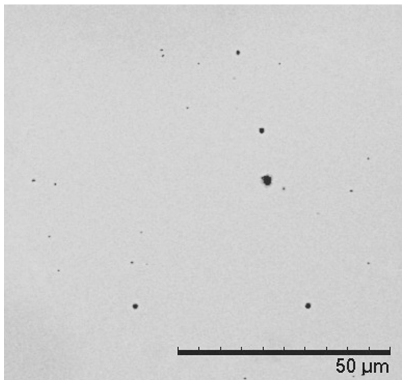


Fig. 2.5.3. SEM image of laser induced damage morphology of dielectric coating energy density level exceeding the LIDT by few percent.

## 2.6. Conclusions

Model of the pseudo-accumulation effect is introduced for optical surfaces containing absorbing defects and numerical *Monte Carlo* simulations are performed for *S-on*-1 measurement. Modeling results show that pulse-to-pulse fluctuations in laser beam propagation direction and pulse energy or even mechanical vibrations in the optical system produce apparently accumulative damage statistics. The exposed area increases shot-by-shot, thus increasing the *S-on*-1 damage probability. Therefore, there is a risk of underestimating LIDT for high $N$ by fitting experimental data modulated by pseudo-accumulation. This information is useful for estimation of real damage probability. Results from this model are consistent with experimental observations. The proposed model of pseudo-accumulation effect is important for studying accumulation processes. Scaling the results is an issue in small spot *S-on*-1 test to a larger spot size.

# 3. Influence of the multiphoton absorption on the optical resistance in dielectric laser coatings

*Material related to this chapter was published in* [A4, A18] *and* [C8, C25]

Optical resistance in laser components is a function of many irradiation parameters such as laser pulse duration [11, 37, 67, 77-81], spot size [82], wavelength [83], irradiation manner [84] and material parameters of the sample [78]. It was discovered that fatigue laser damage exists due to the heat accumulation [85] and defect incubation [86] effects: an additional irradiation of the same sample site influences the damage threshold of the material. Responsible for optical damage mechanisms are not the same at different laser pulse durations. It is widely regarded that incident pulses, lasting longer than a few tens of picoseconds, damage dielectrics by heating conduction-band electrons and transferring their energy to the lattice. This damage mechanism predicts a $\sqrt{\tau}$ dependence of the 1-*on*-1 threshold damage fluence upon pulse duration $\tau$ [37, 77]. For ultrashort pulses (shorter than few tens of femtoseconds) scaling law of LIDT upon pulse duration $\tau$ is still under investigation. Almost all studies have yielded a significant deviation from $\sqrt{\tau}$ scaling for pulse durations $\tau$<10 ps. A decrease [80, 81] and even an opposite [87] dependencies of the critical energy fluence versus pulse duration were reported. However, the shortcomings of previous studies in femtosecond range were partially addressed by the low wavelength resolution of damage probability measurements. In most of the cases measurements were performed for the fundamental radiation and its second and third harmonics. Different ionization mechanisms are influencing the ionization process, thus such wavelength resolution is insufficient to draw the conclusions about the main mechanism of damage. In this chapter we consider, for the first time to our knowledge, the LIDT measurement of $TiO_2$ single layer dielectric coatings in femtosecond range by a continuously changing wavelength. Such resolution is sufficient to resolve the abrupt change in multiphoton absorption. In addition, we show the same effect in multilayer dielectric coatings. The

experimental results are supported by theoretical considerations and results of numerical simulations. This work is motivated by growing importance of the femtosecond laser optics in industrial applications and few works in this field.

## 3.1. Short overview of LIDT mechanisms in fs range

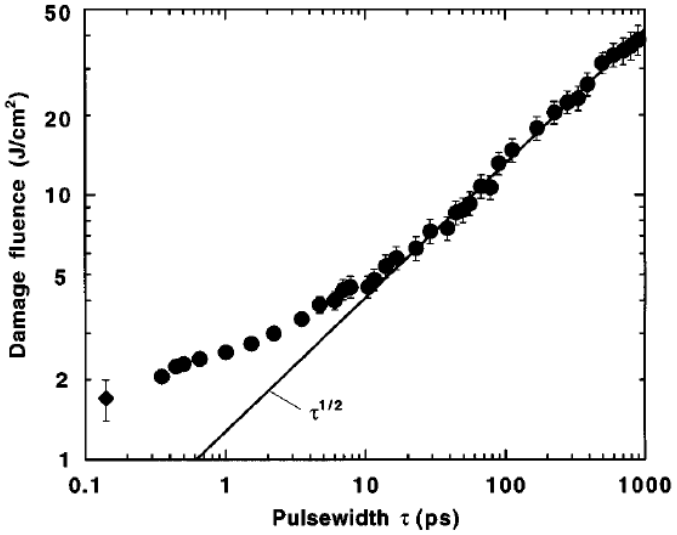


Fig. 3.1.1 Pulse width dependence of threshold damage fluence for fused silica at 1053 nm (●) and 825 nm (◆) [81].

Every laser pulse contains a certain amount of energy, stored in the field of electromagnetic wave. During the laser-matter interaction (in UV - NIR) a part of this energy is transferred to electronic system of wide band-gap material and then to the lattice. Storage of this energy in the material due to electron-phonon interaction is referred to as *heat accumulation*. The amount of transferred energy is dependant on interaction time (pulse duration $\tau_p$), absorption and reflection coefficients. There is a generally accepted picture of laser damage in dielectrics for near infrared (NIR) wavelengths and long pulses. For laser pulse durations $\tau_p$ longer than ~10 ps generation of free electrons starts due to linear absorption because of inclusion states. After that electrons are accelerated in conduction band without significant electron-avalanche [88] and their energy is converted to heat of lattice. Limited thermal diffusion leads to a square-root pulse duration dependence (Fig. 3.1.1) of damage threshold [89]:

$$LIDT \propto \sqrt{\tau} \quad [\mathrm{J/cm^2}] \tag{3.1.1}$$

Damage fluence for pulses shorter than ~10 ps does not follow the square root law any longer and exhibits morphology dramatically different from that observed at long pulses [79]. Nonlinear processes become more and more dominant as the laser pulse duration decreases. Initially quasi-free electrons are provided by multi-photon, tunnel or linear absorption, through structural defect states in the band-gap or by direct interband transitions (Fig. 3.1.2). Excited electrons are heated by the remaining part of the ultra-short laser pulse. Due to electron inverse *bremsstrahlung* absorption and impact electron collisions, processes lead to electron avalanche [87, 90, 91]. This is followed by photoelectron emission, surface charging and thermalization (carrier-carrier scattering). Thermalization of quasi-free electrons proceeds on a material-dependent timescale. The energy transfer to lattice by electron-phonon coupling (carrier-phonon scattering) follows afterwards with subsequent heating of irradiated site [92]. Then ultrafast melting and pressure wave is generated [93] which is followed by a thermal diffusion resulting in time-dependent lens effect for laser focal region [94]. Typical time scale of the above mentioned phenomena is depicted in the (Fig. 3.1.3). In conclusion, conduction band electrons gain energy from the laser field much faster than they transfer energy to the lattice which has important consequences for the damage threshold for ultrashort laser pulses. The actual damage occurs after pulse has passed and electron energy finally is coupled into the lattice. Due to this fact the deviation from thermal single pulse LIDT is observed for ultrashort pulses [11, 78, 79]. Moreover, relation between LIDT, $\tau_p$ and material band-gap was introduced by M. Mero et. al. [78]:

$$LIDT\left(E_g, \tau_p\right) = \left(c_1 + c_2 E_g\right)\tau_p^k \quad [\mathrm{J/cm^2}] \tag{3.1.2}$$

with $c_1 = -0.16 \pm 0.02$ $\mathrm{J \cdot cm^{-2} \cdot fs^{-k}}$, $c_1 = 0.074 \pm 0.004$ $\mathrm{J \cdot cm^{-2} \cdot fs^{-k} eV^{-1}}$, and $k = 0.30 \pm 0.03$ being material and pulse duration independent parameters. One has to be very careful when comparing the experimental damage threshold levels from different studies because a lot of groups use different conventions of beam diameter and intensity, and the experimental conditions are not the same.

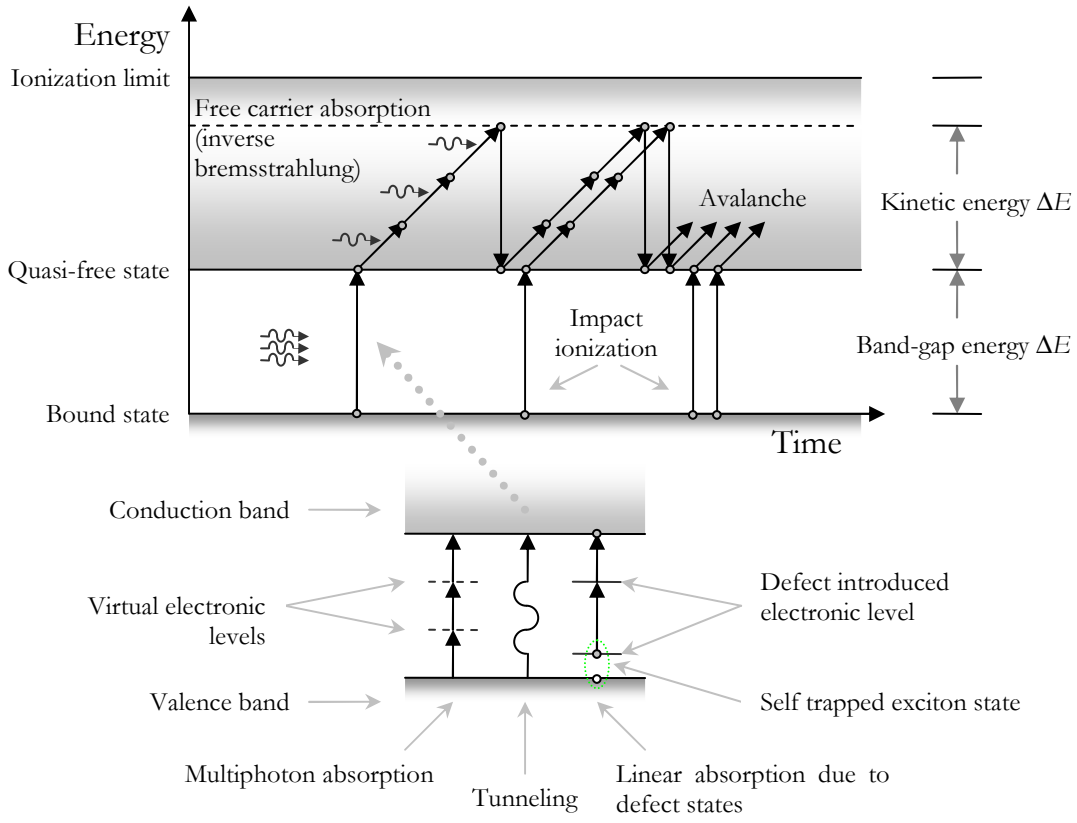


Fig. 3.1.2. Interplay of multiphoton, tunneling, linear absorption, impact and avalanche ionization in the process of plasma formation. Avalanche ionization consists of a series of multiple inverse bremsstrahlung absorption events followed by impact ionization [91].

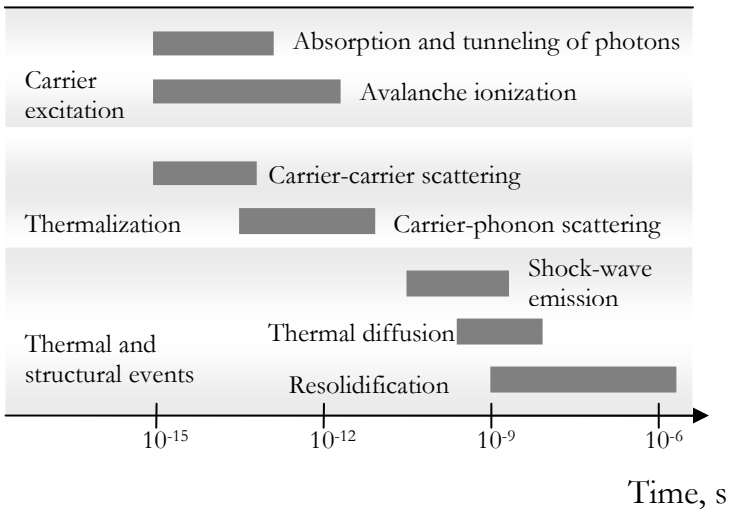


Fig. 3.1.3. Schematic diagram of physical phenomena associated with the interaction of a femtosecond laser pulse with the transparent materials. The solid bars represent the typical timescales for the relevant processes [95].

### 3.1.1. The rate equation of free electron dynamics

Laser-induced damage in wide band-gap optical materials is a result of material modifications arising from the interaction of laser accelerated high energy electrons and the lattice. Material absorbs the energy from the laser pulse and a region of high free electron density in conduction band is produced. The damage occurs when the critical electron density of ~$10^{19}$ – $10^{21}$ $cm^{-3}$ is reached [90]. Dynamics of local free electron density in the conduction band is roughly described by following simplified rate equation [11, 96, 97]:

$$\frac{\partial \rho}{\partial t} = W_{Pi}(I(t)) + W_{Av}(I(t), \rho(t)) - W_r(\rho, t) \qquad (3.1.1.1)$$

where $\rho$ is the local electron density in the laser footprint, $W_{Pi}$ is photo ionization rate due to the multiphoton absorption of tunneling effect, $W_{Av}$ is the increase of electrons due to the avalanche and $W_r$ electron relaxation rate.

#### 3.1.1.1. Keldysh photo ionization formula

The first term $W_{Pi}$ on the right in (3.1.1.1.) is predicted by L.V. Keldysh [98] and describes both tunneling and multiphoton ionization. In fact this is the rate ionization for atoms or solid bodies in the field of a strong electromagnetic wave. Photo ionization rate (3.1.1.1.1) is valid when energy of laser photons is much smaller than the band-gap of material [97]:

$$W_{Pi}(I(t)) = \frac{2\omega_0}{9\pi}\left(\frac{\omega_0 m}{\hbar\sqrt{\Gamma}}\right)^{3/2} Q(\gamma, x)\exp\left(-\pi\frac{K\left(\sqrt{\Gamma}\right)-E\left(\sqrt{\Gamma}\right)}{E\left(\sqrt{\xi}\right)}\right)]x+1[; \qquad (3.1.1.1.1.)$$

where:

$$Q(\gamma, x) = \sqrt{\frac{\pi}{2K\left(\sqrt{\xi}\right)}}\sum_{n=0}^{\infty}\left\{\exp\left(-n\pi\frac{K\left(\sqrt{\Gamma}\right)-E\left(\sqrt{\Gamma}\right)}{E\left(\sqrt{\xi}\right)}\right)\Phi\left(\sqrt{\eta(n+2\mu)}\right)\right\},$$

$$\gamma = \frac{\omega_0}{e}\sqrt{\frac{mU_i c\varepsilon_0 n_0}{2I}}, \qquad \Gamma = \frac{\gamma^2}{\gamma^2+1}, \qquad \xi = \frac{1}{\gamma^2+1},$$

$$x = \frac{2U_i}{\pi\hbar\omega_0\sqrt{\Gamma}}E\left(\sqrt{\xi}\right), \qquad \mu = ]x+1[-x, \qquad \eta = \frac{\pi^2}{2K(\xi)E(\xi)},$$

$$\Phi = \int_0^z \exp\left(y^2 - z^2\right)dy, \quad K(k) = \int_0^{\pi/2} \frac{1}{\sqrt{1-k^2\sin^2(\varphi)}}d\varphi, \quad E(k) = \int_0^{\pi/2}\sqrt{1-k^2\sin^2(\varphi)}d\varphi.$$

Here $\gamma$ is adiabatic *Keldysh parameter*, $\omega_0$- central frequency of laser irradiation, $e$- electron charge, $m$– effective mass of the electron, $U_i$- energy band-gap of the material, c-speed of light in vacuum, $\varepsilon_0$-permittivity, $n_0$-refractive index, and $I$- local intensity of laser irradiation, $\hbar$ -Planck constant, $]Z[$-integer part of $Z$, $\Phi$- Dawson integral and $K$, $E$ –elliptic integrals of the first and the second type. The boundary between multiphoton ionization and tunneling ionization is defined by the *Keldysh parameter* $\gamma$. For $\gamma$ < 1,5, ionization rate describes a tunneling process [99, 100]. In the case of strong electric field, the *Coulomb well* is suppressed. The bound electron tunnels through the barrier and becomes *free*, as it is shown schematically on the left-hand panel of (Fig. 3.1.1.1.1). The phenomenon of tunneling has no counterpart in classical physics and is an important consequence of quantum theory. This type of nonlinear ionization dominates for strong laser fields and low laser frequency [90]. Furthermore, the studies of tunneling ionization showed the dependence of ionization rate at given intensity on both the ionization potential charge energetic state.

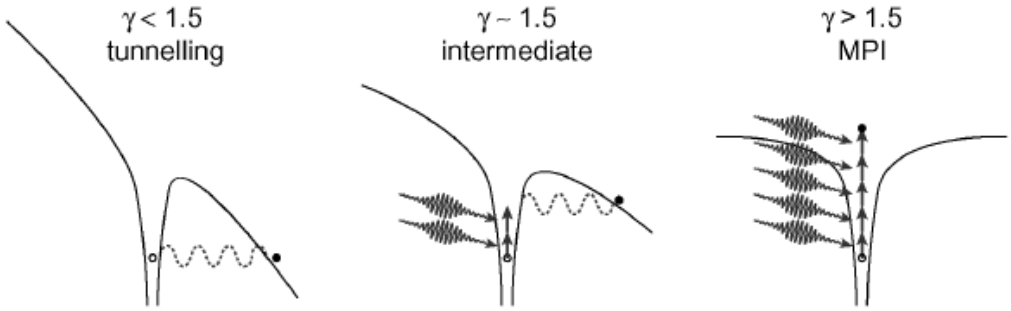


Fig. 3.1.1.1.1. Schematic diagram of photoionization phenomena. In a solid, the electron is promoted from the valence to the conduction band, rather than ionized [90].

For $\gamma > 1{,}5$, the *Keldysh* formula (3.1.1.1.) describes the multiphoton ionization [80] unbinding the electrons from the quantum well as it is shown in the right-hand panel of (Fig. 3.1.1.1.1). In 1929, Maria Göppert-Mayer predicted that theoretically an atom might absorb two or more photons simultaneously, thus allowing electron transition from state to state which is out of reach to the separate photons. Electron must absorb enough photons for being promoted from valence to conduction band. The total absorbed energy is equal or greater than the band-gap of the material [90]. The rate of multiphoton absorption can be expressed as $\sigma_{mp} I^N$. Here, $I$ is laser intensity and $\sigma_{mp}$ is cross section of $N$-photon absorption [48]. The number of photons required is determined by the smallest $N$ that satisfies the relation, $N\hbar\omega_0 > U_i$, where $U_i$ is the band-gap energy of the dielectric material and $\hbar\omega_0$ is the photon energy.

### 3.1.1.2. Impact ionization and electron avalanche

Term $W_{Av}$ in the formula (3.1.1.1.) corresponds to the electron avalanche [11, 48, 97] by impact ionization:

$$W_{Av}(I(t), \rho(t)) = \eta \rho I \; ; \tag{3.1.1.2.1}$$

where $\eta = \dfrac{\sigma}{\varepsilon_{crit}}$, $\sigma = \dfrac{e^2}{c\varepsilon_0 n_0 m} \dfrac{\tau_c}{1+\omega^2\tau_c^2}$, $\tau_c = \dfrac{16\pi\varepsilon_0^2 \sqrt{m\left(\dfrac{U_i}{10}\right)^3}}{\sqrt{2}e^4\rho}$.

Hereby, electrons in the conduction band gain energy from photons due to inverse *bremsstrahlung* absorption (Fig. 3.1.1.2.1., on the left). Additional electron will be promoted from the valence band to the conduction band, if the electron gained energy is higher than band-gap energy. Stuart et al. [11] developed a model of avalanche ionization in which the avalanche rate depends linearly on laser intensity. Heating of electrons in the conduction band is taken into account using what is basically a *Drude model*, considering the electron energy dependence of the conductivity included [48, 90]. This model makes the flux doubling approximation, stating that an electron in the conduction impact ionizes an

electron from the valence band as soon as it has enough energy to do so. However, avalanche ionization process requires some *seed* electrons in the conduction band. These initial electrons are provided either by thermally excited carriers, by easily ionized impurity or defect states, or by carriers that are directly excited by multiphoton or tunneling ionization. Typically, the initial electron density of ~$10^{19}$ $cm^{-3}$ is critical to start the significant effect of the avalanche ionization process. Nevertheless, the influence of avalanche ionization is of fundamental importance for quantitative analysis of ionization process.

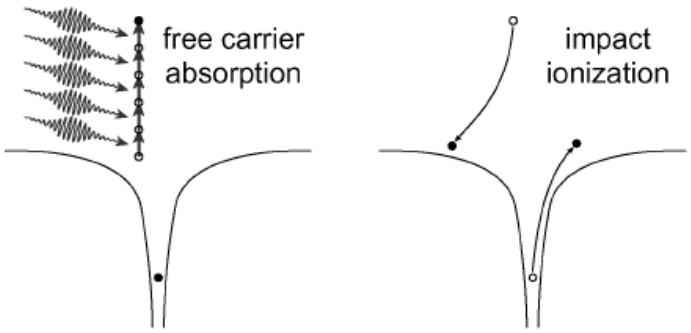


Fig. 3.1.1.2.1. The mechanism of impact ionization. Initially free electron absorbs photons through inverse *bremsstrahlung* absorption (on the left) and when the gained energy reaches double bandgap energy the second electron is promoted to the conduction band by the impact collision (on the right) [90].

### 3.1.1.3. The relaxation of carriers

The last term $W_{rel}$ in the equation (3.1.1.1.) corresponds to the relaxation process:

$$W_{rel} = \frac{\rho}{\tau_{rel}}. \qquad (3.1.1.3.1.)$$

The conduction band electrons can relax to the valence band or decay into shallow traps [101] as well as into self trapped excitons (STE) [48, 90]. STEs are well-known lattice defects observed in many wide-gap dielectric materials. Shallow traps are typical for coatings and manifest themselves as small tails in the transmission spectrum near the band-gap observed in our oxide films. However, in this study we do not distinguish between different origins of relaxation. However, the effective time relaxation is roughly considered to be $\tau_{rel} \approx 500$ fs.

### 3.1.2. Fatigue laser damage due to the heat accumulation and defect incubation

The *S-on-1* threshold for multiple-shot irradiation is almost always lower than for single-shot experiments by a factor of two to four when using femtosecond laser pulses [102, 103]. In fact, the surface damage threshold drops dramatically after the first laser shots until reaching an almost constant level. When the sample is damaged after more than one laser pulse, this is the so-called *fatigue* laser damage [104, 105]. To our knowledge there are two main reasons for fatigue laser damage in femtosecond range of pulse durations. The additional irradiation of the same test site causes either defect incubation (pulse-to-pulse absorption, and mechanical stress increase [101]) or heat accumulation (shot-by-shot temperature increase [106]). The fatigue laser damage probability can be measured according to ISO standard by *S-on-1* procedure. The damage threshold (zero level damage probability) as a function of incident number of pulses is referred to as *characteristic damage curve*. When the material is irradiated with the train of repetitive laser pulses a source of heat at the focal volume is created. The electron system is heated at first and then the energy is transferred to the lattice. The temperature of the lattice grows when the pulse-repetition rate is high enough (Fig. 3.1.2.1.) and the time interval between incident laser pulses is less than required for heat diffusion of absorbed laser energy [76, 85, 100, 107-109]. The typical heat diffusion time is of the order of ~1 μs [76]. The longer the material is exposed to the train of pulses, the higher the temperature at the focus and the larger the region that is heated. The energy is accumulated around the focal volume until the melting point is reached or the local structural changes occur. The boiling, evaporation or ablation takes place if the temperature is further increased. Therefore, the repetition rate, number of incident pulses and beam diameter are critical to the damage threshold. The radius of the so-called heat affected zone (HAZ) is controllable by an increase in either repetition rate or the incident laser fluence. If the laser beam waist is located in the bulk of the sample, the waveguides due to refractive index

changes may be produced [110]. Due to limited diffusion time LIDT also depends on the beam radius $\omega_0$ [108, 111, 112].

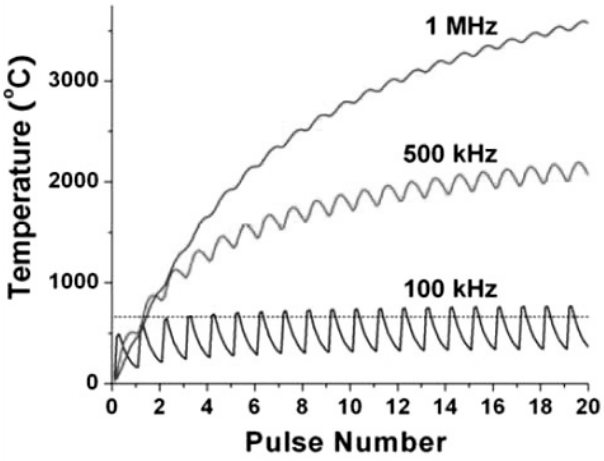


Fig. 3.1.2.1. Temporal evolution of glass temperature with respect to the number of laser pulses at a radial position of 2 μm from the center of the laser beam [107].

Up to now amplified femtosecond pulses from Ti:Sapphire based laser systems are typically separated by milliseconds, exceeding significant time required for heat to diffuse out of the focal volume [76]. The focal volume thus returns to room temperature before the next pulse. Consequently, the structural change caused by an amplified laser is confined to the focal volume, regardless of the number of pulses that strike sample [101]. Defect generation by intense laser radiation is the second very important mechanism leading to fatigue laser damage [89]. Strong optical excitation is sufficient to generate electrons and holes: the process of defect formation starts from exciton creation, followed by self-trapping. In fact, the generation of lattice defects causes the increased absorption for every pulse of the burst. STE's add more energy levels inside the forbidden band-gap, in analog to the effect of impurities and introduces excitation routes for the next laser shots [102]. Moreover, defects increase the mechanical stress inside the material which is directly related to the optical resistance [105]. As a result of intense femtosecond laser irradiation, micron sized defect clusters may form, which can yield macroscopic structural damage in the material. In addition, significant transient volume associated with exciton self-trapping increases. This creates a shockwave-like perturbation that eventually damages otherwise perfect lattice. Defect formation may be classified as extrinsic or intrinsic depending on whether

the defect is derived from the precursor. Recent advances [48] in the study of self-trapped exciton (STE) structures and time-resolved pump probe measurements [47] have provided the basis for a new level of understanding of the mechanisms of intrinsic defect formation. Excitonic mechanisms of defect formation are well established in laser-irradiated halides, $SiO_2$, $TiO_2$, $Ta_2O_5$, and $HfO_2$, among many other wide band-gap materials with strong electron-lattice couplings. These STEs are long-lived and can accumulate during illumination by a sequence of pulses.

## 3.2. Modeling of critical electron density

Ionization rates (3.1.1.1.) are calculated for the given experimental conditions in order to model LIDTs of experimentally prepared $TiO_2$ samples. According to literature, the electron density of $10^{21}$ $cm^{-3}$ is considered critical. Refractive index of $TiO_2$ coatings $n_0$ = 2.48 was determined experimentally from reflection – transmission measurements. Different mechanisms are responsible for the electron density growth in conduction band (3.1.1.1.1.). Therefore, the nonlinear material response is expected to be as a function of the radiation parameters. For instance, an abrupt change of the electron density growth due to the multiphoton absorption is expected for the wavelength transition from $n$ to the $n$+1 - photons which are necessary to promote the electron from valence to conduction band.

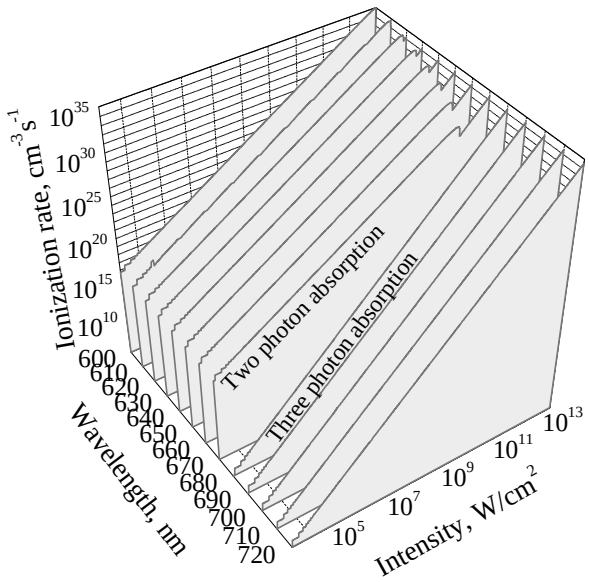


Fig. 3.2.1. The estimation of *Keldysh* ionization rates $W_{Pi}$ for $TiO_2$ at different wavelengths [113].

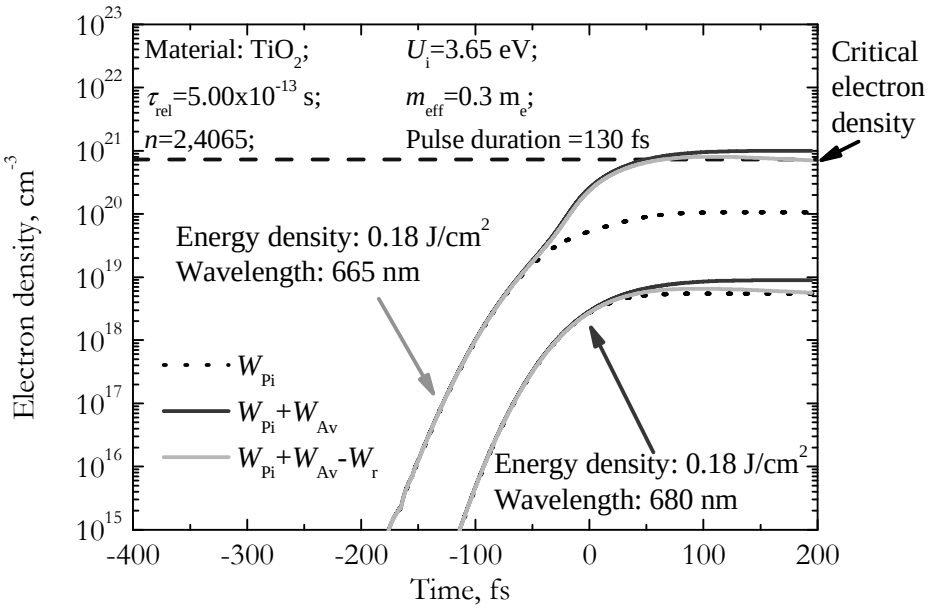


Fig. 3.2.2 Electron density in $TiO_2$ during a fs-pulse [113].

In contrast to multiphoton case, a continuous change in ionization rate is expected for the tunneling mode. The *Keldysh* ionization rate in $TiO_2$ was determined numerically (3.1.1.1.1.) for the wavelengths of interest (Fig. 3.2.1). Temporal profile of the pulse intensity is considered to be Gaussian. And indeed at lower intensities (up to ~$10^{11}$ W/cm$^2$) there is an abrupt change in ionization rate that corresponds to the multiphoton absorption.

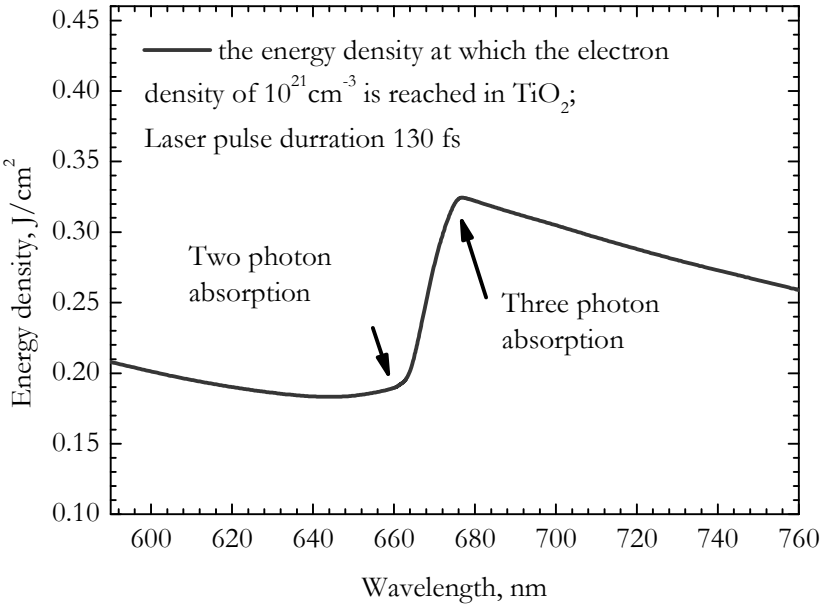


Fig. 3.2.3. The computer simulation of laser intensity which is necessary to produce the critical ($10^{21}$ cm$^{-3}$) electron density [113].

At very high intensities the *Keldysh parameter* $\gamma < 1{,}5$ corresponds to the tunneling ionization mode ant there is no abrupt change in ionization rate with respect to the wavelength. Since the Gaussian temporal profile is considered, ionization rate thus corresponds rather to the multiphoton mode at the beginning and the end of the pulse and to the tunnel mode at the peak intensity. Of course, this assumption is not valid for all materials and wavelengths since the ionization rate depends on many parameters. Modeled dynamics of electron density under identical laser pulses but different wavelengths are calculated for $TiO_2$ (Fig. 3.2.2). The influence of different mechanisms is displayed by separate curves. As we can see, density of free electrons is not the same for different wavelengths. This implies the idea of different LIDTs for different wavelengths. In order to verify this assumption the laser pulse fluence at which the maximal electron density of $10^{21}$ $cm^{-3}$ is reached for 130 fs pulses at the wavelength of interest is modeled (Fig. 3.2.3). As it was predicted, in order to reach the same electron density the different intensities are necessary when changing the wavelength. Moreover, there is an abrupt change in the critical energy density. The predicted model needs to be verified experimentally. The approach of verification is measurement of LIDTs in $TiO_2$ coated layers using tunable wavelength source.

## 3.3. Preparation of samples

Experiments were conducted on two types of samples: the first set of samples consisted of single-layer $TiO_2$ films and the second set HR stack $TiO_2/SiO_2$ mirrors. The first set of $TiO_2$ single layer samples[2] was coated on the B270 glass substrates using ion-beam sputtering (IBS) technique, which is known to produce films with nearly bulk-like refractive indices and low optical losses. Films were nearly amorphous and had a physical thickness of 440 nm. The material band-gap energy ($U_{i(TiO2)} = 3.65$ eV) and refractive index of the coatings ($n_{TiO2} = 2.48$) were determined from spectrometric measurements. With respect to band-gap energy

[2] ~5% of $SiO_2$ were mixed into $TiO_2$ during the IBS process. Since $SiO_2$ has broader band-gap than pure $TiO_2$ the band-gap of the experimental coatings were slightly broader that of pure $TiO_2$.

the *stepwise transition* form the 2 to the 3 photon absorption is expected at a wavelength of ~680 nm (Fig. 2.3.1). Separate mirrors of identical spectral formula must be prepared for each wavelength in order to avoid the effects of interference and standing waves of electric field in the coating. Therefore, the high reflectivity (HR) dielectric coatings centered at $\lambda$ = 800 nm and 400 nm were deposited on BK7 substrates using IAD technique. The high refractive index $TiO_2$ and the low refractive index $SiO_2$ materials were chosen for production of dielectric mirrors. All coatings were designed using commercial software (*TFCalc, Software Spectra Inc.*). Spectral formula of alternating quarter-wave optical thickness layers was in both cases the same – $(HL)^8H2L$, where L = $SiO_2$ and H = $TiO_2$. Coatings satisfy condition of $R > 98\ \%$ at $\lambda =$ 800 nm and 400 nm specification. The overcoats of 2L were used in both cases of HR coatings in order to shift the standing wave maximum towards the higher damage threshold layer of $SiO_2$. Such overcoat helps to increase LIDT by ~50-100% [114]. The IAD coating process started by evacuating the coating chamber to $2 \cdot 10^{-3}$ Pa pressure and heating substrates up to 170 °C. Preconditioning of the evaporation materials and pre-cleaning the substrates for 10 minutes using ion source with $O_2$ was made. Afterwards the gas flow was introduced in the chamber, resulting in ~$2 \cdot 10^{-2}$ Pa total pressure during the deposition. Deposition rates were 0.13 nm/s for $TiO_2$ layers and 0.22 nm/s for $SiO_2$ layers. $O_2$ gas was used for feeding the ion gun for hardening coatings by ion assistance. Anode current was of ~2.5 A. Physical thicknesses of trial coatings were 2167 nm and 1022 nm for HR 800 nm and HR 400 nm mirrors respectively.

## 3.4. Results and discussions

The measurement of breakdown threshold fluence as a function of wavelength was performed on both - single $TiO_2$ layers and $TiO_2/SiO_2$ coating stacks. The femtosecond Ti:Sapphire oscillator-amplifier system, operating at a wavelength of 800 nm with a spatially Gaussian beam profile and the pulse duration of 130 fs, was used for the measurements. Pulse repetition rate was 1 kHz. *Topas 4-800*

optical parametric amplifier was attached to the system in order to convert laser energy to the wavelength of interest. For more experimental details refer to the chapter 1.2.2. The first set of samples was illuminated with a burst of 1000 pulses at center wavelengths from 590 nm to 750 nm. The technique used to measure damage threshold fluence was based on the measurement of *S-on*-1 damage probability as a function of incident pulse energy. Extrapolation of data to a zero-damage probability was made to obtain the threshold fluence corresponding to the center of the Gaussian beam. As expected, the LIDT's of 0% damage probability in the investigated range exhibit a quantized transition at approximately 680 nm (Fig. 3.4.1). In the range from 590 nm to 670 nm of two photon absorption LIDT remains almost constant at a level close to 0.1 J/cm$^2$. Between 670 and 690 nm, the threshold increases dramatically. The threshold reaches a constant level again at about 0.40 J/cm$^2$ in 3 photon absorption range. This change in the threshold exceeds approximately ~20% uncertainty of measurement. The *step* from two to three photon absorption matches theoretical consideration.

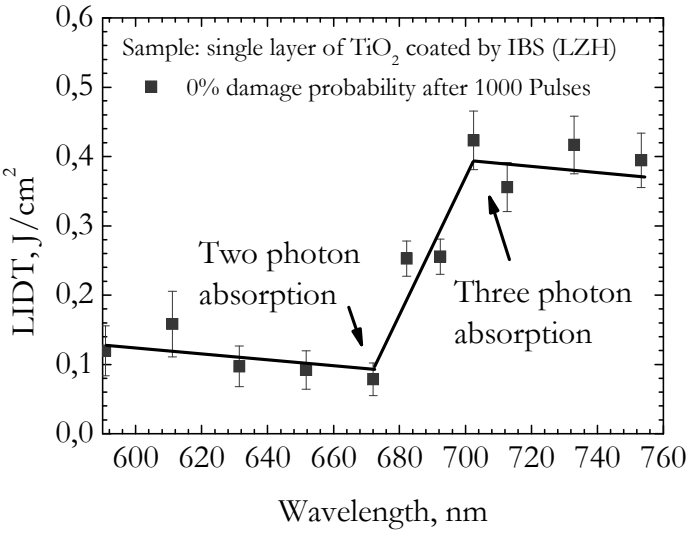


Fig. 3.4.1. The result of *S-on*-1 LIDT measurement[3] for single layer $TiO_2$.

[3] obtained in the international team of LZH and VULTC groups during the LASERLAB-EUROPE project in Vilnius

The second set of samples - $TiO_2/SiO_2$ mirrors - was tested in a similar way. Samples were illuminated with a burst of 10000 pulses at fixed center wavelengths: mirror *HR400nm* – at 400 nm and *HR800nm* at 800 nm, respectively. Damage morphologies of samples were observed by microscope (*Ergolux, Leiz*). The result of measurement is shown in (Fig. 3.4.2).

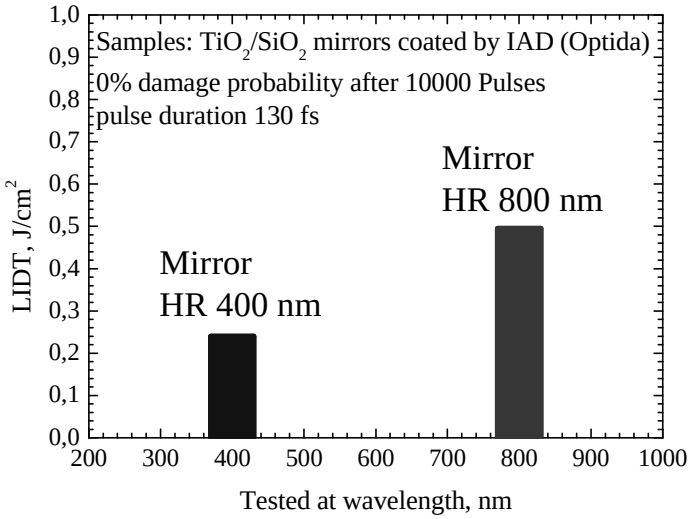


Fig. 3.4.2. The result of *S-on*-1 LIDT measurement for $TiO_2/SiO_2$ mirrors.

In principle, data of both experiments confirmed theoretical considerations: the step-like transition of LIDT is observed experimentally by changing the wavelength in single layer $TiO_2$ coatings. Moreover, the same effect was observed in the case of HR coatings. Since both mirrors were additionally coated by $SiO_2$ overcoat which reduces the internal electric field intensity in $TiO_2$ layer the damage threshold observed for the mirrors is higher than in the case of single layer coatings. However, band-gap of the material is much smaller for $TiO_2$ layers than for $SiO_2$ and this layer limits the optical resistance [78]. LIDT at different wavelengths corresponds to different absorption cross-sections of two and three photon absorption. The same result was predicted by theoretical model of critical density electron generation. Similar results were achieved independently for KDP crystals by Carr et al [83]. The main difference between measurement and modeling of our work is the fact that modeling was made for single shot measurement (1-*on*-1) but the experiment was performed in multi-shot (*S*-*on*-1) operation. *S*-*on*-1 instead of 1-*on*-1 measurement was performed because of two

main reasons. The speed of mechanical shutter was insufficient to ensure accurate control of the exposure by the single laser pulse at repetition rates of 1 kHz. Sometimes one, sometimes as many as two pulses pass through the aperture of the mechanical shutter until it is fully open. Also, the *S-on-1* measurement is more important from practical point of view since it corresponds to real operation conditions of optical coatings. In all cases the incubation effect was observed. For all samples LIDT reached constant level after approximately 10-100 pulses and decreased by approximately 50% compared to first pulses. As it was shown my M. Mero et al [101], the thermal accumulation does not play a role here at 1 kHz repetition rates. The most likely fatigue mechanism of LIDT in femtosecond range is caused by incubation of self trapped excitonic states inside band-gap of $TiO_2$. Such excitons are the result of high electron density in conduction band. Lifetime of the states is high enough if compared to the time between pulses set by the repetition rate of the laser [48, 90, 101]. Material starts to absorb strongly and the electron avalanche starts at the moment when the density of exited electrons reaches critical level. This process leads to ablation and permanent structure changes. It is obvious that 1-*on*-1 damage threshold which is directly proportional to multiphoton absorption of the first pulse is also critical for fatigue laser damage.

## 3.5. Conclusions

The experimental observations of $TiO_2$ coatings showed the stepwise transition in LIDT when continuously tuning the wavelength of laser pulses (130 fs and 1 kHz) in spectral range from 590 nm to 750 nm where two-photon absorption changes to three-photon absorption. It confirms that multiphoton absorption is one of the main damage mechanisms in femtosecond range. Both multilayer and single layer dielectric coatings exhibit similar LIDT behavior.

# 4. LIDT of multilayer dielectric coatings in femtosecond range: role of substrate roughness and coating densification by accelerated ions

*Material related to this chapter was published in* [A3] *and* [C7].

A more complete understanding of different factors that can influence laser-induced damage threshold is necessary for further optimization of optical resistance in multilayer dielectric coatings. These factors include coating deposition methods, deposition process parameters and the choice of coating materials [28, 43, 115, 116]. It was also discovered that the substrate surface properties such as crystalline structure and roughness [117] may also influence the crystal structure of the growing coating. Experimental results show that even slightly different deposition conditions can result in differ LIDT's. Up to now[4] the most common deposition techniques for metal-oxide films remains e-beam and IAD evaporation. However, the mobility of arriving particles with low thermal energy is not large enough to make dense films in e-beam process. In the case of such evaporation thin films consist of columns and voids [43]. Such irregular structures and porosity can introduce additional absorbing defects i.e. self trapped excitons [46] into the lattice. Moreover, the low density and columnar microstructure evokes more undesirable optical effects, such as vacuum-to-air spectral shift, anisotropy and high scattering losses. In order to solve the spectral stability problems related to columnar growth and porosity, more energetic forms of film deposition techniques such as IAD, IBS and MS were developed [24, 33, 34]. The mobility of coating atoms can be enhanced indirectly by substrate heating and by ion bombardment of the growing coating or by sputtering targets and directly producing atoms with higher energy. On the other hand, densification of coatings leads to *replication* of irregular substrate surface in the growing coating [37]. This replication produces the cone-like pits or lens-like defects. Because of these defects the local intensity of incident light may be

[4] more detailed overview is given in the chapter "Coating deposition techniques"

increased many times [38, 39, 118] thus lowering LIDT. To our knowledge the effect of substrate surface roughness as well as role of coating densification with more energetic ion beams is not investigated in detail for femtosecond laser pulses. Thus the aim of study described in this part is experimental investigations of influence of substrate roughness and coating densification by IAD method on the optical resistance of multilayer coatings. According to this, the following study was split in two parts: *roughness test* and *ion assisted densification test*.

The approach to *roughness test* involves the production of the identical e-beam multilayer coatings on well-characterized substrates from different vendors, having different root-mean-square surface roughness ($R_{rms}$). This test is important because of surface preparation, and because finishing quality (roughness) varies from vendor to vendor and it may play a role for damage resistance. The surface roughness of each sample is measured with an atomic force microscope (AFM). In order to examine this relationship between roughness and LIDT, all coatings were LIDT-tested and compared under identical test conditions using fs pulses. Multilayer coatings were deposited under the same e-beam evaporation conditions during the same process run.

The second test referred to as *ion assisted densification test* is based on the comparison of optical resistance of two HR coatings with almost identical spectral formula of coating layers and the same BK7 substrate surface roughness, but evaporated by different methods: e-beam and IAD respectively. Substrates as well as the deposited coatings were characterized by different techniques and finally LIDT-tested. For the densification of layers an additional ion gun was introduced into the coating plant (IAD technique). Typically, the kinetic energy is then supplied by a beam of ionized Ar or $O_2$ gas that is accelerated towards the growing film [23, 24, 26-32]. Momentum transfer at values of 10 to 300's eV discourages columnar growth, thus densifying the layers. Therefore, IAD films are harder, smoother and exhibit more stable optical properties than conventional e-beam films. However, the quality of IAD film is strongly influenced by the energy

of the incident ions and their density [26]. This method has been used extensively for more than two decades, but questions about the densification impact on the fs LIDT are still open. A few works mention such improvement [31], but, on other hand, there are works where the opposite trends are observed [32]. To clarify this we performed a series of *S-on*-1 tests for $10^4$ pulses at 1 kHz repetition rate and the wavelength of 800 nm. For coating structure characterization X-ray diffraction (XRD) measurements were performed.

## 4.1. Preparation of samples

High reflection (HR) multilayer dielectric coatings centered at $\lambda$ = 800 nm were deposited on 20 mm-diameter and 4 mm-thick BK7 substrates in a *VU-2M* coating plant[5]. Two evaporation techniques were applied, namely e-beam and ion assisted deposition (IAD). High refractive index $ZrO_2$ and low refractive index $SiO_2$ materials were chosen for the production of sample layers. Both coatings were designed using commercial optical thin film coating software *TFCalc*. The standard requirement for a laser-line dielectric mirror: $R$ > 99.5 % at $\lambda$ = 800 nm was set as a design target. Design of 27 alternating QWOT $ZrO_2$ and $SiO_2$ layer (substrate/$(HL)^{13}H$/air, total thickness: 4330 nm) for the e-beam case and design of 21 alternate quarter-wave thickness $ZrO_2$ and $SiO_2$ layers (substrate/$(HL)^{10}H$/air, total thickness: 3270 nm) for the IAD case were obtained to satisfy $R$ > 99.5 % at $\lambda$ = 800 nm specification. The e-beam HR coating process started by evacuating the coating chamber to $3 \cdot 10^{-3}$ Pa pressure and heating the substrates to 300° C. After preconditioning of evaporation materials and pre-cleaning of the substrates for 10 minutes by using the ion source with Ar gas, an additional $O_2$ gas flow was introduced into the chamber, resulting in ~ $4 \cdot 10^{-3}$ Pa total pressure during the deposition. The approximate deposition rates were 0.4 nm/s and 0.5 nm/s for $ZrO_2$ and $SiO_2$ layers respectively. IAD HR coating process was started in the similar way; however, all substrates were heated to 170° C. Argon gas was used for feeding ion beam gun. Oxygen gas was

[5] The same coating plant is described in previous chapter

introduced into the chamber resulting in total chamber pressure of ~ $2 \cdot 10^{-2}$ Pa during process. The main parameters of ion beam power supply were:

Cathode current $I_C$: ~15 A
Anode current $I_A$: ~ 2.5 – 3 A
Anode voltage $U_A$: ~150 V

The deposition rates during the IAD coating process were approximately 0.06 nm/s for $ZrO_2$ layers and 0.12 nm/s for $SiO_2$ layers. The layer thicknesses in both processes were controlled by measuring the transmittance of growing layers on the test glass pieces.

### 4.1.1. Characterization of surface roughness by AFM

Substrate surfaces were examined by means of contact-mode atomic force microscopy using the scanning probe microscope (*Explorer, Thermomicroscopes*). Scans in a range of 100 to 1 μm in five distinct surface points near the centre of specimen were performed collecting topography. The most common statistical parameters $R_a$ and $R_{rms}$ (the average roughness deviation and the root-mean-square roughness deviation respectively) were calculated from topography data using *SPMLab 5.01* software. The definitions for these parameters are given in (4.1.1.1) and (4.1.1.2):

$$R_a = \frac{1}{N} \sum_{i=1}^{N} \left| Z_i - \bar{Z} \right| \tag{4.1.1.1}$$

$$R_{rms} = \sqrt{\frac{1}{N} \sum_{i=1}^{N} \left\langle Z_i - \bar{Z} \right\rangle^2} \tag{4.1.1.2}$$

Areas with erroneous data, noise spikes and noise lines were excluded before calculations. Surface examination results are presented in (Fig. 4.1.1.1 and 4.1.1.2) (later compared in Table 4.2.1). Surfaces of four samples obtained from different

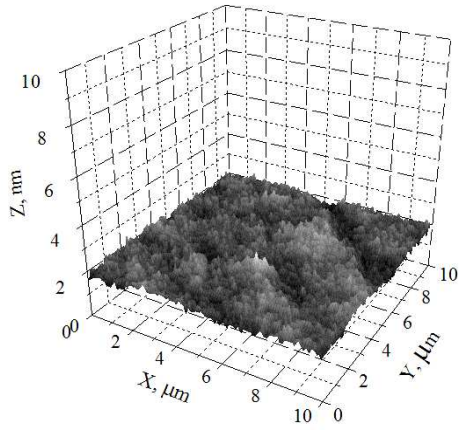


(A) Surface of sample A1

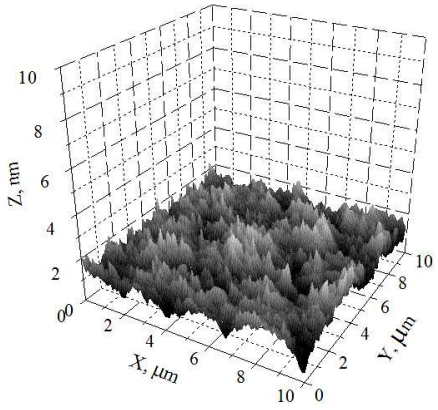


(B) Surface of sample B1

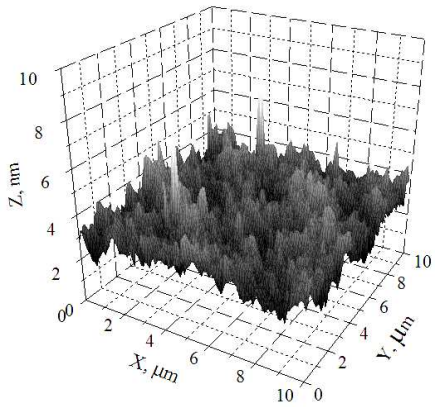


(C) Surface of sample C1

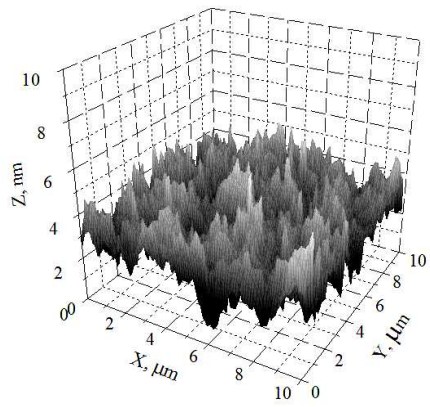


(D) Surface of sample D12

Fig. 4.1.1.1. Representative BK7 glass surfaces of substrates obtained from different vendors (before the deposition of HR layers).

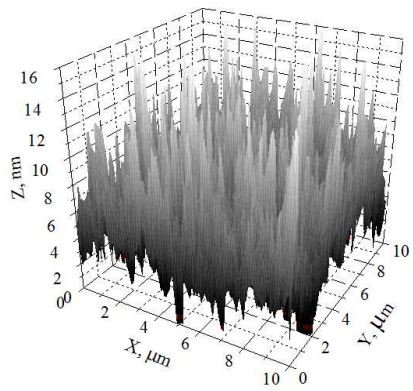


(A) Surface of the e-beam coating

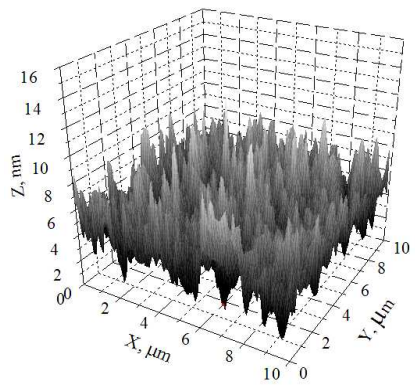


(B) Surface of the IAD coating

Fig. 4.1.1.2. Surfaces after the deposition of HR coatings.

vendors before deposition process show different topographies (Fig. 4.1.1.1). IAD and e-beam coated samples on substrates with the same surface roughness also differ in roughness (Fig. 4.1.1.2). Average roughness deviation $R_a$ and root-mean-square $R_{rms}$ roughness deviation were calculated for 10 $\mu m^2$ areas. As expected, the e-beam coatings are more porous and have higher surface roughness. Roughness of IAD coated samples is ~50% lower than for e-beam coatings. However, it exceeds the roughness of substrates. These results are in good agreement with the results obtained by [19]. The histogram of AFM height values per same scanned area is given in (Fig. 4.1.1.3).

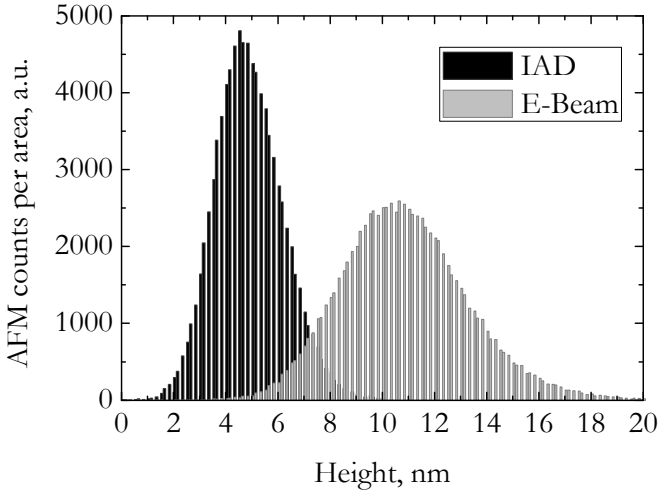


Fig. 4.1.1.3. The histogram of AFM height values for E-beam and IAD coating.

## 4.1.2. Characterization of refractive indices

The ratio of refractive indices of high $n_H$ and low refractive index $n_L$ materials in a quarter-wave-layer stack determines the spectral width and depth of dielectric mirror. Transmission measurements show that the spectral width of high reflection zone (192 nm at $T = 1\%$ level) of IAD HR coating exceeds the high reflection zone of e-beam HR coating (176 nm at $T = 1\%$ level). These results are in good agreement with calculated designs of these HR coatings. (Fig. 4.1.2.1) shows the difference in the refractive index of $ZrO_2$ resulting from different coating technologies – lower index for e-beam evaporation alone and higher index

for ion-assisted deposition. When $ZrO_2$ is evaporated using electron beam, low thermal energies of condensing atoms or molecules result in porous, low packing density and thus lower refraction index $ZrO_2$ layers. In the case of IAD, the growing film is bombarded with energetic ions. That increases the mobility of condensing atoms and molecules on the surface of the substrate. In this case good adhesion increased packing density and thus a higher refractive index $ZrO_2$ layer ensues. This result is in consistence with the surface roughness measurements and refractive indices obtained by [19].

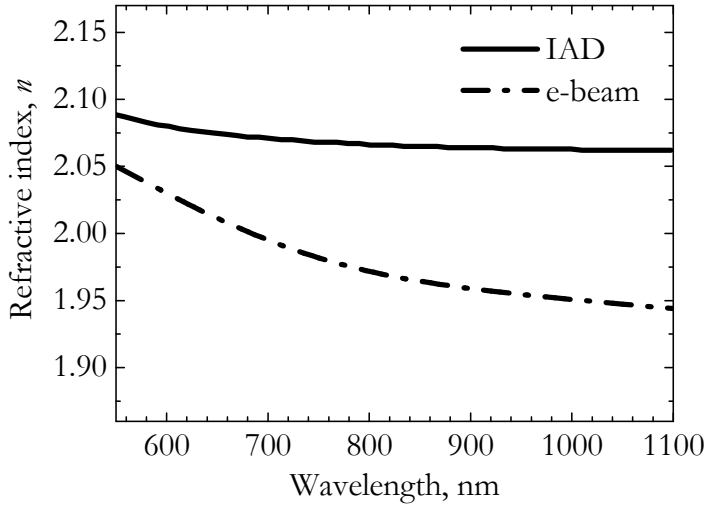


Fig. 4.1.2.1. Refractive index of $ZrO_2$ according coating method.

## 4.1.3. X-ray characterization of coatings

X-ray diffraction (XRD) measurements of the optical coatings were performed with a diffractometer (*D8, Bruker AXS*) equipped with a primary beam monochromator for Cu radiation. Peaks were step-scanned typically with a step-length of 0.02° and a counting time of 3.5 s per step. (Fig. 4.1.3.1) shows a typical XRD pattern for $SiO_2/ZrO_2$ e-beam and IAD optical coatings. Sharp peaks present on the pattern corresponded to $ZrO_2$ monoclinic and tetragonal phases [119, 120]. Silicon oxide layers were amorphous. The monoclinic phase of the $ZrO_2$ coating lattice structure dominates in coatings fabricated using IAD at 170 °C and tetragonal phase of $ZrO_2$ dominates for conventional electron-beam evaporation (e-beam at 300 °C) coatings.

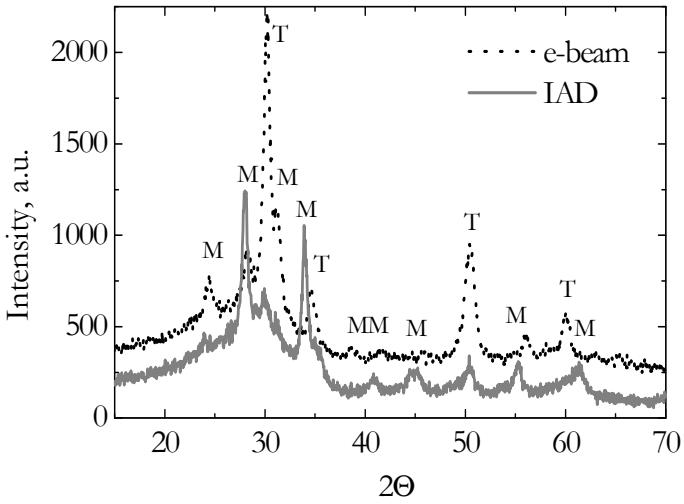


Fig. 4.1.3.1. XRD patterns of coatings deposited by using e-beam and IAD methods. T – $ZrO_2$ tetragonal, M - $ZrO_2$ monoclinic. Cu $K_2$ radiation was used.

## 4.2. Results and discussions

The main part of experimental results is presented in Table 4.2.1. A typical graph of experimental statistics and a characteristic damage curve for femtosecond pulses are shown in (Fig. 4.2.1). After the first 100 pulses the threshold for which the probability of damage becomes non-zero is constant. The characteristic damage curve only changes during the first 100 pulses.

Table 4.2.1. Experimental results

| Sample | Coating method | Experiment | Coatings layer materials | Substrate roughness, nm | | Laser beam diameter in target plane, μm | Wave-length, nm | Pulse duration, fs | $LIDT_{0\%}$ after 10000 shots, J/cm² |
|---|---|---|---|---|---|---|---|---|---|
| | | | | $R_a$ | $R_{rms}$ | | | | |
| A1 | e-beam | *roughness test* | $ZrO_2$ and $SiO_2$ | 0.12 | 0.16 | 535 | 800 | 130 | 0.351 |
| B1 | | | | 0.27 | 0.35 | 540 | | | 0.335 |
| C1 | | | | 0.39 | 0.50 | 535 | | | 0.355 |
| D12 | | *deposition* | | 0.51 | 0.64 | 540 | | | 0.332 |
| D2 | IAD | *method test* | | 0.51 | 0.64 | 560 | | | 0.343 |

As can be seen from the experimental results for 130-fs pulses at 800-nm wavelength, the surface roughness of the substrates had almost no influence on the LIDT. Although the roughness characterized by $R_{rms}$ was in the range of 0.16

– 0.64 nm, the variation in LIDT was not higher than ~7 %. This is close to accuracy of relative measurements, which was ±5 % in our experiments. The same can be said about deposition methods. The LIDT value for IAD optical coating deposited on substrate with the same polishing quality as e-beam coating was higher by ~3 %. Taking into account other samples, the LIDT of IAD coating is in the middle of the range of all observed values.

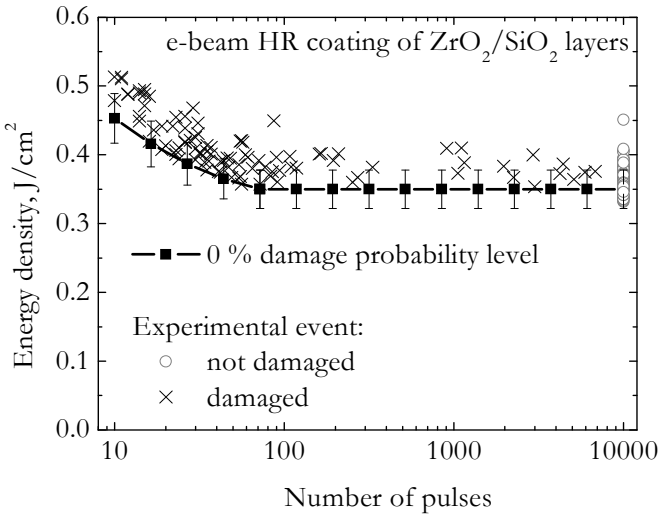


Fig.4.2.1. The typical characteristic damage curve: 0% damage probability of e-beam coated $SiO_2/ZrO_2$ HR mirror.

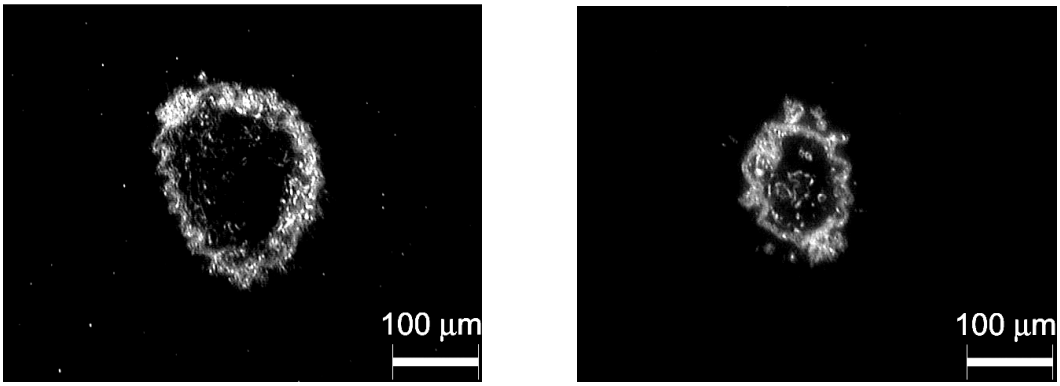


(A) (B)

Fig. 4.2.2. *Nomarski* images of laser-induced damage on HR coated BK7-glass specimens. A – femtosecond pulse induced damage on coating produced by e-beam technique, B – damage on coating produced by IAD technique

Coatings prepared by IAD have the same LIDT value for 130-fs pulses as coatings prepared by e-beam. The main mechanism of laser damage at this pulse duration near the threshold is assumed to be multiphoton absorption in the first layer with high refractive index and high absorption in UV. This can be seen from AFM analysis of laser damage. Damage depth does not reach BK7 substrate, and the substrate has nearly no influence on LIDT for femtosecond pulses directly or trough surface absorption that still exists at the film-substrate interface after coating. *Nomarski* micrographs of damage sites produced by femtosecond laser pulses at energy fluency levels near threshold are shown in (Fig. 4.2.2, A and B).

## 4.3. Conclusions

LIDT comparison of high-reflection coatings deposited of alternating quarter-wave optical thickness $ZrO_2/SiO_2$ layers by using IAD and e-beam techniques was performed at femtosecond laser pulse durations. Monoclinic and tetragonal crystalline phase of $ZrO_2$ layers dominated for IAD (at 170 °C) and e-beam (at 300 °C) deposition techniques respectively. Even though the crystalline phases in $ZrO_2$ layers were different both coatings had almost the same LIDT values for 130 fs, 800 nm and 1 kHz pulses in *S-on*-1 test mode. The IAD and e-beam HR coatings typically had higher than 2 nm surface roughness characterized by $R_{rms}$. Therefore, the typical 0.16 – 0.64 nm roughnesses of substrates had also almost no influence on LIDT of HR coatings for repetitive femtosecond pulses.

# 5. The influence of interference effects on optical resistance in multilayer dielectric coatings

*Material related to this chapter was published in* [A19] *and* [C15].

There are theoretical and experimental works dedicated to investigation of relation of laser induced damage and electric field intensity (EFI) within dielectric coating [63, 121-123]. Since interfaces of high and low index materials within a coating stack are usually identified as the weakest zone, there were many attempts to suppress electric field intensity by shifting its peaks to more resistant low refractive index material. Several studies also demonstrated that there is a clear correlation between damage morphologies and distribution of electric field within multilayer coatings [122, 124]. However, the vast majority of studies were performed for nanosecond laser pulses causing thermal damage. The aim of this work was an experimental study of femtosecond optical resistance in dielectric mirrors using standard alternating QWOT design and modified *e-field* design with suppressed electric field strength. This question arises naturally, since the mechanism of damage is different in femtosecond range [48, 78, 90]. The approach of investigations consists of production of the coatings and their optical resistance testing using ultrashort pulses. High refractive index materials $ZrO_2$, $HfO_2$ and $Ta_2O_5$ were chosen for two sets of experiments. Two different designs of the coatings were investigated: *standard* alternating quarter-wavelength layer design with $SiO_2$ overcoat, and modified *e-field* non quarter-wavelength design with suppressed electric field. Damage sites were studied using optical and AFM microscopes. Relation between electric field distribution and damage morphology was observed. Results demonstrate that suppressing electric field at layer interfaces enables to increase LIDT for high reflectance coatings almost twice compared to standard quarter-wavelength design when using ultrashort laser pulses. However, electric field distribution is sensitive to variations in thicknesses of outer layers, so deposition process should be precisely controlled to get improvement in LIDT of coatings.

## 5.1. Preparation of $ZrO_2/SiO_2$ samples

Experiments were carried out using *VU-2M* coating plant equipped with a high vacuum diffusion pump, backed by rotary oil and rotary lobe pumps. The coating chamber was 70 cm in diameter and 70 cm in height with a spherical rotational substrate holder. Two 180° electron-beam sources and a gridless *end-Hall* ion source for the substrate pre-cleaning and ion beam assisted deposition were installed in the chamber. Deposition process was controlled by optical monitoring measuring the transmission through test glass pieces at selected control wavelength. Optical monitoring was performed using a spectrophotometer with operating range from 250 nm to 1500 nm. The main design specifications of the ion beam source:

Ion energy: 80-120 eV

Beam current: 750 mA (anode current is 4 A)

Ion beam current density: 5 mA/cm² (central part at 150 mm distance)

Table 5.1.1. Main design and deposition parameters of experimental $ZrO_2/SiO_2$ mirrors

| Design | Number of layers | Thickness (nm) | Tempe-rature (°C) | $ZrO_2$ deposition rate (Å/s) | $SiO_2$ deposition rate (Å/s) | Back-ground gas | Deposition pressure (Pa) |
|---|---|---|---|---|---|---|---|
| *standard* | 26 | 3260 | 300 | 3.5 | 5 | $O_2$ | ~$4.5 \times 10^{-3}$ |
| *e-field* | 32 | 4260 | | | | | |

The main purpose of the first experiments was to compare the resistance of *standard* design high reflectance coating with *e-field* design, where intensities of electric field at the layer interfaces as well as in the high refractive index material were suppressed by modifying thicknesses of outer layers to shift peaks of standing electric field wave to the layers of low refractive index material ($SiO_2$). We chose to suppress the intensity of electric field about three times in *e-field* coating comparing to the maximum intensity at the interface of outer layers in standard quarter-wavelength design. The mirrors were designed using *TFCalc* software. The final *e-field* design modified thicknesses of the outer 8 pairs of the

stack and additional 3 pairs of $ZrO_2$ and $SiO_2$ layers to match reflectance at $\lambda$ = 800 nm of *standard* design mirror. Both designs had the overcoat of half-wavelength thickness $SiO_2$ layer. All coatings were deposited on BK7 substrates. The first pair of mirrors was manufactured using common e-beam evaporation of $ZrO_2$ and $SiO_2$. The main design and deposition parameters are presented in the Table 5.1.1, while calculated distribution of standing electric field wave at nine outer layer pairs of both mirrors is shown in (Fig. 5.1.1).

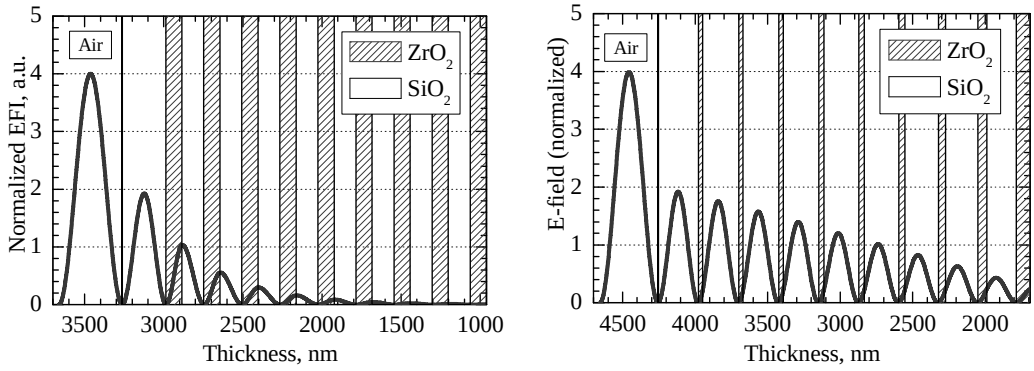


Fig. 5.1.1. Distribution of normalized electric field intensity at nine pairs of outer layers of standard (left) and *e-field* (right) $ZrO_2/SiO_2$ mirror designs.

Measured reflectance spectra of *e-field* design deposited mirrors by spectrophotometer (*Perkin Elmer, Lambda 950*) are presented in (Fig. 5.1.2). Due to errors during the deposition run, there were clear discrepancies between designed theoretical and measured spectral curves. We used optimization of optical layer thicknesses of initial *e-field* design to match the measured spectra and to recover the real structure of deposited layers in order to trace very possible pattern of *E-field*. During the *reverse engineering* procedure, the changes of optical thickness of each layer were restricted to 5%, in order to avoid non-realistic solutions. All this procedure was done using the same *TFCalc* software package.

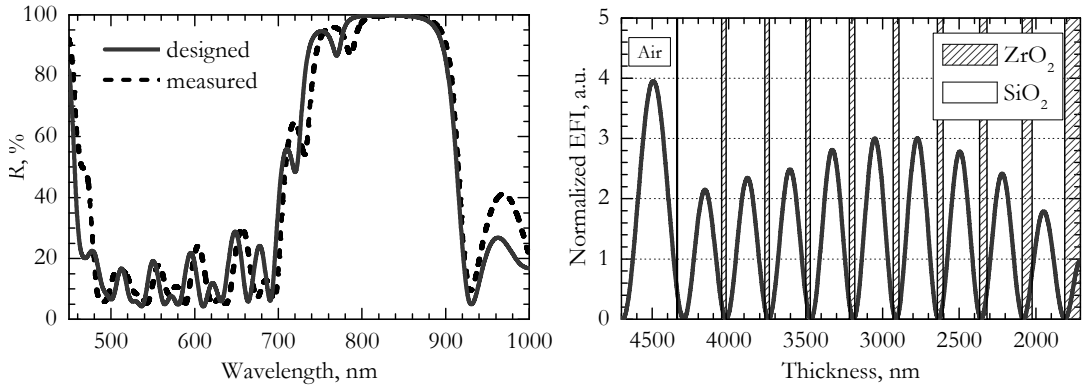


Fig. 5.1.2. Measured and designed spectra of experimental *e-field* $ZrO_2/SiO_2$ mirrors (left). Distribution of normalized electric field intensity in the nine pairs of outer layers of deposited *e-field* $ZrO_2/SiO_2$ mirror, corresponding to measured reflectance spectrum (right).

(Fig. 5.1.2). on the right shows distribution of electric field intensity in deposited *e-field* coating. Deposition errors clearly led to even worse result compared to *standard* design, because the real electric field intensity at all eight outer $SiO_2$ layers is approximately two times higher than designed. The field intensity in the 8th and 9th layer outer interfaces reached the same maximum electric field intensity as in the outer interface of layers of *standard* design. This *e-field* pattern could possibly lead to lower LIDT values.

## 5.2. $ZrO_2/SiO_2$ mirrors: results and discussions

The results and parameters of *S-on-1* LIDT testing are presented in Table 5.2.1.

Table 5.2.1. LIDT testing of experimental $ZrO_2/SiO_2$ mirrors

| Design | LIDT, J/cm$^2$ | Pulse duration, fs | Beam diameter 1/e$^2$, μm |
|---|---|---|---|
| *standard* | 0.65 | 130 | 238 |
| *e-field* | 0.44 | | |

The observed behavior of optical resistance in experimental $ZrO_2/SiO_2$ mirrors were in consistency with corresponding *e-field* patterns - erroneous *e-field* design with raised *e-field* intensity in $SiO_2$ layers and layer interfaces demonstrated only 70% of resistance of *standard* design mirror. Damage sites were also inspected

using optical microscope (*BX41, Olympus*) with dark field contrast in reflection mode. (Fig. 5.2.1) shows dark field images of damage sites of both mirrors using pulse with energy close to LIDT (left) and several times exceeding LIDT (right).

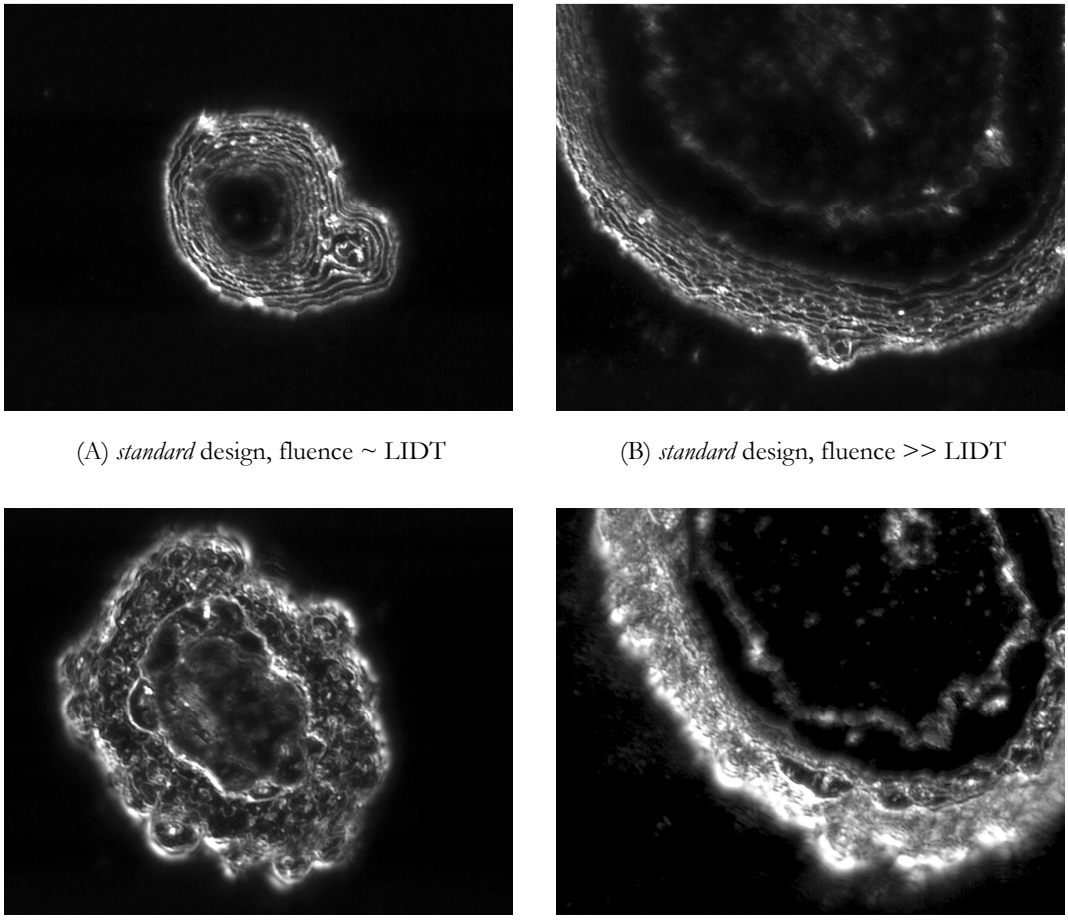

(A) *standard* design, fluence ~ LIDT

(B) *standard* design, fluence >> LIDT

(C) *e-field* design, fluence ~ LIDT

(D) *e-field* design, fluence >> LIDT

Fig. 5.2.1. Images of damage sites of *standard* design (A, B) and *e-field* design (C, D) mirrors. All pictures are of the same scale (78x61 $\mu m^2$).

Morphologies were different – damages of *standard* design mirrors had cone-like shape, where damage was caused by the highest energy density at the centre of Gaussian-shaped laser beam, while *e-field* design clearly demonstrated two-stage pit, possibly obtained when lower energy density at the periphery of the laser beam was still sufficient to initiate damage in outer 8-9 layer pairs where electric field intensity was much higher than in *standard* design coating. Damage sites were also investigated using AFM (*CPII, Veeco*). AFM scan of laser damaged *e-field* mirror is shown in (Fig. 5.2.2). Measured depth of crater corresponded to the

distance of interface of 8th – 9th layer pair from the coating surface, where the intensity of electric field was the highest of all interfaces of the stack. This implied that damage was initiated at this place of the deposited layer structure.

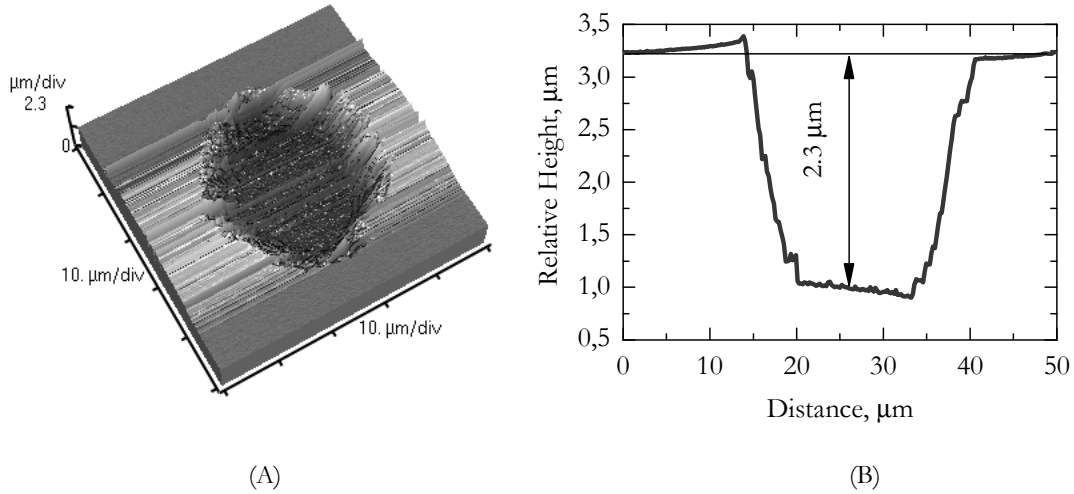


Fig. 5.2.2. A – damage topography of *e-field* design mirror measured by AFM; B – the cross-section of relative height near the geometrical center of the crater.

## 5.3. Preparation of $Ta_2O_5/SiO_2$ and $HfO_2/SiO_2$ samples

Table 5.3.1. Main design and deposition parameters of experimental $Ta_2O_5/SiO_2$ and $HfO_2/SiO_2$ mirrors

| Design | H | L | Process | Nr. of layers | Thick-ness, nm | Tempe-rature °C | H dep. Rate, Å/s | L dep. rate, Å/s | Back-ground IAD gas | Deposition pressure, Pa |
|---|---|---|---|---|---|---|---|---|---|---|
| *standard* | $Ta_2O_5$ | $SiO_2$ | IAD | 24 | 3200 | 50 | 1.3 | 2 | $O_2$ | $8 \times 10^{-3}$ |
| *e-field* | | | | 22 | 2800 | | | | | |
| *standard* | $HfO_2$ | $SiO_2$ | e-beam | 24 | 3270 | 300 | 2 | 2.8 | $O_2$ | $4.5 \times 10^{-3}$ |
| *e-field* | | | | 24 | 3100 | | | | | |

The first set of experiments showed that much more stable materials and processes were needed for the precise manipulation of layer thickness in order to get the desirable distribution of electric field. Therefore, two combinations of processes and high refraction index materials for the next set of experimental mirrors were investigated further: e-beam evaporation of more stable hafnia (hafnium oxide) and highly precise IAD deposition of tantala (tantalum oxide).

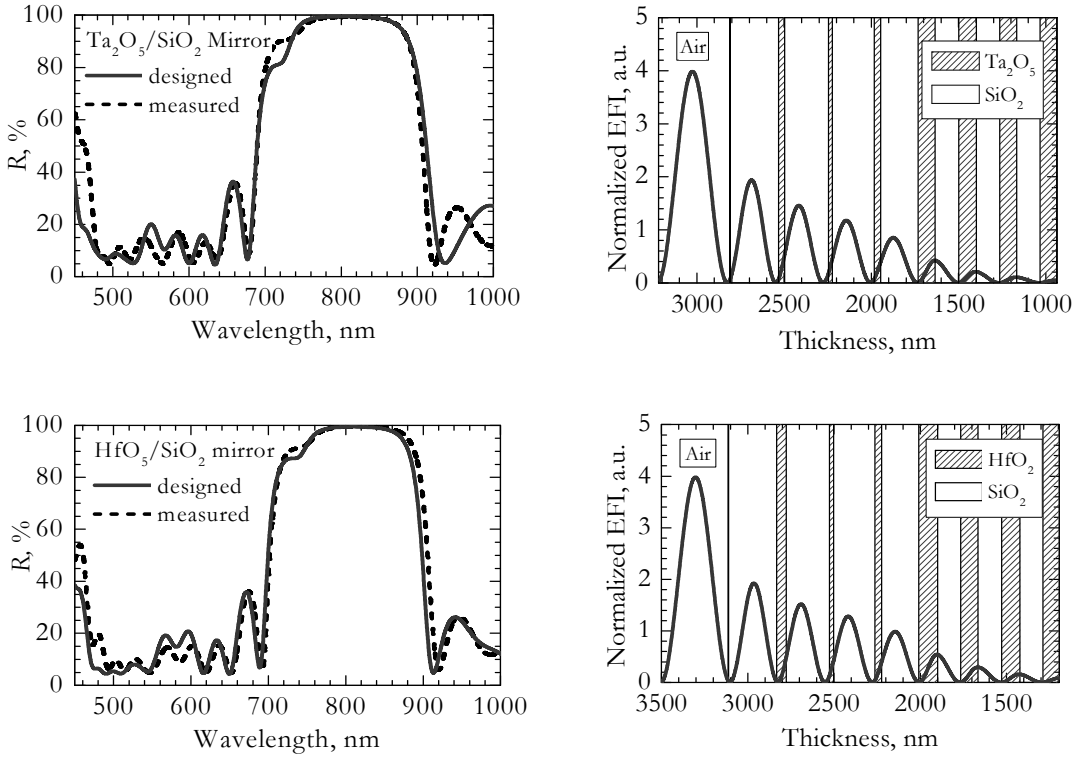


Fig. 5.3.1. Measured and designed spectra of experimental *e-field* $Ta_2O_5/SiO_2$ and $HfO_2/SiO_2$ mirrors (left). Distribution of normalized electric field intensity in the seven pairs of outer layers of *e-field* deposited mirrors, corresponding to measured reflectance spectrum (right).

Additionally, *e-field* design was simplified to decrease the influence of possible errors in modified layer thicknesses to the final pattern of electric field within the coating. Only three outer layer pairs were modified to suppress electric field twofold, compared to a *standard* design mirror. Deposition runs and their technological parameters are presented in Table 5.3.1. Measured transmittance spectra of deposited *e-field* coatings and corresponding distribution of electric field within the outer layers of coatings are shown (Fig. 5.3.1). There was a reasonable match between measured and designed spectra, so corresponding pattern of electric field had fulfilled initial *e-field* design intentions – electric field at outer layer interfaces was suppressed two times, comparing to *standard* design.

## 5.4. $Ta_2O_5/SiO_2$ and $HfO_2/SiO_2$ mirrors: results and discussions

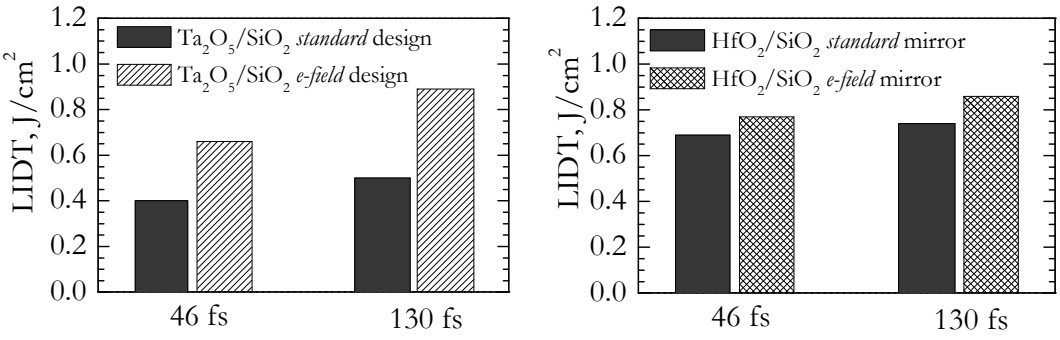


Fig. 5.4.1. LIDT's of $Ta_2O_5/SiO_2$ (left) and $HfO_2/SiO_2$ (right) mirrors for *standard* and *e-field* designs at 46 fs and 130 fs duration pulses.

Laser induced damage threshold (LIDT) of deposited mirrors was experimentally measured in the same manner as for zirconia (zirconium oxide) mirrors. Pulses of 46 fs and 130 fs duration were used. The final LIDT results are summarized in (Fig. 5.4.1). Designs with suppressed *e-field* demonstrated 65-78% increase in LIDT compared to standard quarter-wavelength design for tantala mirrors and 12-16% increase for hafnia mirrors, dependently on pulse duration. The effect of standard mirror stack modification was considerably lower in hafnia case, possibly due to higher band-gap energy of hafnia comparing to tantala. Therefore, it had to be less sensitive to electric field influence on non-linear ionization processes. (Fig. 5.4.2) shows damage sites of $Ta_2O_5/SiO_2$ mirrors (left) and $HfO_2/SiO_2$ mirrors (right). Different morphology could be identified between *standard* (top) and *e-field* (bottom) designs for both materials and followed distribution patterns of electric field at outer layers of coatings. Cone-like pits of standard mirrors confirmed that critical free electron density at the interfaces of outer layers due to higher electric field could be reached by lower energy densities present at peripheral part of the pulse, having Gaussian spatial distribution, while inner layers demanded higher energies, present at the very center of the pulse. Cylindrical shape damage pits in *e-field* coatings implied that the critical conditions

were reached simultaneously at several outer layer interfaces, which clearly correlated to the distribution of electric field within the *e-field* coating (Fig. 5.3.1).

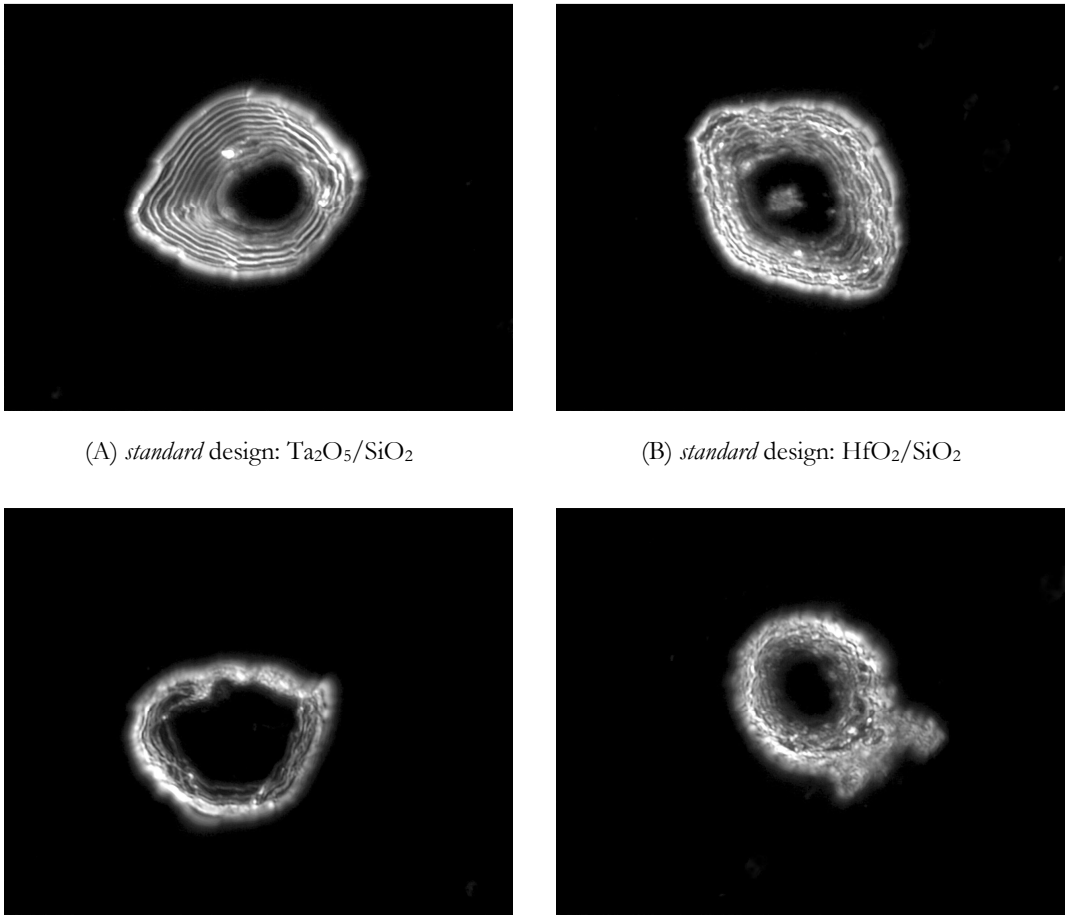

(A) *standard* design: $Ta_2O_5/SiO_2$ (B) *standard* design: $HfO_2/SiO_2$

(C) *e-field* design: $Ta_2O_5/SiO_2$ (D) *e-field* design: $HfO_2/SiO_2$

Fig. 5.4.2. Images of damage morphologies of *standard* design (A - $Ta_2O_5/SiO_2$ B- $HfO_2/SiO_2$) and *e-field* design (C - $Ta_2O_5/SiO_2$, D - $HfO_2/SiO_2$) mirrors. Laser pulse energies close to LIDT.

## 5.5. Conclusions

*Standard* alternating QWOT and custom design $Ta_2O_5/SiO_2$ and $HfO_2/SiO_2$ *e-field* dielectric mirrors centered at 800 nm were deposited by IAD technique. The suppressing of electric field at high refractive index layers as well as in layer interfaces results in the increased optical resistance to intense laser radiation also in femtosecond pulse range. Tantala-silica mirror resulted in 0.66 J/cm$^2$ and

0.89 J/cm$^2$ LIDT for 46 and 130 fs pulses, respectively. These results were 65% and 78% higher in comparison to standard quarter-wavelength design tantala-silica mirrors. Hafnia based *e-field* mirrors had 0.77 J/cm$^2$ and 0.86 J/cm$^2$ LIDT for 46 and 130 fs pulses respectively; this result was 12% and 16% higher compared to standard hafnia-silica mirrors. The effect of suppressed electric field on damage threshold of the coating was considerably lower in hafnia case, due to higher band-gap energy of hafnia comparing to tantala. $ZrO_2/SiO_2$ *e-field* mirrors showed that electric field distribution is sensitive to variations in modified layer thicknesses, and could lead to even lower LIDT in the case of incorrect deposition.

The study of damage sites using optical and AFM microscopes confirmed the relation between the shape of pits and distribution of electric field at the outer layers of experimental mirrors. Cone-like pits of standard mirrors illustrated that damage conditions at the interfaces of outer layers due to the higher electric field could be reached by lower energy densities present at the peripheral part of the pulse. Cylindrical shape damage pits in *e-field* coatings suggested that the critical conditions were reached simultaneously at several outer layer interfaces, which correlated with the equal values of electric field at these interfaces of *e-field* coating.

# List of conclusions

1. An automated metrological facility for *S-on-1* laser-induced damage threshold measurements was developed. It minimizes the influence of human factor and speeds up the LIDT measurement procedure. The sensitivity of assembled metrological facility is sufficient for the determination of various factors (parameters of deposition techniques and coating materials) on LIDT of optical coatings when using femtosecond pulses.

2. *S-on-1* test of optical resistance in dielectric surfaces containing absorbing damage precursors by spatially and energetically fluctuating laser radiation produces the apparently accumulative damage statistics with respect to incident number of pulses because of increasing exposed area and thus increasing probability of damage.

3. The experimental observations of $TiO_2$ coatings showed the stepwise transition in LIDT when continuously tuning the wavelength of laser pulses (130 fs and 1 kHz) in spectral range from 590 nm to 750 nm where two-photon absorption changes to three-photon absorption. It confirms that multiphoton absorption is one of the main damage mechanisms in femtosecond range.

4. The high reflectivity dielectric coatings of alternating $ZrO_2/SiO_2$ QWOT layers evaporated by using conventional electron beam evaporation or ion-assisted deposition typically have surface roughness more than ~2 times higher than substrate roughness. Therefore, the typical roughness of substrate which does not exceed ~0.6 nm has no influence on the LIDT of those coatings in fs range (800 nm, 130 fs and 1 kHz).

5 The densification of HR $ZrO_2/SiO_2$ layers by IAD technique using Ar+ ions with kinetic energy of ~150 eV does not change the LIDT of those coatings for femtosecond (800 nm, 130 fs and 1 kHz) pulses in comparison to with e-beam deposited coatings.

6. The experimental observations using 800 nm, 130 fs and 1 kHz repetition rate laser pulses showed that it is possible to increase the LIDT of HR dielectric coatings up to ~78% by suppressing electric field at the outer layers of high refractive index also in fs pulse range.

# Summary

The present Ph.D. thesis is the experimental and theoretical analysis of damage processes in thin film dielectric coatings induced by the femtosecond laser pulses. Experimental investigations were performed by automated metrological facility designed for *S-on*-1 laser-induced damage threshold measurements. Femtosecond repetitive pulses (1 kHz) either at fixed 800 nm and 400 nm wavelengths or continuously tunable in 590 nm to 750 nm spectral range were used for measurements. The sensitivity of assembled metrological facility was sufficient for the determination of various deposition factors (process parameters and coating materials) on LIDT of optical coatings. During our experimental investigations on multi-layer $ZrO_2/SiO_2$, $HfO_2/SiO_2$, $Ta_2O_5/SiO_2$, $TiO_2/SiO_2$ high reflection coatings and single-layer $TiO_2$ several important results were obtained. This allows us to conclude: stepwise transition of LIDT values was experimentally observed in range where two-photon absorption changes to three-photon absorption. It confirms that multiphoton absorption is one of the main damage mechanisms in femtosecond range. The multilayer coatings deposited by IAD and e-beam techniques on substrates having roughness of 0.64 nm or smaller showed similar LIDT values. Moreover, it was also confirmed that suppressing of standing wave electric field intensity at the outer layers of high refractive index improves the optical resistance of high reflectivity coatings also for femtosecond pulses. Furthermore, the model of the pseudo-accumulation effect is introduced for optical surfaces containing absorbing defects. The results of *Monte Carlo* simulations show that pulse-to-pulse fluctuations of laser beam propagation direction, energy or even mechanical vibrations in the optical systems produce apparently accumulative damage statistics. The exposed area increases shot-by-shot, thus increasing the *S-on*-1 probability of damage.

# References


1. Theodore Maiman, *Stimulated optical radiation in ruby*. Nature **187**, p. 493-494 (1960)
2. Paul Maker, Robert Terhune, and Carleton Savage, *Optical third harmonic generation*. in *Third International Symposium on Quantum Electronics*. Grivetand N. Bloembergen, Editor p. 1559-1576 (1964)
3. B.N. Chichkov, C. Momma, S. Nolte, F. von Alvensleben, and A. Tünnermann, *Femtosecond, picosecond and nanosecond laser ablation of solids*. Applied Physics A: Materials Science & Processing **63**, p. 109-115 (1996)
4. K K Sharma, *Optics Principles and Applications* 2006, Amsterdam: Academic Press is an imprint of Elsevier.
5. Stefano Longhi Giulio Cerullo, Mauro Nisoli, S. Stagira, O. Svelto, *Problems in Laser Physics*. 2001, New York: Kluwer Academic/ Plenum Publishers. 308.
6. Javier Alda, *Laser and Gaussian Beam Propagation and Transformation*, in *Encyclopedia of Optical Engineering*. 2003, Marcel Dekker, Inc.: New York.
7. R. Samad and N. Vieira, *Geometrical method for determining the surface damage threshold for femtosecond laser pulses*. Laser Physics **16**(2), p. 336-339 (2006)
8. A. H. Firester, M. E. Heller, and P. Sheng, *Knife-edge scanning measurements of subwavelength focused light beams*. Applied Optics **16**(7), p. 1971-1977 (1977)
9. J. M. Liu, *Simple technique for measurements of pulsed Gaussian-beam*. OPTICS LETTERS **7**(5), p. 196 - 198 (1982)
10. B. Farkas and Zs. Geretovszky, *On determining the spot size for laser fluence measurements*. Applied Surface Science **252**, p. 4728-4732 (2006)
11. B. C. Stuart, M. D. Feit, S. Herman, A. M. Rubenchik, B. W. Shore, and M. D. Perry, *Nanosecond-to-femtosecond laser-induced breakdown in dielectrics*. Physical Review B **53**(4), p. 1749 (1996)
12. *11254-1: Lasers and laser-related equipment - Determination of laser-induced damage threshold of optical surfaces - Part 1: 1-on-1 test*, ISO, (2000)
13. *11254-2: Lasers and laser-related equipment - Determination of laser-induced damage threshold of optical surfaces - Part 2: S-on-1 test*, ISO, (2001)
14. Emil Wolf Max Born, *Principles of Optics: Electromagnetic Theory of Propagation, Interference and Diffraction of Light*. 6 ed. 1997, Oxford: Cambridge University Press. 836.
15. Vaidutis Antanas Šalna, *Optika*. 1 ed. 2004, Vilnius: Enciklopedija. 272.
16. D. Ristau, *Thin Film Optical Coatings*, in *Encyclopedia of Modern Optics*, Bob D. Guenther, Editor. 2004, Elsevier Academic Press: Amsterdam. p. 360-369.
17. Walter Koechner, *Solid-State Laser Engineering* 6ed. Optical Sciences. 1992, New York: Springer Science+Business Media, Inc. 648.
18. Michael Bass, *Handbook of Optics*. 2 ed. Vol. 1. 1994: McGraw-Hill. 1568
19. M. Jupé, M. Lappschies, L. Jensen, K. Starke, D. Ristau, A. Melninkaitis, V. Sirutkaitis, I. Cravetchi, and W. Rudolph, *Mixed oxide coatings for advanced fs-laser applications*. J. Exarhos Gregory, H. Guenther Arthur, L. Lewis Keith, Ristau Detlev, M. J. Soileau, and J. Stolz Christopher, Editors, Proc. of SPIE, **6720**, p. 67200U, (2007)

20. Detlev Ristau, *Optical coatings for laser technology*. Periodinio seminaro medžiaga (ESF/2004/2.5.0-K02-VS-02). 2007, Vilnius: Vilniaus universiteto leidykla.
21. Program *TFCalc* 3.5, Software Spectra, Inc., (2008)
22. G. L. Dimmick, *Apparatus for the production of reflection reducing coatings*. 1946, Google Patents.
23. P. J. Martin, H. A. Macleod, R. P. Netterfield, C. G. Pacey, and W. G. Sainty, *Ion-beam-assisted deposition of thin films*. Applied Optics **22**(1), p. 178-184 (1983)
24. Hansjörg Niederwald, *Low-temperature deposition of optical coatings using ion assistance*. Thin Solid Films **377-378**, p. 21-26 (2000)
25. Tsai Rung-Ywan, Shiau Sen-Chrong, Lee Chii-Hua, Ho Fang Chuan, and Hua Mu-Yi, *Properties of optical thin films and coatings prepared by reactive electron-beam deposition with and without ion bombardments*. Optical Engineering **36**(12), p. 3433-3438 (1997)
26. John R. McNeil, Alan C. Barron, S. R. Wilson, and Jr W. C. Herrmann, *Ion-assisted deposition of optical thin films: low energy vs high energy bombardment*. Applied Optics **23**(4), p. 552-559 (1984)
27. Hansjörg Niederwald, Sven Laux, Michael Kennedy, Uwe Schallenberg, Angela Duparré, M. Mertin, Norbert Kaiser, and Detlef Ristau, *Ion-Assisted Deposition of Oxide Materials at Room Temperature by use of Different Ion Sources*. Applied Optics **38**(16), p. 3610-3613 (1999)
28. Norbert Kaiser and Hans K. Pulker, *Optical interference coatings*. Springer Series in Optical Sciences. 2003, Berlin. 504.
29. Wayne G. Sainty, R. P. Netterfield, and Philip J. Martin, *Protective dielectric coatings produced by ion-assisted deposition*. Applied Optics **23**(7), p. 1116-1119 (1984)
30. Hyun Ju Cho and Chang Kwon Hwangbo, *Optical inhomogeneity and microstructure of ZrO2 thin films prepared by ion-assisted deposition*. Applied Optics **35**(28), p. 5545-5552 (1996)
31. P. F. Gu and J. F. Tang, *Laser-induced damage resistance of thin-film polarizers prepared by ion-assisted deposition*. Optics Letters **19**(2), p. 81 (1994)
32. Jonathan H. Herringer and Thomas A. Caughey, *Ion-assisted versus nonion-assisted high-laser-damage resistant coatings on BBO*. in *Laser-Induced Damage in Optical Materials: 2002 and 7th International Workshop on Laser Beam and Optics Characterization* **4932**, p. 35-37, (2003)
33. David T. Wei and Anthony W. Louderback, *Method for fabricating multi-layer optical films*. 1978.
34. Michael A. Scobey, Richard I. Seddon, James W. Seeser, R. Russel Austin, Paul M. LeFebvre, and Barry W. Manley, *Magnetron sputtering apparatus and process*. 1988: USA.
35. W. D. Sproul, D. J. Christie, and D. C. Carter, *Control of reactive sputtering processes*. Thin Solid Films **491**(1-2), p. 1-17 (2005)
36. Yao Xu, Bing Zhang, Wen Hao Fan, Dong Wu, and Yu Han Sun, *Sol-gel broadband anti-reflective single-layer silica films with high laser damage threshold*. Thin Solid Films **440**(1-2), p. 180-183 (2003)
37. R. M. Wood, *Laser-induced damage of optical materials*. Optics & Optoelectronics 2003, Bristol and Philadelphia Institute of Physics Publishing

38. Christopher J. Stolz, Michael D. Feit, and Thomas V. Pistor, *Laser intensification by spherical inclusions embedded within multilayer coatings.* Applied Optics **45**(7), p. 1594-1601 (2006)
39. Christopher J. Stolz, Scott Hafeman, and Thomas V. Pistor, *Light intensification modeling of coating inclusions irradiated at 351 and 1053 nm.* Applied Optics **47**(13), p. C162-C166 (2008)
40. Yuanan Zhao, Weidong Gao, Jianda Shao, and Zhengxiu Fan, *Roles of absorbing defects and structural defects in multilayer under single-shot and multi-shot laser radiation.* Applied Surface Science **227**, p. 275–281 (2004)
41. Jean-Yves Natoli, Laurent Gallais, Bertrand Bertussi, Annelise During, Mireille Commandré, Jean-Luc Rullier, Florian Bonneau, and Patrick Combis, *Localized pulsed laser interaction with submicronic gold particles embedded in silica: a method for investigating laser damage initiation.* Optics Express **11**(7), p. 824-829 (2003)
42. S. Papernov and A. W. Schmid, *Two mechanisms of crater formation in ultraviolet-pulsed-laser irradiated SiO2 thin films with artificial defects.* Journal of Applied Physics **97**, p. 114906 (2005)
43. John A. Thornton, *Influence of Apparatus Geometry and Deposition Conditions on the Structure and Topography of Thick Sputtered Coatings.* Journal of Vacuum Science & Technology **11**(4), p. 666-670 (1974)
44. R. Messier, A. P. Giri, and R. A. Roy, *Revised structure zone model for thin film physical structure.* Journal of Vacuum Science & Technology A: Vacuum, Surfaces, and Films **2**(2), p. 500-503 (1984)
45. P.B. Barna and M. Adamik, *Fundamental structure forming phenomena of polycrystalline films and the structure zone models.* Thin Solid Films **317**, p. 27–33 (1998)
46. Eoin P. O'Reilly and John Robertson, *Theory of defects in vitreous silicon dioxide* Physical Review B **27**(6), p. 3780-3795 (1983)
47. M. Mero, A. J. Sabbah, J. Zeller, and W. Rudolph, *Femtosecond dynamics of dielectric films in the pre-ablation regime.* Applied Physics A: Materials Science & Processing **81**(2), p. 317-324 (2005)
48. S.S. Mao, F. Quere, S. Guizard, X. Mao, R.E. Russo, G. Petite, and P. Martin, *Dynamics of femtosecond laser interactions with dielectrics.* Applied Physics A: Materials Science & Processing **79**, p. 1695–1709 (2004)
49. Jonathan W. Arenberg, *Revised damage frequency method for the determination of laser damage threshold.* in *Laser-Induced Damage in Optical Materials: 1993* E. Bennett Harold, L. Chase Lloyd, H. Guenther Arthur, E. Newnam Brian, and M. J. Soileau, Editors, Proc. of SPIE, **2114**, p. 521-526, (1994)
50. S.C. Seitel, A. Giesen, and J. Becker, *International Standard Test Method for Laser Induced Damage of Optical Surfaces.* in *Laser Induced Damage in Optical Materials: 1992.* Harold E. Bennet, Lloyd L. Chase, Arthur H. Guenther, and M.J. Soileau, Editors, Proc. of SPIE, **1848**, p. (1993)
51. Jurgen Becker and Achim Bernhardt, *ISO 11254: an International Standard for the Determination of the Laser Induced Damage Threshold.* in *Boulder Damage Syposium 1993.* H. E. Bennett, L. L. Chase, A. H. Guenther, B. E. Newnam, and M. J. Soileau, Editors, Proc. of SPIE, **2114**, p. 703-713, (1994)

52. Barry R. Masters, *Ernst Abbe and the Foundation of Scientific Microscopes*. Optics and Photonics News (2007)
53. Chris Brandmaier, Kenneth R. Spring, and Michael W. Davidson. *Reflected Light DIC Microscopy*. (Visited: 2008-08-31) Available from: http://www.microscopyu.com/articles/dic/reflecteddic.html.
54. M. Bass and D. Fradin, *Surface and bulk laser-damage statistics and the identification of intrinsic breakdown processes*. Quantum Electronics, IEEE Journal of **9**(9), p. 890-896 (1973)
55. Jonathan W. Arenberg, *Determination of Minimal Test Sample Size for High Accuracy Laser Damage Testing*. in *Laser-Induced Damage in Optical Materials: 1994*. H. E. Bennett, A. H. Guenther, M. R. Kozlowski, B. E. Newnam, and M. J. Soileau, Editors, Proc. of SPIE **2428**, p. 484-488, (1994)
56. Jonathan W. Arenberg, *Error Sources in the Damage Frequency Method*. in *Laser-Induced Damage in Optical Materials: 1997*. H. E. Bennett, A. H. Guenther, M. R. Kozlowski, B. E. Newnam, and M. J. Soileau, Editors, Proc. of SPIE **3244**, p. 42-45, (1997)
57. Jonathan W. Arenberg, *Requirements for the Detection of Damage Events and Measurement of Laser Fluence for High Quality Damage Threshold Measurements*. in *Laser-Induced Damage in Optical Materials: 1993*. H. E. Bennett, L. L. Chase, A. H. Guenther, B. E. Newnam, and M. J. Soileau, Editors, Proc. of SPIE **2114**, p. (1994)
58. Jean-Yves Natoli, Laurent Gallais, Hassan Akhouayri, and Claude Amra, *Laser-induced Damage of Materials in Bulk, Thin-film, and Liquid forms*. Applied Optics **41**(16), p. 3156-3166 (2002)
59. *Laser-Induced Damage Threshold and Certification Procedures for Optical Materials*, National Aeronautics and Space Administration (NASA), (1997)
60. M. A. Villegas, M. A. García, J. Llopis, and J. M. Fernández Navarro, *Optical Spectroscopy of Hybrid Sol-Gel Coatings Doped with Noble Metals*. Journal of Sol-Gel Science and Technology **11**(3), p. 251-265 (1998)
61. Michael Duncan, Mark Bashkansky, and John Reintjes, *Subsurface defect detection in materials using optical coherence tomography*. Optics Express **2**(13), p. 540-545 (1998)
62. H. Krol, L. Gallais, C. Grèzes-Besset, J. Y. Natoli, and M. Commandré, *Investigation of nanoprecursors threshold distribution in laser-damage testing*. Optics Communications **256**(1-3), p. 184-189 (2005)
63. M. Reichling, A. Bodemann, and N. Kaiser, *Defect induced laser damage in oxide multilayer coatings for 248 nm*. Thin Solid Films **320**(2), p. 264-279 (1998)
64. Annelise During, Caroline Fossati, and Mireille Commandré, *Photothermal deflection microscopy for imaging sub-micronic defects in optical materials*. Optics Communications **230**(4-6), p. 279-286 (2004)
65. B. Bertussi, J. Y. Natoli, M. Commandre, J. L. Rullier, F. Bonneau, P. Combis, and P. Bouchut, *Photothermal investigation of the laser-induced modification of a single gold nano-particle in a silica film*. Optics Communications **254**(4-6), p. 299-309 (2005)
66. Zhouling Wu, Christopher J. Stolz, Shannon C. Weakley, James D. Hughes, and Qiang Zhao, *Damage threshold prediction of hafnia-silica multilayer coatings by*

*nondestructive evaluation of fluence-limiting defects.* Applied Optics **40**(12), p. 1897-1906 (2001)
67. N. Bloembergen, *Role of cracks, pores, and absorbing inclusions on laser induced damage threshold at surface of transparent dielectrics.* Applied Optics **12**(4), p. 661 (1973)
68. Alexander A. Manenkov and Vladimir S. Nechitailo, *Physics of multishot laser damage to optical materials.* in *Laser-Induced Damage in Optical Materials: 1990* E. Bennett Harold, L. Chase Lloyd, H. Guenther Arthur, E. Newnam Brian, and M. J. Soileau, Editors, Proc. of SPIE **1441**, p. 392-405, (1991)
69. M. A. Stevens-Kalceff, A. Stesmans, and Wong Joe, *Defects induced in fused silica by high fluence ultraviolet laser pulses at 355 nm.* Applied Physics Letters **80**(5), p. 758-760 (2002)
70. K. L. Lewis, Smith G. W, and and A. J. Pidduc, *Nodular defects in sputtered coatings.* in *Laser-Induced Damage in Optical Materials: 1996*. G. J. Exarhos, A. H. Guenther, N. Kaiser, K. L. Lewis, M. J. Soileau, C. J. Stolz, A. Giesen, and H. Weber, Editors, Proc. of SPIE **4932**, p. 26-34, (1996)
71. L. Gallais, H. Krol, J. Y. Natoli, M. Commandré, M. Cathelinaud, L. Roussel, M. Lequime, and C. Amra, *Laser damage resistance of silica thin films deposited by Electron Beam Deposition, Ion Assisted Deposition, Reactive Low Voltage Ion Plating and Dual Ion Beam Sputtering.* Thin Solid Films **515**(7-8), p. 3830-3836 (2007)
72. J. O. Porteus and Steven C. Seitel, *Absolute onset of optical surface damage using distributed defect ensembles.* Applied Optics **23**(21), p. 3796 (1984)
73. Gordon Lukesh, Susan Chandler, and David Voelz, *Estimation of laser system pointing performance by use of statistics of return photons.* Applied Optics **39**(9), p. 1359-1371 (2000)
74. M. Bass and H. Barrett, *Avalanche breakdown and the probabilistic nature of laser-induced damage.* Quantum Electronics, IEEE Journal of **8**(3), p. 338-343 (1972)
75. P.T. Mannion, J. Magee, E. Coyne, G.M. O'Connor, and T.J. Glynn, *The effect of damage accumulation behaviour on ablation thresholds and damage morphology in ultrafast laser micro-machining of common metals in air.* Applied Surface Science **233**, p. 275–287 (2004)
76. Rafael R. Gattass, Loren R. Cerami, and Eric Mazur, *Micromachining of bulk glass with bursts of femtosecond laser pulses at variable repetition rates.* Optics Express **14**(12), p. 5279-5284 (2006)
77. Nicolaas Bloembergen, *Laser-Induced Electric Breakdown in Solids.* IEEE Journal of Quantum Electonics **QE-10**(3), p. 375-386 (1974)
78. M. Mero, J. Liu, W. Rudolph, D. Ristau, and K. Starke, *Scaling laws of femtosecond laser pulse induced breakdown in oxide films.* Physical Review B **71**(11), p. 115109 (2005)
79. B. C. Stuart, M. D. Feit, A. M. Rubenchik, B. W. Shore, and M. D. Perry, *Laser-Induced Damage in Dielectrics with Nanosecond to Subpicosecond Pulses.* Physical Review Letters **74**(12), p. 2248 (1995)
80. Wolfgang Kautekand, Jörg Krüger, Matthias Lenzner, Sasa Sartania, Christian Spielmann, and Ferenc Krausz, *Laser ablation of dielectrics with pulse durations between 20 fs and 3 ps.* Applied Physics Letters **69** (21), p. 3146-3148 (1996)

81. B. C. Stuart, M. D. Feit, S. Herman, A. M. Rubenchik, B. W. Shore, and M. D. Perry, *Optical ablation by high-power short-pulse lasers.* J. Opt. Soc. Am. B **13**(2), p. 459-468 (1996)
82. S. Martin, A. Hertwig, M. Lenzner, J. Krüger, and W. Kautek, *Spot-size dependence of the ablation threshold in dielectrics for femtosecond laser pulses.* Applied Physics A: Materials Science & Processing **77**(7), p. 883-884 (2003)
83. C.W. Carr, H.B. Radousky, and S.G. Demos, *Wavelength Dependence of Laser-Induced Damage: Determining the Damage Initiation Mechanisms.* Physical Review Letters **91**(12) (2003)
84. M. E. Frink, J. W. Arenberg, D. W. Mordaunt, S. C. Seitel, M. T. Babb, and E. A. Teppo, *Temporary laser damage threshold enhancement by laser conditioning of antireflection-coated glass.* Applied Physics Letters **51**(6), p. 415-417 (1987)
85. M. Khenner and V. K. Henner, *Temperature of spatially modulated surface of solid film heated by repetitive laser pulses.* Journal of Physics D **38**, p. 4196–4201 (2005)
86. S. Küper and M. Stuke, *Femtosecond uv Excimer Laser Ablation.* Applied Physics B **44**, p. 199-204 (1987)
87. D. Du, X. Liu, G. Korn, J. Squier, and G. Mourou, *Laser-induced breakdown by impact ionization in SiO[sub 2] with pulse widths from 7 ns to 150 fs.* Applied Physics Letters **64**(23), p. 3071-3073 (1994)
88. X. A. Shen, Scott C. Jones, and Peter Braunlich, *Laser heating of free electrons in wide-gap optical materials at 1064 nm.* Physical Review Letters **62**(23), p. 2711 (1989)
89. D. Ashkenasi, M. Lorenz, R. Stoian, and A. Rosenfeld, *Surface damage threshold and structuring of dielectrics using femtosecond laser pulses: the role of incubation.* Applied Surface Science **150**(1-4), p. 101-106 (1999)
90. Chris B. Schaffer, André Brodeur, and Eric Mazur, *Laser-induced breakdown and damage in bulk transparent materials induced by tightly focused femtosecond laser pulses.* Measurement Science and Technology **12**, p. 1784 (2001)
91. A. Vogel and V. Venugopalan, *Mechanisms of pulsed laser ablation of biological tissues.* Chemical Reviews **103**(2), p. 577-644 (2003)
92. R. Stoian, D. Ashkenasi, A. Rosenfeld, and E. E. B. Campbell, *Coulomb explosion in ultrashort pulsed laser ablation of Al2O3.* Physical Review B **62**(19), p. 13167 (2000)
93. M. Sakakura, M. Terazima, Y. Shimotsuma, K. Miura, and K. Hirao, *Observation of pressure wave generated by focusing a femtosecond laser pulse inside a glass.* Optics Express **15**(9), p. 5674-5686 (2007)
94. M. Sakakura, M. Terazima, Y. Shimotsuma, K. Miura, and K. Hirao, *Heating and rapid cooling of bulk glass after photoexcitation by a focused femtosecond laser pulse.* Optics Express **15**(25), p. 16800-16807 (2007)
95. Eric Mazur Rafael R. Gattass, *Femtosecond laser micromachining in transparent materials.* Nature Photonics **2**, p. 219 - 225 (2008)
96. Cord L. Arnold, *Erzeugung optischer Durchbrüche bei hoher numerischer Apertur: Numerische Simulationen zur Submikrometer-Manipulation transparenter Materialien und biologischer Zellen mit ultrakurzen Laserpulsen*, PhD thesis, Leibniz Universität Hannover, (2007)

97. Kai Starke, *Übertragung von Standardmessverfahren zur Charakterisierung optischer Beschichtungen in den Bereich ultrakurzer Laserpulse*, PhD thesis, Universität Hannover, (2004)
98. L. V. Keldysh, *Ionization in the field of a strong electromagnetic wave.* JETP **47**, p. 1945-57 (1964)
99. S. Augst, D. Strickland, D. D. Meyerhofer, S. L. Chin, and J. H. Eberly, *Tunneling ionization of noble gases in a high-intensity laser field.* Physical Review Letters **63**(20), p. 2212 (1989)
100. C. B. Schaffer, J. F. García, and E. Mazur, *Bulk heating of transparent materials using a high-repetition-rate femtosecond laser.* Applied Physics A: Materials Science & Processing **76**(3), p. 351-354 (2003)
101. Mark Mero, Benjamin Clapp, Jayesh C. Jasapara, Wolfgang Rudolph, Detlev Ristau, Kai Starke, Jörg Krüger, Sven Martin, and Wolfgang Kautek, *On the damage behavior of dielectric films when illuminated with multiple femtosecond laser pulses.* Optical Engineering **44**(5), p. 051107-1 - 051107-7 (2005)
102. A. Rosenfeld, M. Lorenz, R. Stoian, and D. Ashkenasi, *Ultrashort-laser-pulse damage threshold of transparent materials and the role of incubation.* Applied Physics A: Materials Science & Processing **69** p. S373–S376 (1999)
103. M. Lenzner, J.Krüger, W.Kautek, and F. Krausz, *Incubation of laser ablation in fused silica with 5-fs pulses.* Applied Physics A: Materials Science & Processing **69**, p. 465–466 (1999)
104. A.E. Chmel, *Fatigue laser-induced damage in transparent materials.* Materials Science and Engineering B **49** p. 175-190 (1997)
105. A.E. Chmel, *Cumulative Effect in Laser-Induced Damage of Optical Glasses: A Review.* Glass Physics and Chemistry **26**(1), p. 49-58 (2000)
106. F. Brygo, A. Semerok, R. Oltra, J. M. Weulersse, and S. Fomichev, *Laser heating and ablation at high repetition rate in thermal confinement regime.* Applied Surface Science **252** p. 8314–8318 (2006)
107. Shane Eaton, Haibin Zhang, Peter Herman, Fumiyo Yoshino, Lawrence Shah, James Bovatsek, and Alan Arai, *Heat accumulation effects in femtosecond laser-written waveguides with variable repetition rate.* Optics Express **13**(12), p. 4708-4716 (2005)
108. Shane M. Eaton, Haibin Zhang, Mi Li Ng, Jianzhao Li, Wei-Jen Chen, Stephen Ho, and Peter R. Herman, *Transition from thermal diffusion to heat accumulation in high repetition rate femtosecond laser writing of buried optical waveguides.* Optics Express **16**(13), p. 9443-9458 (2008)
109. Wataru Watanabe Takayuki Tamaki, Kazuyoshi Itoh, *Laser micro-welding of transparent materials by a localized heat accumulation effect using a femtosecond fiber laser at 1558 nm.* Optics Express **14**(22), p. 10468 - 10476 (2006)
110. Haibin Zhang, Shane M. Eaton, Jianzhao Li, and Peter R. Herman, *Heat accumulation during high repetition rate ultrafast laser interaction: Waveguide writing in borosilicate glass.* Journal of Physics: Conference Series **59**, p. 682-686 (2007)
111. B. M. Kim, M. D. Feit, A. M. Rubenchik, E. J. Joslin, J. Eichler, P. C. Stoller, and L. B. Da Silva, *Effects of high repetition rate and beam size on hard tissue damage due to subpicosecond laser pulses.* Applied Physics Letters **76**(26), p. 4001-4003 (2000)

112. David Gomez and Igor Goenaga, *On the incubation effect on two thermoplastics when irradiated with ultrashort laser pulses: Broadening effects when machining microchannels.* Applied Surface Science **253**, p. 2230–2236 (2006)
113. Personal communication: Marco Jupé, 2008
114. Meiqiong Zhan, Hongbo He, Yuanan Zhao, Guanglei Tian, Jianda Shao, and Zhengxiu Fan, *Overcoat dependence of laser-induced damage threshold of 355 nm HR coatings.* Applied Surface Science **252** p. 2126–2130 (2006)
115. Robert Chow, Steve Falabella, Gary E. Loomis, Frank Rainer, Christopher J. Stolz, and Mark R. Kozlowski, *Reactive evaporation of low-defect density hafnia.* Applied Optics **32**(28), p. 5567 (1993)
116. R. Crase, *The Effects of Polishing Materials on the Laser Damage Threshold of Optical Coatings*. in *Laser-Induced Damage in Optical Materials : 1990*. H. E. Bennett, L. L. Chase, A. H. Guenther, B. E. Newnam, and M. J. Soileau, Editors, Proc. of SPIE **1441**, p. 381-389, (1991)
117. Y. Yoshino, K. Inoue, M. Takeuchi, T. Makino, Y. Katayama, and T. Hata, *Effect of substrate surface morphology and interface microstructure in ZnO thin films formed on various substrates.* Vacuum **59**(2-3), p. 403-410 (2000)
118. Ying Wang, Yueguang Zhang, Xu Liu, Weilan Chen, and Peifu Gu, *Gaussian profile laser intensification by nodular defects in mid-infrared high reflectance coatings.* Optics Communications **278**(2), p. 317-320 (2007)
119. *Powder diffraction file PDF-2 database 1-44, Pennsylvania Joint Committee Powder Diffraction Standard, PDF No 50 - 1089*, International Center for Diffraction Data, (1988)
120. *Powder diffraction file PDF-2 database 1-44, Pennsylvania Joint Committee Powder Diffraction Standard, PDF No 65 - 1023*, International Center for Diffraction Data, (1988)
121. F. Demichelis, E. Mezzetti-Minetti, L. Tallone, and E. Tresso, *Optimization of optical parameters and electric field distribution in multilayers.* Applied Optics **23**(1), p. 165 (1984)
122. Weidong Gao, Meiqiong Zhan, Shuhai Fan, Janda Shao, and Zheng-Xiu Fan, *Laser-induced damage of Ta2O5/SiO2 narrow-band interference filters under different 1064 nm Nd:YAG laser modes.* Applied Surface Science **250**(1-4), p. 195-202 (2005)
123. Carl M. Liebig and W. M. Dennis, *Simulation of interactions of high-intensity ultrashort pulses with dielectric filters.* Optical Engineering **46**(2), p. 023801 (2007)
124. Joseph Lowry, Marshall Thomsen, Ernest R. Behringer, and Zhouling Wu, *Layer Thickness Fluctuations in Optical Coatings with Non-Quarter-Wave Design.* Applied Optics **38**(10), p. 2083-2085 (1999)